

Optical study of stratification for partially premixed combustion

Citation for published version (APA):

Izadi Najafabadi, M. (2017). *Optical study of stratification for partially premixed combustion*. [Phd Thesis 1 (Research TU/e / Graduation TU/e), Mechanical Engineering]. Technische Universiteit Eindhoven.

Document status and date:

Published: 07/12/2017

Please check the document version of this publication:

- A submitted manuscript is the version of the article upon submission and before peer-review. There can be important differences between the submitted version and the official published version of record. People interested in the research are advised to contact the author for the final version of the publication, or visit the DOI to the publisher's website.
- The final author version and the galley proof are versions of the publication after peer review.
- The final published version features the final layout of the paper including the volume, issue and page numbers.

[Link to publication](#)

General rights

Copyright and moral rights for the publications made accessible in the public portal are retained by the authors and/or other copyright owners and it is a condition of accessing publications that users recognise and abide by the legal requirements associated with these rights.

- Users may download and print one copy of any publication from the public portal for the purpose of private study or research.
- You may not further distribute the material or use it for any profit-making activity or commercial gain
- You may freely distribute the URL identifying the publication in the public portal.

If the publication is distributed under the terms of Article 25fa of the Dutch Copyright Act, indicated by the "Taverne" license above, please follow below link for the End User Agreement:

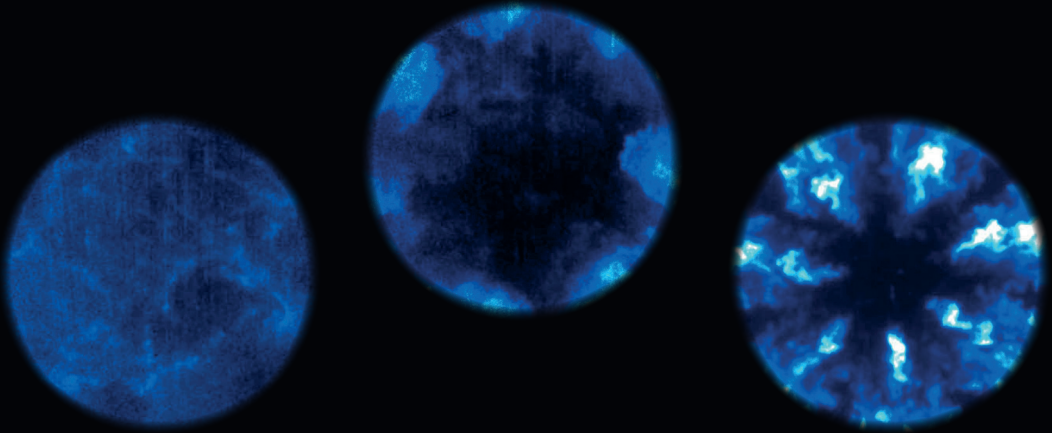
www.tue.nl/taverne

Take down policy

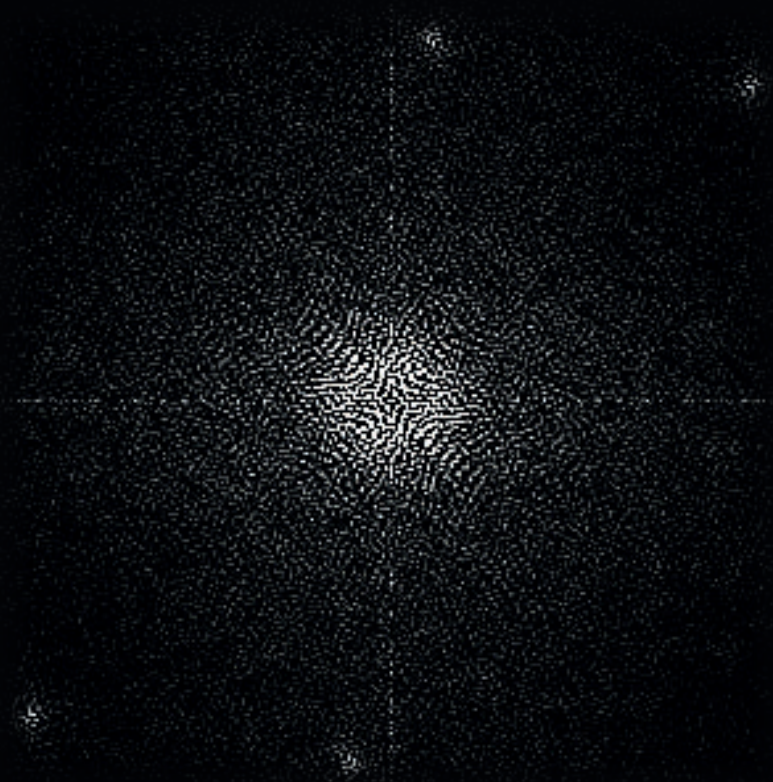
If you believe that this document breaches copyright please contact us at:

openaccess@tue.nl

providing details and we will investigate your claim.



**Optical Study of Stratification
for
Partially Premixed Combustion**



M. Izadi Najafabadi

Optical Study of Stratification for Partially Premixed Combustion

PROEFSCHRIFT

ter verkrijging van de graad van doctor aan de Technische Universiteit Eindhoven, op gezag van de rector magnificus, prof.dr.ir. F.P.T. Baaijens, voor een commissie aangewezen door het College voor Promoties, in het openbaar te verdedigen op donderdag 7 december 2017 om 16.00 uur

door

Mohammad Izadi Najafabadi

geboren te Najafabad, Iran

Dit proefschrift is goedgekeurd door de promotor en de samenstelling van de promotiecommissie is als volgt:

voorzitter: prof.dr. L.P.H. de Goey
1^e promotor: prof.dr. B. Johansson
2^e promotor: prof.dr.ir. N.G. Deen
co-promotor: dr. N.J. Dam
co-promotor: dr.ir. L.M.T. Somers
leden: prof.dr. S. Kaiser (University of Duisburg-Essen)
prof.dr. A.M. Taylor (Imperial College London)
prof.dr.ir. G.J.F. van Heijst

Het onderzoek of ontwerp dat in dit proefschrift wordt beschreven is uitgevoerd in overeenstemming met de TU/e Gedragscode Wetenschapsbeoefening.

To Fahimeh

Optical Study of Stratification for Partially Premixed Combustion
by Mohammad Izadi Najafabadi
Technische Universiteit Eindhoven, 2017

Copyright © 2017 M. Izadi Najafabadi
Cover design by M. Izadi Najafabadi
Back cover photography by Bart van Overbeeke
Printed by Gildeprint, Enschede, The Netherlands

A catalogue record is available from the Eindhoven University of Technology Library
ISBN: 978-90-386-4401-1

This research has received funding from the People Programme (Marie Curie Actions) of the European Union's Seventh Framework Programme FP7/2007–2013/ under REA Grant Agreement No. 607214.



Contents

Contents	v
Summary	ix
1 Introduction	1
1.1 Motivation	2
1.2 Partially Premixed Combustion	3
1.3 Research objectives	5
1.4 Thesis outline	5
2 Experimental Set-up	7
2.1 Introduction	8
2.2 Light-duty Optical Engine	8
2.3 Fuel System	9
2.4 Engine Intake	10
2.5 Heat Release Rate Analysis	10
2.6 Operating Conditions	11
2.7 Experimental Setup for PIV measurements	11
2.8 Conclusion	12
3 Ignition Sensitivity of PPC	13
3.1 Introduction	14
3.2 Experimental Methods	15
3.2.1 Shadowgraphy	15
3.2.2 OH* Chemiluminescence	17
3.2.3 Operating Conditions	18
3.3 Post-Processing	18
3.3.1 Shadowgraphy Image Processing	18
3.3.2 OH* Chemiluminescence Image Processing	20
3.4 Results and Discussions	21
3.4.1 Ignition Sensitivity to Injection Timing	21
3.4.2 Spray Penetration and Targeting	22
3.4.3 Combustion Stratification	26
3.4.4 Comparison with CFD Results	29
3.5 Conclusions	31

4	Spectral Signature and Stratification	33
4.1	Introduction	34
4.2	High-speed Spectroscopy Setup	35
4.2.1	Operating Conditions	37
4.3	Spectroscopy Analysis	38
4.4	Results and Discussion	40
4.4.1	Effect of Combustion Stratification	41
4.4.2	Adequacy of Bandpass Filters	43
4.4.3	Chemiluminescence & Rate of Heat Release	45
4.4.4	A Proxy for Equivalence Ratio	46
4.5	Conclusions	48
5	Fourier-based Stratification Analysis	49
5.1	Introduction	50
5.2	OH* Bandpass Imaging	51
5.2.1	Operating Conditions	52
5.3	Combustion Stratification Analysis	53
5.3.1	Angular, Radial and Vertical Stratification	54
5.3.2	Fourier-based Stratification	55
5.3.3	Validation	58
5.4	Results and Discussion	58
5.4.1	Angular, Radial and Vertical Stratification	60
5.4.2	Fourier-based Stratification	61
5.4.3	Effect of the Considered Spatial Frequency Range	63
5.5	Conclusions	64
6	Fuel Stratification	65
6.1	Introduction	66
6.2	Fuel-Tracer LIF Setup	67
6.2.1	Operating Conditions	68
6.3	Post-processing of LIF Images	69
6.3.1	Background and Flat Field Corrections	69
6.3.2	Temperature Dependency of Toluene Fluorescence	69
6.3.3	Quantification Procedure	70
6.4	Results and Discussion	72
6.4.1	Fuel, Thermal and Combustion Stratification	72
6.4.2	Fuel Stratification and Spectral Signature	76
6.4.3	Fourier-based Stratification Analysis	79
6.4.4	Effects of Intake Temperature on Fuel Stratification	80
6.5	Conclusions	81
7	Turbulence and Stratification	83
7.1	Introduction	84
7.2	PIV Setup	85
7.2.1	Operating Conditions	87
7.3	PIV Post-Processing	88

7.3.1	Image Distortion and Adaptive PIV	88
7.3.2	Ensemble Average Velocity and Cycle-resolved Turbulence	88
7.4	Results and Discussion	90
7.4.1	Flow Characteristics of PPC: from SOI to End of Combustion	90
7.4.2	Effects of Injection Timing	93
7.4.3	Injection-Driven vs Combustion-Driven Turbulence	95
7.4.4	Comparison of 7-hole and 5-hole injectors	98
7.5	Conclusions	99
8	Conclusions and Outlook	101
8.1	Introduction	102
8.2	PPC and Stratification	102
8.3	Stratification Index	103
8.4	Laser/Optical Diagnostics and Quantification	104
8.5	Conclusion	106
	Appendices	107
	Abbreviations	109
	Bibliography	111
	Acknowledgements	121
	PhD Publications	123
	Curriculum vitae	125

Summary

The growing impacts of Hybrid Electric Vehicles (HEV) and upcoming constraints on CO₂ emissions provide an opportunity for new combustion concepts to take over the role of conventional concepts. Partially Premixed Combustion (PPC), a new Compression Ignition (CI) combustion concept, combines the advantages of both Homogeneous Charge Compression Ignition (HCCI) and conventional diesel combustion. In PPC, the fuel partially premixes with air as a consequence of earlier injection and longer ignition delay compared to diffusion-controlled combustion, resulting in lower soot and NO_x emissions, while maintaining high indicated efficiency. The strategy and the timing of the injection provide control over both fuel and thermal stratification, and hence over the timing of the combustion and the behavior of the heat release. However, finding the optimal stratification level of fuel, temperature and combustion for PPC is a challenging issue. The main objective of this study is to investigate various aspects of stratification in PPC to better understand this combustion concept. A light-duty optical engine has been used throughout this study, and different optical/laser diagnostic techniques are applied to fundamentally investigate this phenomenon.

The ignition sensitivity of PPC to injection timing is investigated by using high-speed shadowgraphy and OH* chemiluminescence imaging. Shadowgraphy is used to visualize fuel injection and evaporation while OH* chemiluminescence imaging is used to study the combustion stratification. Results confirm that Start of Injection (SOI) strongly affects the spray penetration and evaporation of fuel. Moreover, combustion stratification has an inverse correlation with combustion phasing of PPC for late injections.

High-speed spectroscopy measurements are used to study the effects of stratification on the spectral signature of PPC (270 – 540 nm range). A method has been developed to distinguish chemiluminescence from thermal radiation, and different chemiluminescing species (OH*, CH* and C₂*) could be identified. The results indicate that the spectral signature of the combustion is highly dependent on the stratification level. It is shown that the broadband chemiluminescence can serve as a proxy for equivalence ratio and the rate of heat release. From the C₂* chemiluminescence, it appears that two different chemical mechanisms for formation of C₂* are active in the PPC regime: it is first formed during the early stage of combustion by the breakup of bigger molecules, and secondarily during the late stage of combustion when soot particles are forming.

In order to compare stratification levels of different PPC strategies or other combustion concepts,

an objective and meaningful definition of “stratification level” is proposed, based on Fourier analysis of OH^* chemiluminescence images, which is assumed to provide spatial information regarding heat release. Two-dimensional Fourier transforms translate these chemiluminescence images into a range of spatial frequencies. The information in this range of frequencies is used to define combustion stratification, using an appropriate normalization procedure. The results indicate that this new definition overcomes the drawbacks of previous definitions used in the literature and is a promising method to meaningfully compare the levels of combustion and fuel stratification in different experiments.

Fuel tracer Laser-Induced Fluorescence (LIF) is used to investigate the effects of fuel stratification on PPC, and to measure/estimate the in-cylinder fuel and temperature distributions. Quantification of fuel-tracer LIF images is performed based on the temperature dependency of the fluorescence signal of toluene (tracer), combined with a comprehensive thermodynamic model, resulting in both temperature and fuel distributions. Quantified results on the fuel distribution are linked to crank-angle resolved OH^* luminescence images and spectroscopy measurements. Results confirm that fuel stratification can either decrease or increase the peak heat release rate, depending on the pattern and the values of local equivalence ratios. Fourier-based analysis of fuel distributions provide an objective metric for fuel stratification, which can be used as a tool to optimize the stratification in the PPC regime from different points of view, such as emissions, efficiency, heat release rate and controllability.

In the end, to investigate the effects of flow and turbulence on stratification, high-speed Particle Image Velocimetry (PIV) is used to measure fluid flow characteristics, including the flow fields, mean velocity and cycle-resolved turbulence, inside the piston bowl as well as in the squish region. Two injectors, having 5 and 7 holes, are compared to see their effects on fluid flow and heat release behavior for different injection timings. Reactive and non-reactive measurements are performed to distinguish injection-driven and combustion-driven turbulence. Formation of vortices and higher turbulence levels enhance the air/fuel interaction, changing the level of fuel stratification and combustion duration. Results demonstrate clearly how later injection (up to a certain point) causes higher mean velocity and turbulence level inside the piston bowl, and consequently higher mixing efficiency.

Introduction



This image is showing a Tesla Delivery Truck in Sydney, ND, taken from Tesla Updates website.

1.1 Motivation

Internal combustion engines are the workhorses of modern society. Today's contribution of transportation energy to the total energy used by the entire human civilization is about 20%. This share slightly increases to 23% for global carbon dioxide emissions [1]. The contribution of internal combustion (IC) engines to the total land transportation power supply is almost 100%; considering 1.2 million Battery Electric Vehicles (BEVs) out of 1.2 billion cars and trucks in 2016 [2] would result in a share of 0.1% for E-Vehicles. The same story holds for the role of IC engines in marine transportation.

The foreseeable future of IC engines does not show signs of it being abandoned. Recent developments in biofuels allow for production of liquid fuels without the risk of fuel depletion. Electrification of vehicles is developing based on electrical energy derived from batteries or hydrogen fuel cells. The energy density of these energy carriers is currently orders of magnitude smaller than that of carbon-based liquid fuels [3]. So, even though the alternatives for IC engines are expected to become more numerous, they are unlikely to make up for much more than 10% share of transport energy by 2040 [1, 4]. Hence, the vision on the future of internal combustion engines is still inspiring and motivating to improve their efficiency and to reduce their emissions.

Although IC engines have been improved steadily during the last century, from efficiency, emission, power, size and control points of view, the primary combustion concepts are still limited to conventional compression-ignition (CI) engines and spark-ignited (SI) engines. These concepts survived, even when emission standards tried to limit emissions such as NO_x , CO and particulate matter (PM). Indeed, many new technologies such as high-pressure injection systems, Exhaust Gas Recirculation (EGR) and exhaust gas treatment systems were all implemented in IC engines during last years to meet limiting emission regulations, without significantly modifying the combustion concept itself. However, upcoming regulations, such as EURO 7, are targeting CO_2 emission for the first time. It is a critical point for conventional concepts to meet high-efficiency demands related to new CO_2 emission regulations, while decreasing other emissions even more. Hence, efficiency is playing a key role for designing future IC engines.

New combustion concepts, mainly various implementations of low temperature combustion (LTC), have shown a potential to improve indicated efficiency and to reduce NO_x and soot emissions. However, these combustion concepts have been problematic from a control point of view. Combining an IC engine with an electric propulsion system, i.e. hybridization, is a practical solution to avoid running IC engines in transient load/speed modes, when the efficiency of IC engines is far lower than in their optimum mode. Running an IC engine in a steady-state (load/speed) mode means that new combustion concepts, with limited controllability but superior efficiency, have now the opportunity to emerge in the market.

1.2 Partially Premixed Combustion

Conventional compression-ignition (CI) engines, using diesel as fuel, provide high indicated efficiencies ($\approx 50\%$), but also high soot and NO_x emissions. In such CI engines, liquid fuel is injected at the end of the compression stroke into the high-pressure and -temperature air charge. The fuel spray ignites almost instantaneously, after only a short ignition delay, which is followed by rapid heat release. Subsequently, a stable, diffusion-controlled spray burns until the end of injection, which results in a smooth, gradual heat release.

In spark ignition (SI) engines, an essentially homogeneous (premixed) mixture of fuel and air is ignited in the cylinder by an electrical spark. Premixing reduces the amount of soot emissions formed during combustion. However, stoichiometric burning of fuel will result in a high combustion temperature and consequently high NO_x emissions. Using a fuel-lean mixture is challenging in SI engines due to the lower flame propagation speed of fuel-lean mixtures compared to that of a stoichiometric mixture. In comparison with conventional CI engines, SI engines have a lower compression ratio, limited by knocking, resulting in lower indicated efficiency of SI engines ($\approx 35\%$).

New compression ignition combustion concepts aim to increase the ignition delay and thereby enhance fuel/air premixing to reduce both NO_x and soot emissions (which are typically related by a trade-off), while maintaining a high indicated efficiency. Enhanced fuel/air mixing would result in lower local equivalence ratios (< 1) and consequently a lower combustion temperature. A common name for this kind of combustion is Low Temperature Combustion (LTC).

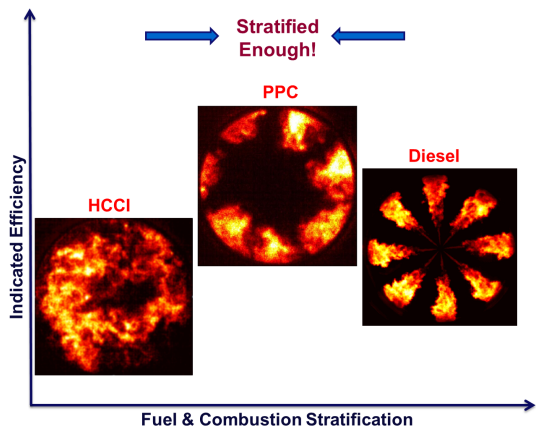
LTC research is inspired by the Homogeneous Charge Compression Ignition (HCCI) concept. HCCI has proven to combine low emissions and relatively high indicated efficiency ($\approx 45\%$) compared to conventional SI engines [5, 6]. The homogeneous air/fuel mixture is ignited by compression, i.e. the density and temperature are raised until the mixture reacts spontaneously. HCCI combustion concepts bring several advantages. First of all, HCCI engines run fuel-lean, implying that they can operate at conventional CI compression ratios (≤ 15). This has the advantage that they can achieve up to 30% (relatively) higher efficiencies than conventional SI gasoline engines [7]. Secondly, homogeneous mixing of fuel and air leads to cleaner combustion and lower emissions. Because peak temperatures are significantly lower compared to typical SI and diesel engines, NO_x levels are almost negligible. Moreover, HCCI does not produce soot because of the absence of locally fuel-rich regions during combustion [8]. Other advantages are that HCCI engines can operate on a large variety of fuels and avoid throttle losses, thereby improving efficiency (especially at part load).

The drawbacks of HCCI are mainly related to the rapid combustion and difficulties to control the combustion timing. HCCI engines are constrained at low loads and low speeds by fuel-lean reactivity limits and at high loads by in-cylinder pressure rise rate and peak restrictions which can damage the engine. The low temperature fuel-lean combustion results in incomplete oxidation of the fuel, therefore the CO and unburned hydrocarbon emissions are typically higher than in a spark-ignition engine [9]. The HCCI concept also suffers from issues regarding the combustion phasing control, since the injection timing and start of combustion are not coupled

any more as in traditional CI engines. The most effective solution to this problem is to use Direct Injection (DI) with fuel injection sufficiently close to top dead center (TDC) to improve combustion controllability but still early enough to provide extensive fuel/air premixing. In this mode, the LTC concepts are referred to as Partially Premixed Combustion (PPC). “Stratified fuel cloud burns with a mixture of diffusion and premixed flames together with some bulk auto-ignition”, phrased by Kalghatgi and Johansson [1] to describe PPC process. The “stratification” word is used in PPC regime to describe in-cylinder inhomogeneities of fuel, temperature, turbulence and combustion.

Regarding fuel stratification at the start of combustion (SOC), partially premixed combustion is located somewhere between HCCI and the conventional CI processes (see Fig. 1.1). Fuel stratification provides a means to control combustion phasing and heat release rate behavior, and thus to overcome the poor controllability of HCCI. There is an optimum point for stratification (called “stratified enough!” in Fig. 1.1) in the PPC regime, in which the indicated efficiency would be higher than for both HCCI and conventional CI combustion ($\approx 55\%$), while NO_x and soot emission are relatively low. This feature is graphically illustrated in Fig. 1.1, where the indicated efficiency of different CI combustion concepts are plotted as a function of fuel and combustion stratification. Using diesel fuel to achieve PPC is difficult due to its high chemical reactivity and low volatility, while gasoline-like fuels are much more evaporative and resistant to auto-ignition, providing enough time for premixing [10]. High fuel stratification improves the combustion efficiency, controllability and operating range, while NO_x and soot emissions increase. Low fuel stratification levels, on the other hand, decrease NO_x and soot emissions but result in unstable combustion with high CO and unburned hydrocarbons emissions. Hence, PPC relies on an intermediate stratification level, where it combines the best of both concepts.

Figure 1.1: Fuel and combustion stratification for different compression ignition combustion strategies. There is an optimum fuel stratification level, called “stratified enough” by Kalghatgi, where the highest indicated efficiency would be achieved, while NO_x and soot emissions are relatively low. The HCCI and PPC labeled images are OH* bandpass images in a light-duty optical engine, while the diesel labeled image is combustion luminosity acquired in a heavy-duty optical engine.



Knowledge gap

Dempsey et al. tried to zoom in on fuel stratification of partially premixed concepts to provide a perspective on gasoline LTC [10]. They categorized fuel stratification into three different levels, namely, partial fuel stratification (PFS), moderate fuel stratification (MFS), and heavy fuel stratification (HFS) based on different injection strategies and timings. However, such

a categorization of fuel stratification demands a quantitative index for stratification, a robust, unique and objectively determined parameter which allows to meaningfully compare stratification of fuel, temperature and combustion for different operating conditions, engines, injection strategies. Such a parameter can help to precisely locate the “stratified enough” region in Fig. 1.1. Moreover, combustion stratification is the final outcome of fuel, thermal and turbulence stratification, which all affect the heat release rate behavior and production of emissions. Further understanding of PPC requires the study of all aspects of stratification, in the end allowing to implement the concept in a practical way.

1.3 Research objectives

This thesis presents an optical investigation of different aspects of stratification in partially premixed combustion. Using various laser and optical diagnostic techniques in a light duty optical engine is the main path to meet the following objectives:

- Better understanding of the concept of Partially Premixed Combustion by investigation of different aspects of stratification, including combustion, fuel, thermal and turbulence during this phenomenon.
- Defining a meaningful index for stratification.
- Quantification of the outcome of laser diagnostic techniques.
- Sharing of experimental results to help other researchers, particularly those involved in numerical studies.

1.4 Thesis outline

The experimental setup, light-duty optical engine and overall operating conditions used throughout this study are described in chapter 2. Details regarding the applied optical diagnostic setups and operating conditions are separately addressed in each individual chapter.

At the beginning of this study, the overall PPC operating conditions are identified based on the experimental setup explained in chapter 2. The scope of chapter 3 is to investigate the ignition sensitivity of PPC to the injection timing at different injection pressures. High-speed shadowgraphy is used to visualize fuel injection and evaporation at different Start of Injections (SOI). Spray penetration and injection targeting are derived from these shadowgraphy recordings. OH^* chemiluminescence is used to study the stratification level of combustion, which is used for interpretation of ignition sensitivity behavior.

Investigation of the origin of light emission during PPC is the subject of chapter 4, where further understanding regarding the effect of stratification on combustion behavior and chemical mechanisms is derived from high-speed spectroscopy measurements. Chemiluminescence and thermal radiation are expected to be the dominant sources of light emission during combustion.

A method has been developed to distinguish chemiluminescence from thermal radiation, and different chemiluminescing species (i.e., OH^* , CH^* and C_2^*) could be identified. Different combustion modes and global equivalence ratios are analyzed in this manner. Some optical diagnostic aspects are also analyzed, such as adequacy of using bandpass filters, and finding a proxy for equivalence ratio during combustion.

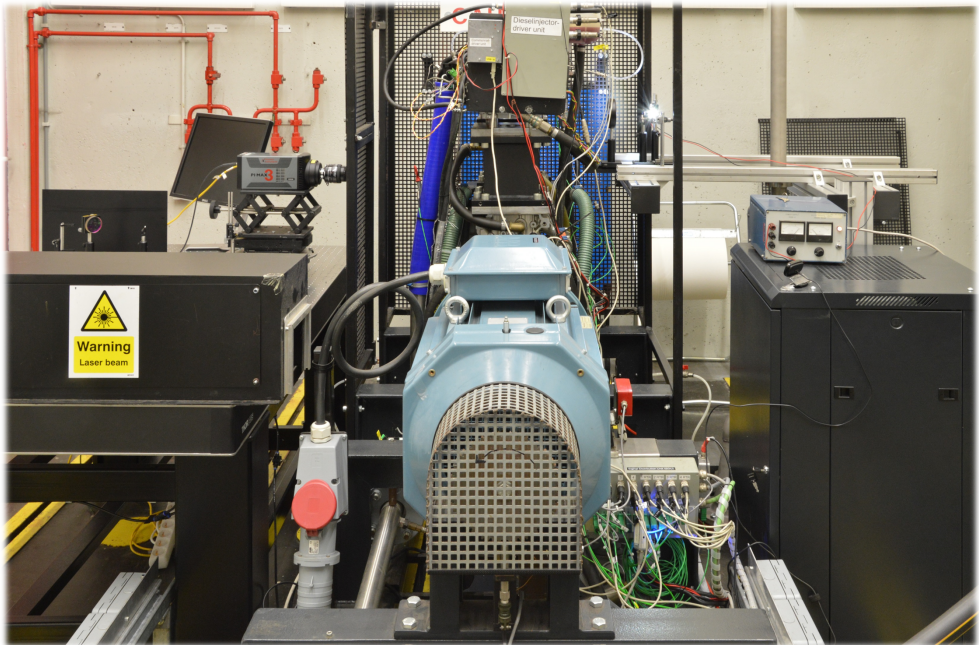
As discussed in this chapter, there is an optimum stratification level (in terms of fuel and combustion) in which a high indicated efficiency can be achieved while maintaining low NO_x and soot emissions. In order to compare stratification levels of different PPC strategies or other combustion concepts, an objective and meaningful definition of "stratification level" is required. Such a definition is currently lacking; qualitative/quantitative definitions in literature (as also used in chapter 3) cannot properly distinguish various levels of stratification. The main purpose of chapter 5 is to objectively define a combustion stratification index based on high speed OH^* bandpass imaging, which provides spatial information regarding heat release based on the results of chapter 4. Stratification essentially being equivalent to spatial structure, the definition is based on two-dimensional Fourier transforms of photographs of OH^* chemiluminescence. Various experimental points are evaluated, with injection timings in the homogeneous regime as well as in the stratified PPC regime. Two-dimensional Fourier transforms translate these chemiluminescence images into a range of spatial frequencies. The frequency information is used to define combustion stratification, using a normalization procedure.

Determining the optimal stratification level of fuel, being the main controlling parameter of PPC, has been a challenging issue. The main objective of chapter 6 is to measure/estimate the in-cylinder fuel and temperature distributions quantitatively based on fuel tracer Laser-Induced Fluorescence (LIF), and to investigate the effects of fuel stratification on PPC. Different fuel stratification levels from homogeneous to highly stratified are studied by sweeping the start of injection. Quantification of fuel tracer (toluene) LIF images is based on the temperature dependency of the toluene fluorescence signal, combined with a comprehensive thermodynamic model, resulting in both temperature and fuel distributions. Quantified results of the fuel distribution are linked to crank-angle resolved OH^* bandpass images (presented in chapter 5) and spectroscopy measurements (presented in chapter 4). Fourier-based stratification analysis proposed in chapter 5 is also implemented as an index for fuel stratification.

Flow characteristics during injection and mixing time is one of the major parameters which affect the level of fuel and combustion stratification of PPC. The scope of chapter 7 is to investigate the fluid flow characteristics of PPC at different injection timings. To this end, high-speed Particle Image Velocimetry (PIV) is implemented to measure fluid flow characteristics, including the flow fields, mean velocity and cycle-resolved turbulence, inside the piston bowl as well as in the squish region. Two injectors, having 5 and 7 holes, are compared to see their effects on fluid flow and heat release behavior for different injection timings. Reactive and non-reactive measurements are performed to distinguish injection-driven and combustion-driven turbulence. The effects of turbulence level on the air/fuel interaction, level of fuel stratification and combustion duration are discussed.

The study is concluded in chapter 8, by means of a general discussion on the obtained results, and suggestions for future work.

Experimental Set-up



This image is showing the Volvo D5 optical engine setup used by the author at TU/e.

2.1 Introduction

The overall engine setup and operating conditions, used throughout this study, are explained in this chapter. The optical engine setup, used by the author at TU/e, is provided by Shell Global Solutions, developed in Lund University, and is one of the three nominally identical setups which are located at Lund University and Imperial College London as well.

2.2 Light-duty Optical Engine

A five-cylinder Volvo D5 light-duty direct injection (DI) engine is used throughout this study. The engine is modified for optical access according to the Bowditch design [11]. One of the engine cylinders is equipped with a cylindrical quartz liner with a height of 25 mm. The other cylinders are deactivated by disconnecting the cylinder head from the engine block and connecting the latter only to the optical cylinder based on a piston and cylinder extender. The quartz liner allows for wide optical access through the combustion chamber from the side (full engine bore diameter). A cross-section schematic of the optical engine is given in Fig. 2.1. An extended optical piston with a slot in the side is used for the optical cylinder while other pistons are equipped with counterweights to compensate for the extra mass of the optical piston extension. The slot in the side of the extended piston provides space for a stationary 45° tilted mirror. A flat optical piston is used in this study except for the PIV measurements (chapter 7) of which the setup will be discussed in section 2.7. On one hand, this flat piston geometry decreases the amount of premixing with respect to the geometry of a piston bowl. Furthermore, fuel is more likely to end up in the crevice volume [12]. On the other hand, the advantage of a flat piston over a re-entrant bowl is that the imaging is hardly affected by optical distortion. Distortion correction for the re-entrant piston bowl geometry is challenging for chemiluminescence imaging, since spatial position inside the cylinder along the line-of-sight of the camera is undefined.

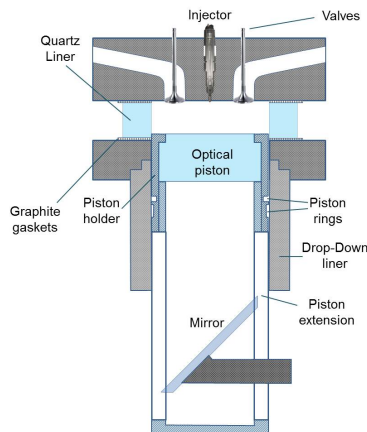


Figure 2.1: Schematic of the Volvo D5 optical engine. The engine has a side optical access through a cylindrical quartz liner with a height of 25 mm, and a bottom optical access through an optical piston and a stationary 45° tilted mirror.

Engine specifications and operating conditions are presented in Table 2.1. Note that 0 CAD

(crank angle degree) marks firing TDC throughout this study. The compression ratio of the engine is decreased to 12.6 to protect the optical parts against high pressure. Moreover, a high compression ratio is not essential to study fundamentals of PPC.

Table 2.1: Volvo D5 optical engine specifications.

Displacement volume	480 cm ³
Bore	81 mm
Stroke	93.2 mm
Connecting rod length	147 mm
Compression ratio	12.6
Squish height	7.077 mm
Number of valves	4
Inlet valve close	-140 CAD
Swirl ratio	1.8
Intake pressure	1.2 bar
Cylinder wall temperature	363 ± 2 K
Coolant temperature	348 ± 2 K

2.3 Fuel System

The complex chemical composition of commercial fuels leads to the use of surrogate fuels, or model fuels, which are simplified fuels used for experimental and modeling work. Such surrogate fuels are designed to have similar relevant properties to full distillate fuels [13]. However, they contain only a certain set of chemical constituents, so that modeling can be done more accurately. PRF70, a blend of the two primary reference fuels (n-heptane/iso-octane), is used as fuel in this study, considering its low-reactive characteristics [14] which extends the ignition delay of PPC combustion at elevated loads. On volume basis, PRF70 contains 70 % iso-octane and 30 % n-heptane. Since the fuel is a pure reference fuel, its Research and Motor octane numbers (RON and MON) are identical by definition. The engine can operate using two distinct injection systems: high pressure Direct Injection (DI) which is mainly used in this study, and port fuel injection, which is used when a homogeneous fuel/air mixture is needed.

Using DI, the fuel is led through a filter to a low-pressure pump and from there to the high-pressure pump via a heat exchanger. The pressure in the common rail is delivered by the high-pressure pump. The fuel is then directly injected into the cylinder by a 7-hole injector. The injection timing, injection duration and fuel pressure in the common rail can be controlled. Specifications of the fuel system and the injector are presented in Table 2.2.

Using port fuel injection, the fuel is pumped by the same low pressure pump as in DI mode. The actual pressure can be controlled by a parallel connected pressure regulator. In contrary to DI mode, the fuel is then led to the port fuel injector. This injector has been installed in the inlet manifold exactly on top of the intake valve. The fuel is injected onto the hot surface of the

Table 2.2: Specification of the direct injection system.

Fuel	PRF70
Fuel injection system	Bosch common rail system
Injector type	solenoid
Number of injector holes	7, equally spaced
Injector umbrella angle	140°
Injector hole diameter	140 μm

intake valve, where it evaporates immediately. Both fuel injectors are calibrated: the amount of injected fuel is measured at different injection pressures and durations. The calibration procedure, observations and data can be found in Ref. [15].

2.4 Engine Intake

The engine intake state can be entirely conditioned, i.e. composition, temperature and pressure are all controlled. The mass flow of the intake air is measured using a mass flow meter before it is led through a heat exchanger. EGR is simulated by diluting the intake air with nitrogen. Any percentage of oxygen up to 21 vol. % can be supplied using this system and the ignition delay variation compared to the real EGR system would be less than 1 % for low EGR percentages, considering the PRF as the fuel [16]. Intake pressure and temperature are also controlled using a compressor and heater. The swirl ratio is adjusted by a throttle which regulates the amount of intake through each of the two intake valves. The swirl ratio is defined as the average angular velocity of the rotating flow normalized by the angular velocity of the crankshaft; it is kept constant at 1.8 throughout this study.

2.5 Heat Release Rate Analysis

An AVL GU13P pressure transducer coupled to a KISTLER 5011 charge amplifier is used to measure the cylinder pressure every 0.20 CAD (sampling frequency of 36 kHz). The heat release analysis of the pressure trace is performed using Eq. (2.1), involving a single-zone thermodynamic model, including the Woschni heat-loss model and a crevice volume model [17, 18]:

$$\frac{dQ_{hr}}{d\theta} = \frac{\gamma}{\gamma - 1} P \frac{dV}{d\theta} + \frac{1}{\gamma - 1} V \frac{dP}{d\theta} + \frac{dQ_{cr}}{d\theta} + \frac{dQ_{ht}}{d\theta} \quad (2.1)$$

in which, dQ_{hr} is heat release [J], the CAD is represented as θ , P is the in-cylinder pressure [N/m^2], V is the in-cylinder volume [m^3], dQ_{cr} is the energy loss due to crevice volume [J], dQ_{ht} is the in-cylinder heat transfer [J], and γ is the heat capacity ratio of the mixture considering its temperature (estimated from ideal gas law). dQ_{cr} and dQ_{ht} are determined based on the work

of Gatowski [18] and Woschni [17], respectively, in which constant parameters are chosen in such way that motoring heat release rate would be constant at zero. A 5th order Hann window function is applied to suppress noise on the pressure trace and heat release rate.

2.6 Operating Conditions

The engine is operated at 1200 rpm by using an electromotor. A so-called “skip-fire” mode (once every 10 engine cycles) is used to reduce the risk of liner failure due to thermal and mechanical loads, and the required cleaning frequency of the optical parts. The intake pressure is always kept constant at 1.2 bar (absolute) and the intake temperature is tuned based on the purpose of the study. If the intention is to keep the CA50 constant, the intake temperature has been varied between 323 and 423 K. If the aim is to study ignition timing, the intake temperature is kept constant at 348 K.

A single injection strategy is used throughout the study. In order to investigate different stratification levels for PPC, the start of injection (SOI) is typically swept from -340 to -10 CAD. Different injection pressures are used ranging from 420 to 850 bar, although most of the study is based on an injection pressure of 600 bar, when the effect of injection pressure was not the goal of the investigation. The injection duration, depending on the injection pressure, ranges from 0.6 to 1.0 ms in such way that always 17 ± 2 mg/cycle of PRF70 fuel is injected. The oxygen percentage has been set in the range of 17.8-20 vol. % to achieve a global equivalence ratio around 0.45.

The main restriction while performing experiments is the fact that the quartz liner is fragile compared to a metal housing. Consequently, the in-cylinder pressure is kept below 70 bar and the temperature of the quartz liner below 368 K, while maintaining an indicated mean effective pressure (IMEP) around 4 bar, which is representative for a low load condition. The coolant temperature is always kept constant at 348 K.

2.7 Experimental Setup for PIV measurements

The high-speed PIV measurements, presented in chapter 7, are performed on a similar Volvo D5 optical engine at Lund university. The engine specifications, setup and operating conditions are exactly the same as the one used for the rest of this study, except for a few differences which are detailed below:

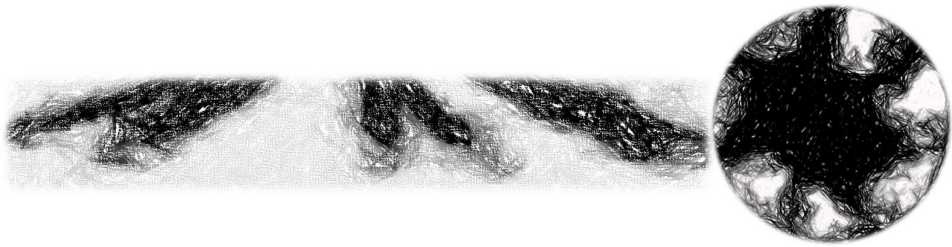
- A quartz piston with a realistic re-entrant bowl geometry, similar to a production-like piston, is used instead of the flat piston geometry. There are two main reasons for this choice. Firstly, the aim of the study was to investigate the flow characteristics for PPC conditions, in which the realistic piston geometry is playing a main role. Secondly, the study was based on a planar measurement with side illumination by a thin light sheet, which makes it possible to correct for the optical distortion.

- By using a re-entrant piston bowl geometry, the engine compression ratio has been reduced from 12.6 to 12.3.
- The swirl ratio has increased from 1.8 to 2.6.
- Two different Bosch injectors with 5 and 7 injection holes are used. The 7-hole injector is exactly the one used for the rest of this study (Table 2.2). The 5-hole injector has also equally spaced holes with the same umbrella angle as the 7-hole injector (140°), but with a larger orifice diameter of 159 μm to deliver almost the same fuel flow rate as the 7-hole injector.
- EGR is simulated by an external conventional diesel burner running stoichiometrically. The engine intake air is diluted by the burner exhaust gas instead of pure nitrogen.
- The engine is driven at 800 rpm instead of 1200 rpm, since the vibration level of the engine at Lund was much higher than that of the one in Eindhoven.

2.8 Conclusion

In this chapter, the engine experimental setup and operating conditions were described. In each of the following chapters, the implemented laser and optical diagnostics on this engine setup are explained, including their detailed operating conditions.

Ignition Sensitivity of PPC



This chapter is based on the following publications:

Izadi Najafabadi, M., Dam, N., Somers, B., Johansson, B., (2016) “**Ignition Sensitivity Study of Partially Premixed Combustion by Using Shadowgraphy and OH* Chemiluminescence methods**”, *SAE Technical Paper* 2016-01-0761, 2016, doi:10.4271/2016-01-0761.

Maghbouli, A., Lucchini, T., D’Errico, G., Izadi Najafabadi, M., Somers, B., (2017) “**Numerical Investigation of PPCI Combustion at Low and High Charge Stratification Levels**”, *SAE Technical Paper* 2017-01-0739, 2017, doi:10.4271/2017-01-0739.

Vallinayagam, R., Vedharaj, S., An, Y., Dawood, A., Izadi Najafabadi, M., Somers, B., Johansson, B., (2017) “**Combustion Stratification for Naphtha from CI Combustion to PPC**”, *SAE Technical Paper* 2017-01-0745, 2017, doi:10.4271/2017-01-0745.

3.1 Introduction

Partially premixed combustion (PPC) is defined as a combustion mode of compression-ignition internal combustion engines that is intermediate between homogeneous charge combustion and diffusion controlled combustion [5, 19, 20]. Relatively high levels of stratification (that is, spatial inhomogeneity in composition and temperature) is one of the main differences of PPC over HCCI, which improves the controllability of this combustion concept. This controllability depends on injection timing and the sensitivity of ignition to stratification [21]. The ignition sensitivity behavior can be investigated from two viewpoints: firstly, by considering the injection process to be the main parameter affecting the mixture inhomogeneity, and secondly, by analyzing the combustion stratification caused by any particular injection strategy. These two aspects are both investigated in this study by applying shadowgraphy and OH^* chemiluminescence imaging in a light-duty optical engine. Analyzing the injection process and combustion stratification are the main objectives of the study.

The shadowgraphy/Schlieren technique is based on a relatively simple concept, and a low cost method for visualizing evaporative sprays [22–24]. Spray penetration and injection targeting (whether and when the sprays hit the liner or piston) can both be seen by visualizing the injection process in side view. However, difficulties with its implementation in an optical engine, especially distortion caused by the optical liner, have limited the number of engine studies using this method [24–28]. The perturbing effect of the optical liner can be compensated by dedicated external optics. There is a limited number of studies which implemented this technique in an optical engine. Ozasa and colleagues (Toyota Research) used the Schlieren technique in an optical engine by shaping the outer surface of the acrylic liner to compensate for the divergence induced by the liner surfaces [26–28]. They could include 67 % of the bore in their field of view (FOV) with a recording rate of 4800 fps, and investigated evaporating gasoline during direct injection. Weinrotter and colleagues implemented the same technique to study spark-plug-assisted HCCI combustion, using a quartz liner and one corrective lens [25]. However, their FOV included only 16 % of the engine bore (128 mm). Finally, Kaiser et al. tried to extend both of the above [24]. They used two corrective lenses before and after the quartz liner to obtain a wide FOV while using a high recording rate of 18 200 fps.

The shadowgraphy part of this research introduces further improvements, not only in experimental design by obtaining a wide FOV while using only one corrective lens and a recording rate of 25 316 fps, but also in comprehensive post-processing of data by extracting quantified spray penetrations as a function of injection timing and pressure.

OH^* chemiluminescence is spontaneous radiation from the OH radical in one of its electronically excited states (OH^*). OH^* is formed by specific chemical reactions in the heat release zone; the combustion temperature itself is not sufficiently high to produce appreciable amounts of thermal OH^* . Consequently, OH^* chemiluminescence imaging provides line-of-sight information across the imaged volume, and is widely used in literature, as a marker of the heat release location [29–32], to investigate the behavior of combustion. However, mathematical analysis of combustion cloud features based on chemiluminescence images are limited. Zegers et al. investigated the position and size of combustion clouds of PPC combustion by analyzing OH^*

chemiluminescence images in a heavy-duty optical engine [31]. A clear correlation between ignition delay and flame location was observed by them. Tanov et al. analyzed the combustion stratification using various injection strategies in a light-duty optical engine (the same engine as used in this study) [30]. Their results show that the combustion following triple injection is more homogeneous compared to that after single and double injection. However, high distortion of the piston bowl limited their study to only angular stratification analysis of PPC combustion inside a narrow ring of the combustion chamber. The chemiluminescence part of this study improves and expands on that study [30] by considering the largest part of combustion chamber and analyzing both angular and radial stratification as well.

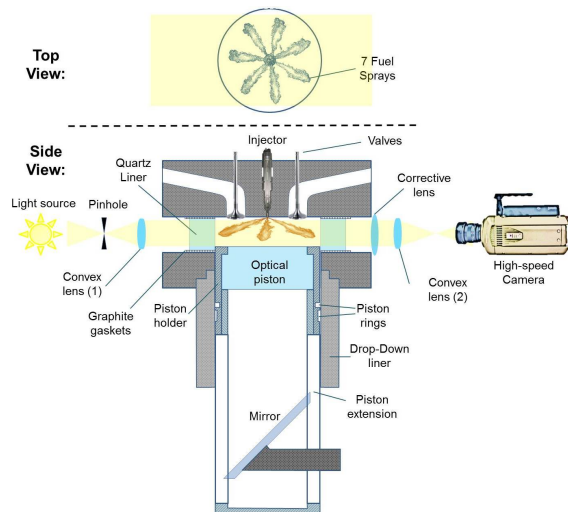
In the end, the CFD results for the same operating conditions as the experimental points are presented for completeness, to better understand the ignition sensitivity of PPC. CFD simulations were performed by Amin Maghbouli from Politecnico di Milano [33].

3.2 Experimental Methods

3.2.1 Shadowgraphy

The aim is to measure the spray penetration and visualize the injection targeting for different injection timings and pressures. To this end, the combustion chamber is illuminated with a collimated beam of light to image the fuel injection in side view (Fig. 3.1) under non-reacting conditions (pure nitrogen).

Figure 3.1: Schematic of shadowgraphy setup. LED light passes through a pinhole which is located at the focal length of a convex lens (1). The convex lens produces a collimated beam which passes through the combustion chamber and later through a corrective lens to compensate for the optical distortion of the cylindrical quartz liner. Another convex lens (2) is used in combination with an objective lens to widen the FOV (the image is flipped). In the end, the shadowgraphy image is recorded by the high-speed camera.



The collimated beam is produced by an LED light source, a wide convex lens (82 mm diameter) and a pin hole between them, located at the focal length of the lens (80 mm). Shadowgraphy imaging is based on the fact that rays of light are diverted when they traverse a medium

with refractive index gradients [23]. When the injected fuel, with a different refractive index compared to the ambient compressed air, is illuminated by a collimated beam through the combustion chamber, some rays will be deflected, while others will not. Individual light rays in the combustion chamber can be absorbed or scattered by the liquid fuel, refracted by the Schlieren effect of the fuel vapor, or just pass through the chamber, effectively without being affected by the injection [22]. As a consequence, the liquid phase of sprays will be seen by the camera as mere darkness, while the vapor phase will show up gray.

In the optical engine, the quartz cylinder behaves as a negative cylindrical lens, causing the collimated beam to diverge. This phenomenon is simulated for the actual quartz liner and shown in Fig. 3.2. The same behavior is also reported by Kaiser et al. [24]. They proposed using two corrective lenses before and after the quartz liner to increase the FOV without distortion. However, only one wide cylindrical lens is used in this study, to compensate only for the beam divergence immediately after the liner, as shown in Fig. 3.1. By using this corrective lens, there are still some minor distortions, which have been corrected by imaging a grid and post-processing of data.

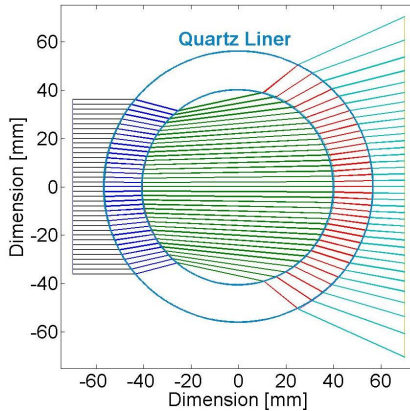


Figure 3.2: Optical distortion by the cylindrical quartz liner. Collimated light rays enter at the left and diverge when leaving the quartz liner at the right, because of different refractive index of quartz compared to air.

High-speed imaging is done using an 8 bit CMOS camera, specifications and settings of which are shown in Table 3.1. A recording speed of 25 316 fps allows to record almost 3.5 frames/CAD and to follow the spray penetration process by approximately 25 images (considering an engine speed of 1200 rpm and injection duration of 7 CAD).

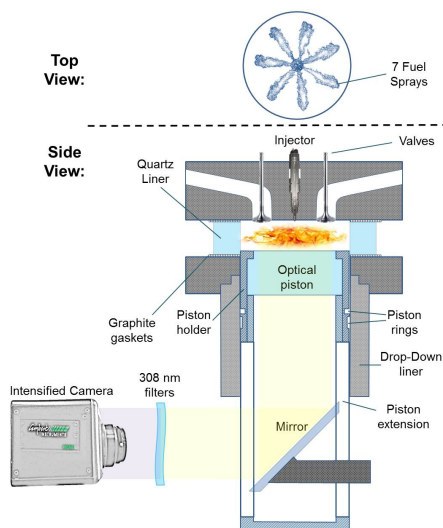
Table 3.1: Camera specifications for shadowgraphy.

Camera	Phantom 5.1
Imaging sensor	8 bit CMOS
Resolution	387 × 96 pixel ²
Frame rate	25 316 fps
Exposure time	3 μs
Objective lens	AF-Nikkor 50 mm 1:1.4D

3.2.2 OH* Chemiluminescence

Crank-angle-resolved OH* chemiluminescence is recorded using a high-speed intensified camera for the same conditions and measurement points as for shadowgraphy experiments (but not simultaneously). A schematic of the experimental setup is shown in Fig. 3.3. The flat optical piston used in this study gives 60 mm optical access of the 81 mm engine bore without any distortion.

Figure 3.3: Schematic of OH* chemiluminescence setup. Combustion luminosity passes through the flat optical piston, is reflected by the stationary 45° tilted mirror, filtered by OH* bandpass filters and in the end, recorded by the high-speed intensified camera.



Specifications of camera, intensifier, objective lens and filters are presented in Table 3.2. A combination of a 315 nm bandpass filter with 20.4 nm FWHM (Full width at half maximum) and a 300 nm bandpass filter with 87.5 nm FWHM is used to reject light with wavelength below 300 nm or above 330 nm, so as to record only OH* chemiluminescence wavelengths (peak emission around 310 nm). Soot luminosity, however, cannot completely be suppressed, and is in fact expected to dominate the recorded luminosity later during the combustion.

Table 3.2: Specifications of camera and optics for OH* chemiluminescence.

Camera	Lambert HiCAM 5000 (built-in intensifier)
Imaging sensor	8 bit CMOS
Intensifier	P46 with 0.2-0.4 μ s phosphor decay time
Intensifier gain	72 %
Resolution	352 \times 352 pixel ²
Frame rate	7200 fps
Exposure time	25 μ s
Objective lens	UV Nikkor 105 mm f/4.5
1 st Filter	315 nm bandpass filter with 20.4 nm FWHM
2 nd Filter	300 nm bandpass filter with 87.5 nm FWHM

3.2.3 Operating Conditions

To investigate the effect of SOI (injection into different thermodynamic situations) on combustion phasing and ignition sensitivity behavior of PPC combustion, SOI is swept from -100 to -12.5 CAD (ATDC) for three different single-injection strategies. These strategies are detailed in Table 3.3 and for all of them the amount of fuel injection is constant at 16 mg/cycle. The engine is run around a gross IMEP of 4.3 ± 0.9 bar to prevent the high pressure rise rate of PPC and HCCI combustion which can damage the optical engine. SOI is swept from -100 to -60 CAD with a step size of 10 CAD, from -60 to -35 CAD with a step size of 5 CAD and from -35 to -12.5 CAD with a step size of 2.5 CAD, in total 19 measurement points for each injection pressure.

Table 3.3: Single injection strategies. Total injected fuel is 16 mg/cycle in all cases.

Case	Injection pressure	Injection duration
I	640 bar	5 CAD
II	500 bar	6 CAD
III	420 bar	7 CAD

25 fired cycles are acquired for each experimental point and results are based on an ensemble average. The intake temperature is kept constant at 348 K, and to isolate the effect of SOI on combustion phasing, the intake pressure and intake oxygen percentage are also kept constant at 1.2 bar and 17.6 Vol. %, respectively. As a consequence, CA50 and IMEP change with SOI. However, it has still been possible to achieve CA50 between 3 and 15 CAD for SOI between -100 and -12.5 CAD. Injection later than -12.5 CAD leads to misfire and really late combustion. Another parameter is also considered to investigate the combustion phasing, named CA50_{abs}. The CA50_{abs} is defined as the crank angle at which 50 % of the total injected fuel is burned while CA50 is the crank angle at which 50 % of the accumulated heat release is achieved.

3.3 Post-Processing

3.3.1 Shadowgraphy Image Processing

The target of shadowgraphy image processing is to derive the spray penetration as a function of crank angle degree for different injection timings and pressures. As shown in Fig. 3.2, even the unperturbed light intensity distribution coming out of the quartz liner is not homogeneous and decreases with distance from the center line. Since the shadowgraphy image processing is based on intensity gradients, the background intensity variation is corrected by:

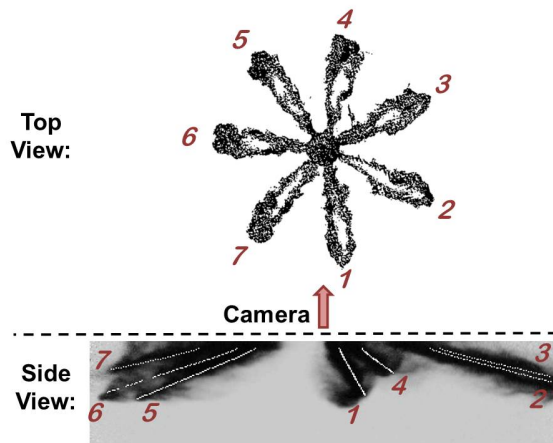
$$I_{corrected_{i,j}} = c \frac{I_{i,j}}{I_{sample_{i,j}}} \quad (3.1)$$

where $I_{corrected_{i,j}}$ is the corrected intensity of the data image (i and j represent pixel position), c is a constant which is considered as 100 here to prevent going beyond 256 intensity limit of 8 bit/pixel, $I_{sample_{i,j}}$ is background intensity of the same pixel derived from a sample image without injection and finally, $I_{i,j}$ is the intensity of the raw data image.

An illuminated rectangular grid, positioned at the center of the combustion chamber, has been used to correct for the minor residual geometrical distortions. A Cartesian coordinate system is considered with an origin at the injector point and all pixels are mapped onto this coordinate system by interpolation using the inserted grid. This map is used for interpreting of final results (spray penetration from injector point).

To trace the spray penetration, 7 lines are defined in a three-dimensional Cartesian coordinate system, each one of which determines the injection path out of one of the injector holes as seen by the camera, based on the 140° injector umbrella angle. Then, these lines are projected onto the focal plane of the camera. Monitoring the intensity values and gradients along these 7 lines, allows to track spray penetration for each spray frame by frame; an example is shown in Fig. 3.4. The presented side-view images of shadowgraphy do not show the intensity gradient between two overlapped sprays (like sprays 2 and 3) because of large contrast in the images. However, there is a detectable distinction between them which is used for the post-processing of the axial penetration. To avoid the probable post-processing errors of side-view overlapped sprays, results are presented by averaging all sprays.

Figure 3.4: 7 sprays and their mapped line paths in the focal plane. The top view is only a schematic of 7 sprays, while the side view is a shadowgraphy post-processed image at -96 CAD for SOI at -100 CAD. White lines show the penetration for each spray.



Pixels along the injection lines with an intensity value less than 10% of the highest possible values are considered as liquid phase. This is based on the range of intensity when liquid phase of fuel hits the liner and makes a stain for the early injection timings (for example -100 CAD). These stains disappear after some crank angles because of evaporation. For early

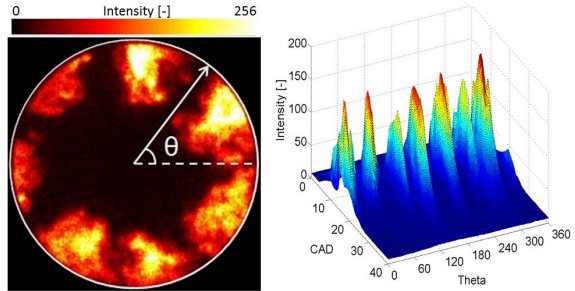
injection timings, sprays 2, 3, 6 and 7 (according to Fig. 3.4) leave the field of view, and are not considered in the final results. Eventually, spray penetration in the z direction is presented by averaging the vertical penetration of all 7 sprays (or less, for early injections).

3.3.2 OH* Chemiluminescence Image Processing

The objective is to find the level of combustion stratification for different injection timings by analyzing OH* chemiluminescence images. As mentioned in the Introduction section, this part of study expands on the earlier research by Tanov et al. [30]. In that research, the angular stratification could only be determined in a narrow ring of the image, while in this study the full image is considered for both angular and radial stratification. To this end, chemiluminescence images are analyzed in a cylindrical coordinate system.

To determine the angular stratification, the intensity is radially averaged and plotted as a function of polar angle (θ). Figure 3.5 shows a typical behavior of PPC combustion by applying this method to each frame (CAD) of an OH* chemiluminescence movie. Based on that, the range of theta can be divided into 7 equal segments, representative of 7 combustion clouds.

Figure 3.5: Typical behavior of intensity as a function of polar angle for PPC combustion. Left: intensity image for a given CAD, right: radially averaged intensity as a function of θ for a sequence of CADs.



Regarding Fig. 3.5, the angular stratification of each image can be defined as:

$$Str_{\theta} = \frac{1}{n} \sum_{i=1}^n \frac{(I_{max} - I_{min})_i}{(I_{max} + I_{min})_i} \quad (3.2)$$

where Str_{θ} is angular stratification, n is number of injector holes, and I_{max} (I_{min}) is the maximum (minimum) radially averaged intensity in the polar angle range of the i^{th} combustion cloud.

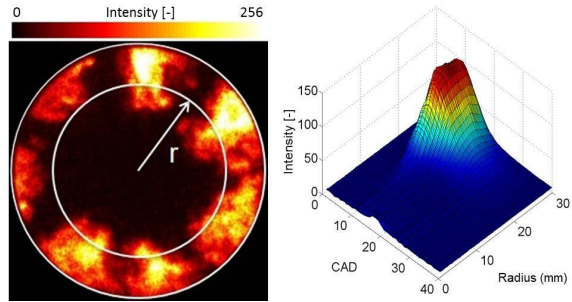
Based on this definition, the swirl motion of combustion clouds does not affect the final stratification results, since each polar segment includes a complete, be it composite combustion cloud. The difference of maximum and minimum angular intensities is normalized by the sum of them in this definition instead of normalizing by the mean intensity of whole image, as was used in the literature [30]. This way of normalization, used in Eq. (3.2), limits the stratification level between 0 and 1 and allows to compare different cases.

To analyze radial stratification, the intensity is averaged over θ for each radius (r) and is plotted as a function of r for different crank angle degrees (Fig. 3.6). Regarding Fig. 3.6, radial stratification of each image can be defined as:

$$Str_r = \frac{(I_{max} - I_{min})_{[0:R]}}{(I_{max} + I_{min})_{[0:R]}} \quad (3.3)$$

where Str_r is radial stratification, R is the radius of the FOV (30 mm in this study), I_{max} is maximum radial intensity and I_{min} is the minimum radial intensity over all possible radii. Note that I_{max} (I_{min}) is the maximum (minimum) circularly averaged intensity in Eq. (3.3) while it is the maximum (minimum) radially averaged intensity in Eq. (3.2).

Figure 3.6: Typical behavior of intensity as a function of radius for PPC combustion. Left: intensity image for a given CAD, right: circularly averaged intensity as a function of θ for a sequence of CADs.



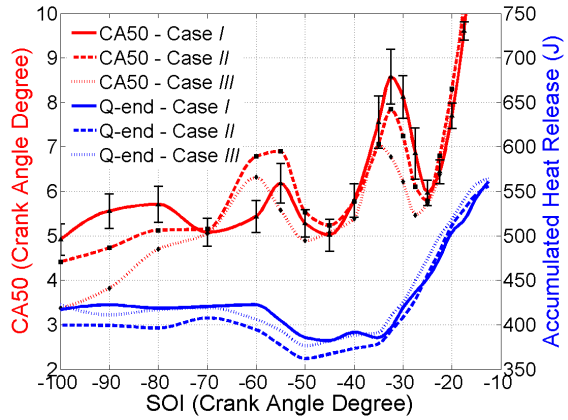
3.4 Results and Discussions

3.4.1 Ignition Sensitivity to Injection Timing

SOI is swept from -100 to -12.5 CAD to see its effect on CA50 and accumulated heat release for different injection pressures (see Table 3.3). Results of CA50 and accumulated heat release are shown in Fig. 3.7. For the sake of clarity, representative standard deviation error-bars are only presented for one set of results (also for other figures in this section). Accumulated heat release (net) is used to compare the combustion efficiency, since the same amount of fuel is injected for all experimental points. Unexpectedly, there are two regions of SOI over which the CA50 is advanced with increasing SOI. Firstly, it happens around -50 CAD, where the accumulated heat release is decreasing. Secondly, CA50 drops around -30 CAD while the accumulated heat release is strongly increasing (moving toward high-efficiency PPC region).

Injection timing between -100 and -60 CAD creates an almost homogeneous mixture, causing an HCCI-like combustion behavior. Experiments in this region confirm that combustion phasing behavior is independent of injection timing, while it is highly sensitive to intake temperature fluctuations as well as engine's thermal status. As a consequence, CA50 behavior in this region is governed by small differences in engine's thermal status. This fact is also shown in Fig. 3.8 where ignition sensitivity is calculated for each injection timing. To assess the ignition

Figure 3.7: CA50 and accumulated heat release (Q-end) as a function of SOI for different injection pressures. Standard deviation error-bars are shown only for case I for the sake of clarity. CA50 is representative of combustion phasing, while accumulated heat release is representative of combustion efficiency, since the same amount of fuel is injected for all operating conditions.



sensitivity, SOI has been advanced and retarded for 2 CAD for each measurement point (2×19 extra measurement points) and the CA50 variation has been measured for this small SOI differential. To this end, ignition sensitivity is defined as:

$$S_{ign} = \frac{d(CA50)}{d(SOI)} \quad (3.4)$$

where S_{ign} is ignition sensitivity, $d(CA50)$ is CA50 differential and $d(SOI)$ is SOI differential.

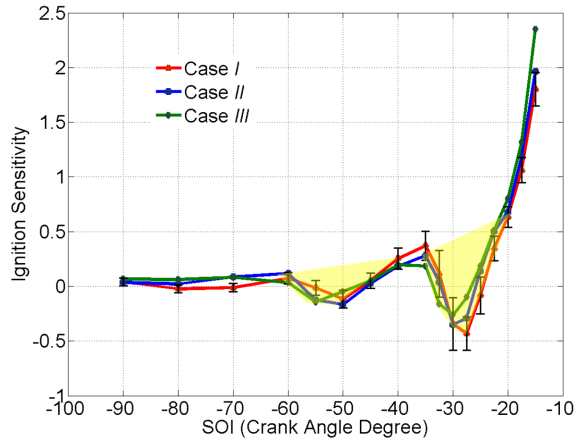
The ignition sensitivity to injection timing is close to zero for the SOI up to -60 CAD. There is a significant positive correlation between injection timing and combustion phasing for SOI in the range between -25 and -12.5 CAD. These results are in line with the ignition sensitivity study by Yin and co-workers [21]. Combustion phasing in this CAD range is highly repeatable. At intermediate SOI from -60 to -25 CAD, the CA50 and ignition sensitivity act unexpectedly, particularly around -50 and -30 CAD where the combustion is advanced by retarding the injection timing. Considering a hypothesis of “later injection, later combustion” for late injection timing, two unexpected regions are highlighted (yellow) in Fig. 3.8. These two regions correspond to those in Fig. 3.7; they are discussed below.

3.4.2 Spray Penetration and Targeting

The purpose of shadowgraphy experiments was to study injection targeting and spray penetration. Injection targeting can in principle be investigated just by visualization, while spray penetration needs quantification of measurements.

Figure 3.9 shows representative side views of injection targeting at four injection timings: -100 , -50 , -30 and -20 CAD at injection pressure of 420 bar (case III), illustrating four possibilities of injection targeting. Early injection timing (-100 CAD) causes liquid fuel to hit the liner, which is obvious in this figure. By the end of injection, this liquid stain on the liner evaporates after

Figure 3.8: Ignition sensitivity to injection timing for different injection pressures. Regions of unexpected behaviors (low and negative ignition sensitivity values) are highlighted (yellow).



some crank angle degrees. By retarding the injection, these stains get smaller and smaller, because higher pressures and temperatures restrict spray penetration.

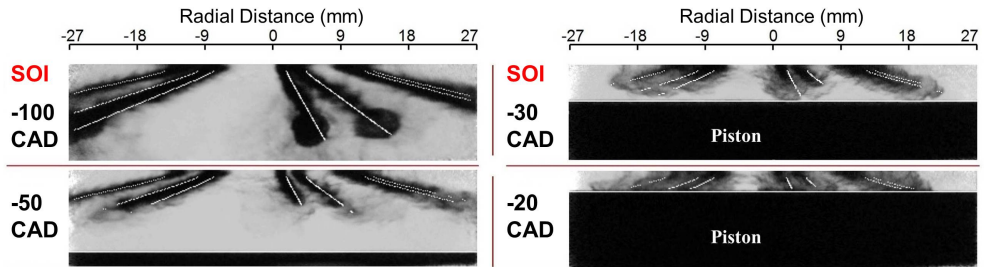
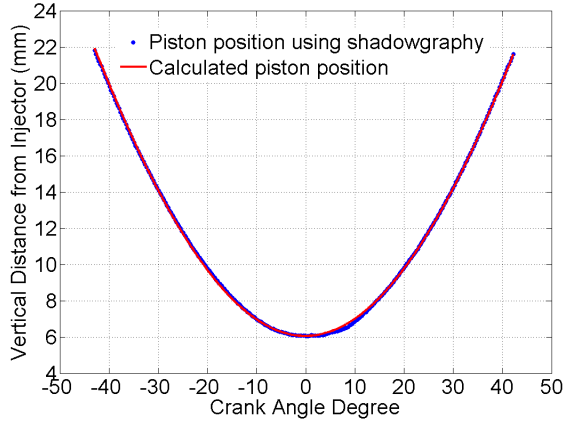


Figure 3.9: Injection targeting based on side view shadowgraphy images. See Fig. 3.4 for spray layout. Note that for SOI at -100 CAD, sprays 1 and 4 terminate in blobs, indicating that they have hit the liner. For the other sprays, this happens outside of the field of view.

For injection timing from -50 CAD onwards, the liquid phase does not hit the liner any more. However, now the piston is getting closer and closer to the injector and finally is hit by the liquid phase at SOI of -30 CAD. It should be noted that it is the piston which hits the spray rather than vice versa, since the liquid penetration is already steady. At later injections, this situation changes. Then the liquid phase hits the piston as it develops towards its stable liquid length. This phenomenon is evident at SOI of -20 CAD when the sprays spread over the piston crown (Fig. 3.9).

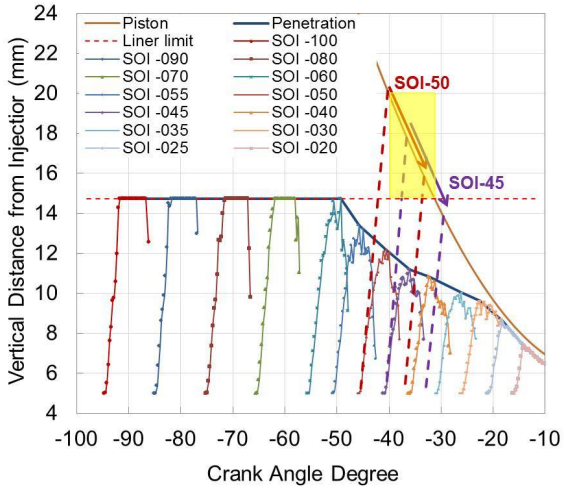
Quantified spray penetration, based on shadowgraphy measurements, requires a reference for spatial calibration. To this end, the piston position is auto-tracked through the high intensity gradient at the top edge of piston. Then the tracked piston position is corrected for image deformation during the shadowgraphy movie, to extract the piston crown distance from the injector as a function of crank angle degree. Finally, this measurement is compared to the piston motion equations [34]. Figure 3.10 shows a good level of agreement between quantified shadowgraphy measurements and numerical calculations.

Figure 3.10: Validation of position tracking by using shadowgraphy method. Vertical distance between the piston crown and the injector is calculated based on engine geometry, and compared to shadowgraphy results.



Based on the image processing method described earlier, spray penetration as a function of crank angle degree is derived for different injection timings and injection pressures. Figure 3.11 shows vertical spray penetrations for case III. Piston motion is also shown, to illustrate its collision with the sprays. Considering the injector umbrella angle of 140° , the vertical position where the sprays would hit the liner is shown in Fig. 3.11 as “Liner limit”. When spray penetration reaches this line, it means it hits the liner and then flows downwards over the liner.

Figure 3.11: Spray penetration (liquid) as a function of crank angle for different injection timings at injection pressure of 420 bar (case III). Dashed lines are representative of vapor penetration based on visual inspection. The highest probable region (time-location) for fuel to be trapped in the crevice volume is highlighted (yellow).



Four injection targeting regions described earlier can also be seen in the quantified measurements. Injection timing from -100 to -60 CAD results in sprays hitting the liner. At SOI of -30 CAD, the piston hits the sprays when their maximum penetrations are stabilized. By retarding the injection timing still further, it is actually the piston which limits the spray penetration.

Probable trapping of fuel in the crevice volumes can also be seen in Fig. 3.11, based on vapor penetration data which are extracted from visual inspection of shadowgraphy images. If fuel reaches the liner exactly when the piston is there, it experiences the highest probability to be

trapped in the crevice volume. Considering an injection duration of 7 CAD, this critical region is highlighted by yellow color in Fig. 3.11. Vapor penetrations for SOI of -50 and -45 CAD are also shown by dashed lines. As shown in the figure, SOI of -50 CAD produces sprays with the highest contribution in the critical region, followed by SOI of -45 CAD. A large amount of fuel can be trapped in the significant crevice volume, caused by the relatively large piston clearance of the optical engine (1 mm clearance), leading to a low combustion efficiency (around 68%) in this injection timing region (around -50 CAD). This is exactly why the accumulated heat release decreases in this region, which was shown in Fig. 3.7.

Interestingly, ignition sensitivity is also negative in this region (SOI around -50 CAD) as demonstrated in Fig. 3.8. Ignition sensitivity is a function of CA50 which is dependent on accumulated heat release. Hence, decreasing the accumulated heat release is actually causing the CA50 to decrease as well in this region. This is well shown in Fig. 3.12 where CA50_{abs} which is independent of accumulated heat release is compared to CA50. Behaviors of CA50 and CA50_{abs} are always the same except for a region between -60 to -40 CAD where CA50_{abs} does not change which means its sensitivity to injection timing is zero.

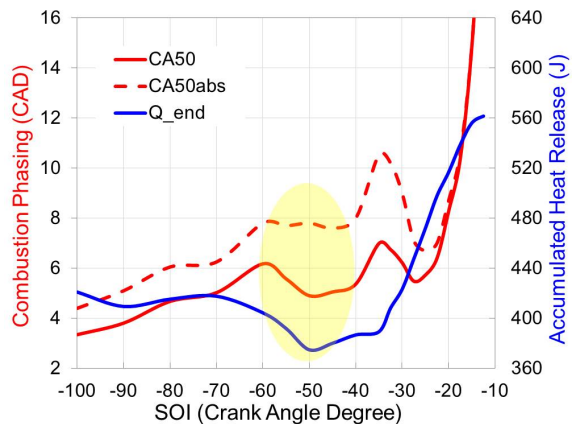


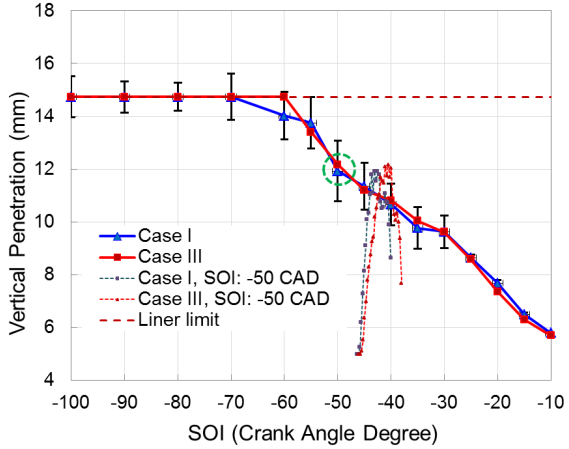
Figure 3.12: Comparison of CA50 and CA50_{abs} for case III. CA50_{abs} is defined as the crank angle at which 50% of the total injected fuel is burned (280 J for this case). Accumulated heat release is also shown for better comparison.

In general, the first region of negative ignition sensitivity values (yellow region in Fig. 3.8) is caused by relatively large amounts of trapped fuel in the crevice volume. However, considering an absolute value of heat release instead of CA50 as a representative of combustion phasing causes these negative values of ignition sensitivity to disappear. Indeed, ignition sensitivity is dependent on definition of combustion phasing for this range of injection timing, where a significant amount of fuel is trapped in the crevices. Note that this effect would be less of a concern in a metal engine, where the crevice volume is much smaller than in an optical engine.

To see the effect of injection pressure on spray penetration, vertical spray penetration as a function of injection timing for two different injection pressures (420 and 640 bar) is shown in Fig. 3.13. The effect of injection pressure on liquid penetration is negligible as expected [35, 36]. However, the injection pressure does affect the spray velocity, which is demonstrated in Fig. 3.13 for the SOI of -50 CAD (maximum spray penetrations are highlighted by the green circle, while time-resolved spray penetrations are shown by dashed lines for different injection pressures). Higher injection pressure of case I causes the sprays to reach their maximal penetration faster

than case *III*. This higher penetration speed provides more time and higher kinetic energy for better mixing, and should result in more homogeneous combustion. This effect is investigated in the next section, where stratification levels of combustion are analyzed for different situations.

Figure 3.13: Comparison of maximum spray penetration for different injection timings and pressures: cases *I* and *III*. Time-resolved spray penetration for SOI at -50 CAD are also shown by dash lines for cases *I* and *III*. Their maximum spray penetrations are indicated using a green circle.



3.4.3 Combustion Stratification

Angular and radial stratifications are calculated for each crank angle degree, based on the chemiluminescence image processing method described earlier. Figure 3.14 shows the stratification level (average of angular and radial) as a function of crank angle degree for four different injection timings: -100 , -45 , -25 and -15 CAD. Some OH^* chemiluminescence images of the same cases are included to provide a better understanding of the phenomena. As a drawback of the proposed stratification method, a baseline value of 0.1 is observed when there is no combustion occurring. This is due to camera noise, which because of the employed normalization procedure result in a non-zero stratification level of 0.1.

For early injection at -100 CAD, the combustion is fast and almost homogeneous in comparison with later injection timings. By retarding the injection timing to -45 and -25 CAD, there is less and less time for mixing of fuel and air, resulting in a more and more stratified combustion. This behavior is obvious in both OH^* chemiluminescence images and quantified stratification results. Situations are a little different for injection timing of -15 CAD, where ignition delay increases due to the temperature drop after TDC. This higher ignition delay provides more time for mixing and is responsible for the break in the trend of increasing stratification.

To derive a single parameter to characterize the level of stratification for a specific injection timing, the 90th percentile of the crank-angle-resolved stratification level is used. By applying this method, the representative stratification level of a movie would depend on the maximum stratification values. By considering maximum values instead of averaging, results are independent of the combustion duration and it is also possible to avoid the probable effect of soot luminosity later during the combustion (when the mixture is cooling down). Figure 3.15 shows the angular, radial and mean levels of stratification as a function of injection timing based on

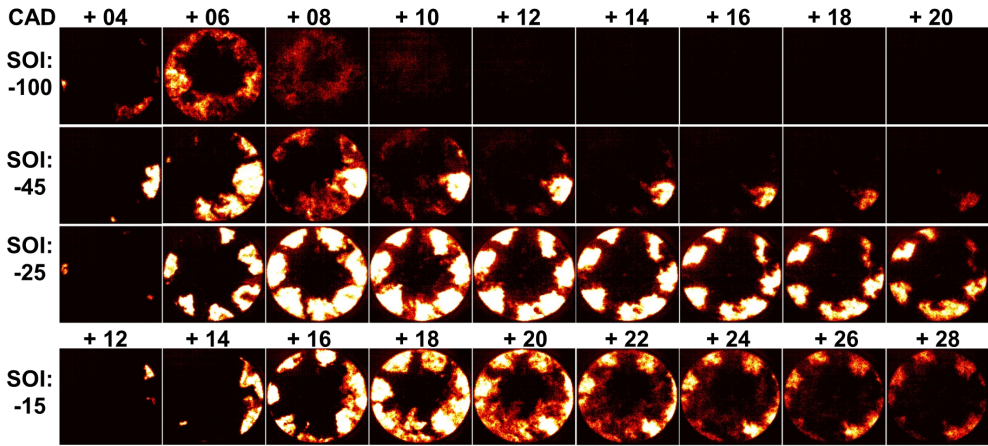
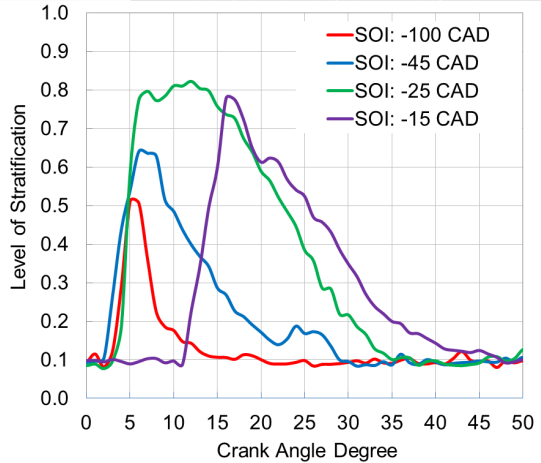


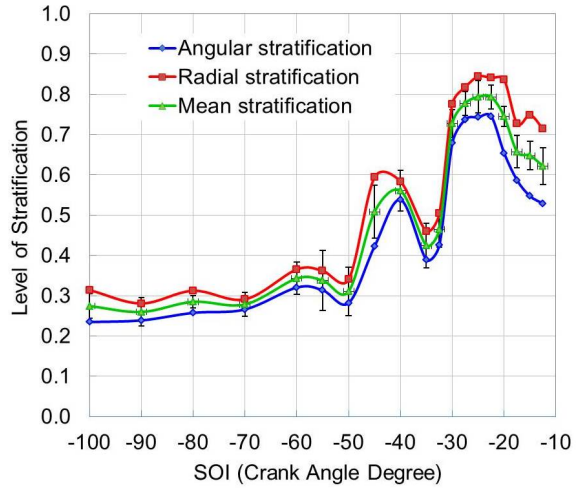
Figure 3.14: Spontaneous luminescence images and stratification level as a function of crank angle degree for four different injection timings: -100 , -45 , -25 and -15 CAD at injection pressure of 420 bar (case III). Note that SOI at -45 CAD is a transient point from the almost homogeneous combustion of SOI -100 CAD to the stratified combustion of SOI -25 CAD. This is the reason that hole to hole variation of the injector causes different combustion behaviors.



this method. Interestingly, the behavior of angular and radial stratifications is exactly the same. However, the radial stratification is slightly higher than the angular stratification for this particular injection system.

These quantified stratification results allow to interpret combustion phasing behavior of different injection timings. Combustion stratification is low and almost stable for early injection from -100 to -50 CAD as expected. Remarkably, there is a reverse correlation between combustion phasing (Fig. 3.7) and stratification level (Fig. 3.15) for injection timing of -45 to -12.5 CAD. There are two jumps in the stratification level, around -45 and -25 CAD, while combustion phasing advances at exactly these injection timings (valleys in Fig. 3.7). The first jump occurs when the injection timing moves out of the critical fuel trapping range (Fig. 3.11), leading to higher local equivalence ratios and higher combustion stratifications. The second jump starts exactly at SOI of -30 CAD when the piston hits the liquid core at -20 CAD (illustrated in Fig. 3.11). The temperature of the piston crown is much lower than the temperature of the compressed air at -20 CAD causing the fuel evaporation process to slow down. This is negatively affecting the mixing process, causing more fuel stratification and as a result, more

Figure 3.15: Comparison of angular and radial combustion stratifications for different injection timings (case III). Note that the mean stratification can be representative of both angular and radial stratifications.



combustion stratification. Actually, the second yellowish region in Fig. 3.8 (negative ignition sensitivity values around -30 CAD) is caused by the high level of stratification for this injection range which is dominated by the collision of piston and liquid core of sprays. For the late injection timings, around -20 and -15 CAD, the higher ignition delay provides more time for mixing due to the lower temperature after TDC, causing the stratification level to decrease.

The same angular stratification analysis is implemented to study the combustion stratification for naphtha and diesel as well in another optical engine based on high-speed luminosity images [37]. The maximum combustion stratification and the mean intensity with respect to SOI for naphtha and diesel are presented in Figs. 3.16a and 3.16b, respectively. By retarding the injection timing from -30 to -20 CAD, the level of combustion stratification increases for both fuels, similar to what seen in Fig. 3.15 for PRF70, while for the later injection timing around -20 and -10 CAD, the higher ignition delay provides more time for mixing, stopping the increasing trend of stratification level. More information regarding the effect of fuel on combustion stratification and emissions based on the same stratification analysis method can be found in Refs. [37–40].

Similar trends of combustion stratification are seen for different injection pressures, as presented in Fig. 3.17, showing only minor differences. By averaging the stratification level of different injection timings from -100 to -12.5 CAD for each injection case, stratification level as a function of injection pressure is obtained. Lower injection pressure causes relatively higher combustion stratification, while higher injection pressure leads to more homogeneous combustion. The higher kinetic energy of the injection case I (followed by case II), as well as providing a little more time for mixing (shorter injection duration), leads to more homogeneous mixture and, consequently, lower level of combustion stratification. Indeed, injection pressure is inversely affecting combustion stratification, but its effect is negligible compared to the effect of injection timing on the combustion stratification.

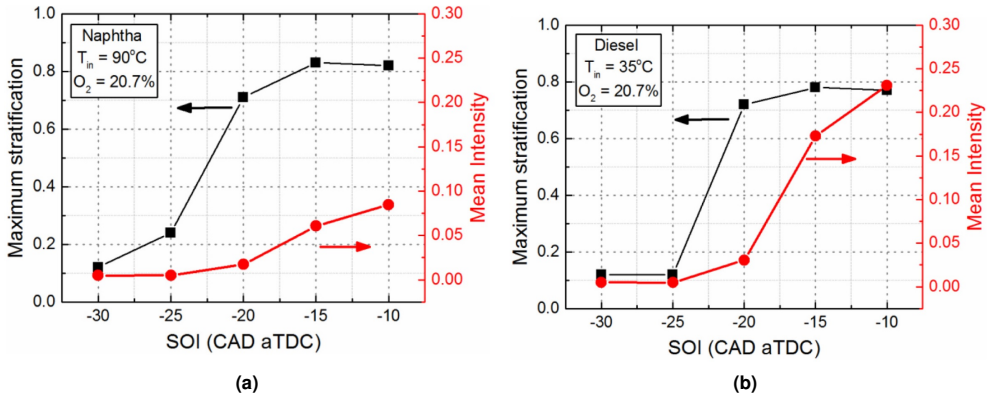
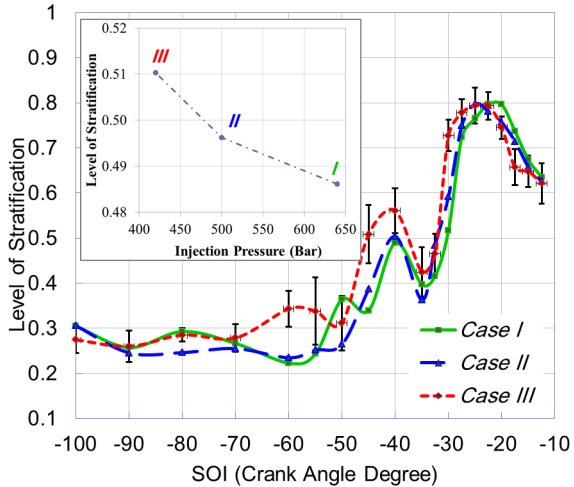


Figure 3.16: Maximum stratification and mean intensity with respect to SOI for naphtha (a) and diesel (b).

Figure 3.17: Effect of injection pressure on combustion stratification (mean of angular and radial stratifications) for different injection timings. The inner graph shows the average of combustion stratification from -100 to -12.5 CAD for each injection case (as a function of injection pressure).



3.4.4 Comparison with CFD Results

Multi-dimensional CFD simulations for the SOI at -80 and -40 CAD (case III), as low and high air-fuel stratification cases, were performed. A Spray Oriented sector grid was generated with considering the crevice volume (to match the engine compression ratio) and seven injector nozzles. Mesh generation was performed based on an automatic grid generation tool [41]. Numerical simulations were conducted using the OpenFOAM open-source code [42] in conjunction with Lib-ICE which is a set of libraries and solvers for comprehensive IC engine simulations [43]. Turbulence was accounted for by Reynolds Averaged Navier Stokes (RANS) formulation and was modeled using the standard $k-\epsilon$ model. The Multi-Zone Well-Mixed model was used as combustion model, and Liu's PRF mechanism [44] with 41 chemical species and 124 chemical reactions was used as reaction mechanism. More details regarding the modeling method can be found in Ref. [33].

Numerical and experimental results of apparent heat release rate (AHRR) are compared for the considered cases in Fig. 3.18a. It can be noted that the time delay between first and second stage ignition was getting shorter by further retarding the start of injection from -80 to -40 CAD ATDC. In other words, it shows that combustion phases faster to the second and main stage heat release in higher air-fuel stratification case.

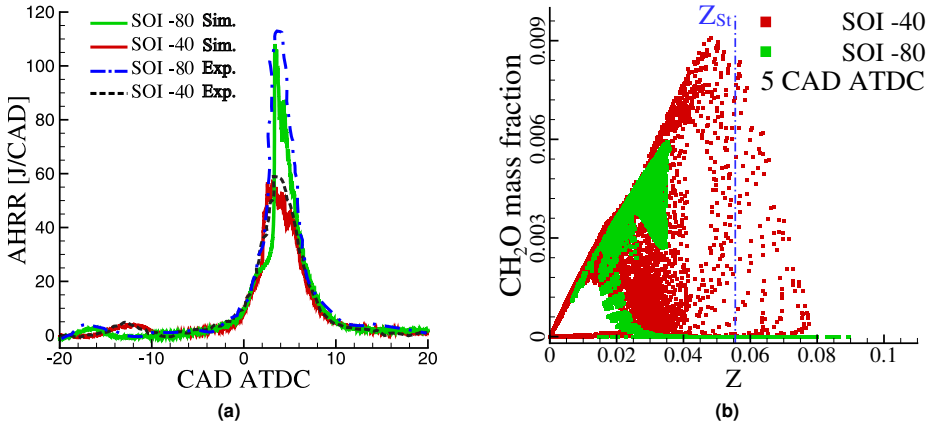


Figure 3.18: (a): Numerical and experimental AHRR comparison of SOI -80 and -40 CAD as representors of low and high mixture stratification levels, respectively. (b): CH₂O mass fractions of SOI -80 and -40 CAD for the whole CFD domain at 5 CAD ATDC (Second stage ignition).

Although it was not for PPC combustion, the inclination toward single stage ignition was also reported by Pei et al. [45] for highly stratified air-fuel charges (ECN Spray A experiments). Pei et al. concluded that there is almost no effect of double stage ignition and negative temperature coefficient in the numerical simulations of Spray A. Similar behavior is found in this study where time delay between first and second stage combustion was shortened by moving to the case with higher stratification. In PPC combustion, observed differences of combustion phasing speeds toward second stage heat release can be considered as a key parameter to provide a better control on timing of the second stage heat release rate. Hence, the important task then would be generating a desired mixture stratification for different engine operating conditions.

In a stratified mixture, availability of a slightly rich mixture (at Z_{St} and slightly higher), due to its highest chemical reactivity, can alter the ignition and combustion phasing. Figure 3.18b shows CH₂O mass fractions of SOI -80 and -40 CAD at 5 CAD ATDC as indicator for the second stage ignition of PRF70. It can be seen that due to availability of richer mixtures, higher CH₂O mass fraction resulted for SOI -40 CAD. This shortens the transition time from first to second stage ignition, which takes 17 engine crank angles. This is an important outcome of applying stratified air-fuel charges bringing an additional and effective controlling parameter which is not available in HCCI engines. On the other hand, for SOI -80 CAD a large number of grid cells, with mixture fractions at $Z \approx 0.03$, have higher CH₂O mass fractions than SOI -40 CAD. This is because a larger amount of fuel undergoes the second stage ignition in SOI -80 CAD. This

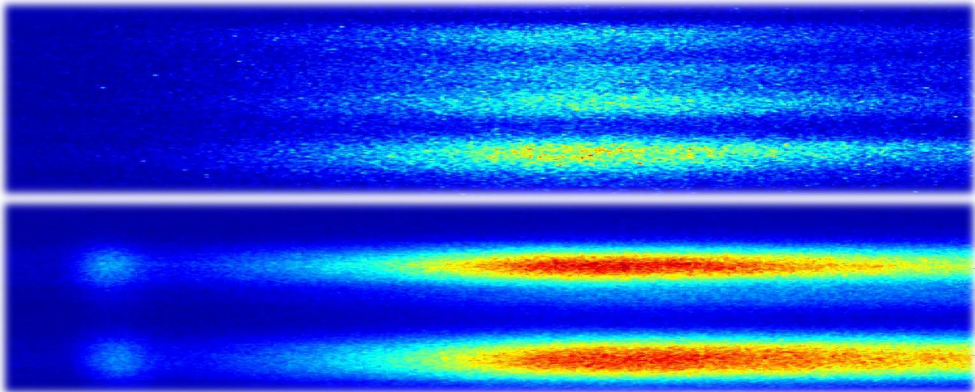
also causes a higher heat release rate peak in Fig. 3.18a for SOI -80 CAD.

3.5 Conclusions

The goal of this study was to investigate the ignition sensitivity of PPC combustion to the injection timing by using shadowgraphy and OH^* chemiluminescence imaging in a light duty optical engine. Quantified spray penetration measurements are performed for the first time in an optical engine by using side view shadowgraphy, to study how injection timing is affecting the mixture formation. Moreover, both radial and angular combustion stratification analysis is done for the first time based on OH^* chemiluminescence imaging. Combination of these results provided a good level of understanding about the combustion phasing and sensitivity of partially premixed combustion to the injection timing:

- Ignition sensitivity to injection timing is negative in two SOI regions from -100 to -12.5 CAD: firstly around SOI of -50 CAD where accumulated heat release is decreasing and secondly, around SOI of -30 CAD where accumulated heat release is rapidly increasing.
- Shadowgraphy experiments confirm that injection timing, targeting and spray penetration have significant influence on mixture formation and combustion phasing behavior. Negative ignition sensitivity values for SOI around -50 CAD is caused by the high amount of trapped fuel in the crevice volume while negative ignition sensitivity values of SOI around -30 CAD is caused by collision of piston and liquid core.
- Behaviors of angular and radial stratifications for different injection timings are exactly the same. Hence, either of them or their mean value can be taken as representative for combustion stratification.
- Combustion stratification is low and almost independent of SOI for early injections, while there is a remarkable reverse correlation between combustion phasing and stratification level for the late injections (-45 to -12.5 CAD). Indeed, the higher local equivalence ratios of late injections, followed by more stratified combustion, advance the combustion phasing.
- Combustion stratification can dramatically increase by collision of the liquid core with the piston, leading to advanced combustion.
- Injection pressure can adversely affect combustion stratification. However, the effect of injection pressure on the combustion stratification is insignificant compared to the effect of injection timing.
- CFD results confirm that high air-fuel stratification will cause a faster shift from first stage to second stage ignition of PRF70 fuel. This was argued to be due to higher reactivity of the mixture in high air-fuel stratification cases.

Spectral Signature and Stratification



This chapter is based on the following publication:

Izadi Najafabadi, M., Egelmeers, L., Somers, B., Deen, N., Johansson, B., Dam, N., (2017) **“The influence of charge stratification on the spectral signature of partially premixed combustion in a light-duty optical engine”**, *Applied Physics B: Lasers & Optics* 123:108, 2017, doi:10.1007/ s00340-017-6688-9.

4.1 Introduction

PPC allows to reduce both NO_x and soot emissions while providing high combustion efficiency. By and large, the low NO_x emissions result from the low combustion temperature, whereas the low soot emission is a result of increased premixing (with respect to conventional CI engines) [5, 20, 46–48]. However, many details of the in-cylinder phenomena are still to be explained and evaluated.

By coupling a high-speed camera to a spectrograph, crank angle- and cycle-resolved spectroscopic data, containing detailed information regarding the species formation during the combustion, can be obtained. Chemiluminescence and thermal radiation are expected to be the dominant sources of luminescence during combustion [49]. Depending on the combustion mode, the intensities of these two contributions will vary. Thermal radiation is mainly composed of black-body radiation coming from soot particles that are heated to flame temperature by the combustion process [50], while the term chemiluminescence is used for the light emission of specific molecules, which are formed in an electronically excited state during combustion and spontaneously decay back to lower energy levels [50, 51]. Chemiluminescence occurs in specific wavelength bands that are characteristic of the emitting molecules. The chemiluminescence yield due to specific molecules varies for different combustion regimes, and this can provide information about the nature of the chemistry involved [51–53]. Because chemiluminescence is the direct product of exothermic chemical reactions, it marks the location of the initial combustion reactions, both temporally and spatially [52], although reaction pathways leading to chemiluminescent species are under debate [54]. In practical implementation, a drawback is that the collected light is integrated along the line of sight of the detector. By any means, chemiluminescence imaging is a useful tool for time- and space-resolved investigation of the reactions that occur during combustion [55].

Molecular spectroscopy has also been used to study HCCI combustion in IC engines. Hultqvist et al. [51] obtained chemiluminescence spectra during the low temperature reactions and the main heat release period of HCCI combustion. They found that, depending on the fuel, low temperature reactions may or may not occur and precede the main heat release. During the main heat release, a continuous, essentially structureless spectrum ranging from 250 nm to 550 nm was observed. Furthermore, a strong correlation between the light intensity and the rate of heat release was found. Dec et al. [55] showed that the emission spectrum of combustion in conventional CI engines includes distinct features due to thermal radiation and OH^* chemiluminescence. Kim et al. [56] used spectroscopy to compare HCCI, SCCI and SI combustion of PRF50. They analyzed spectra based on putative point-measurements at the center of their combustion chamber. In the SI combustion spectra, an OH^* peak was observed during the combustion, while CH^* and C_2^* peaks were only present during the early stage of combustion. The main heat release spectra of HCCI combustion were dominated by the CO_2^* continuum with superposed formaldehyde bands, but peaks corresponding to OH^* , CH^* and C_2^* were not observed. They also reported broadband chemiluminescence during the low-temperature heat release, be it 3-4 orders of magnitude less intense than the luminescence during the main heat release. Augusta et al. [57] investigated the spectral features of HCCI combustion of PRF87 under a wide variety of engine operating conditions. They observed

several distinct, although weak, spectral peaks attributed to OH^* , CHO^* , CH^* , and CH_2O^* , superimposed on a CO_2^* continuum. Their results were similar for all operating conditions, suggesting that the primary reaction pathways of the fuel remained unchanged in spite of factors that significantly affected HCCI combustion timing and heat release rate.

Many studies have used optical filters to investigate the combustion behavior and detect different species like OH^* and CH^* [30, 49, 53, 58]. The obvious advantage of spectral bandpass filters is that they allow spatial distribution mapping; the obvious disadvantage is that one can never exclude spectral interference by other emitters than those for which the filter is intended. OH^* bandpass imaging is typically used as a measurement method for the rate of heat release in combustion. The equivalence ratio (in premixed laminar flames) is often estimated by means of the intensity ratio between OH^* and CH^* chemiluminescence. The CH^*/OH^* chemiluminescence ratio is found to proportionally increase with equivalence ratio at atmospheric pressures [59, 60].

In this chapter, optical emission studies of partially premixed combustion are reported. A method has been developed to distinguish between chemiluminescence by various species (OH^* , C_2^* and CH^*) and thermal radiation, based on spectroscopic measurements of the lion's share of the combustion chamber. The effect of charge stratification on the spectral signature of PPC combustion has been investigated for the first time, and is compared to homogeneous conditions. Furthermore, a study has been performed on the reliability of bandpass filters when they are used to investigate the auto-ignited combustion in an IC engine. As the final part of this research, broadband chemiluminescence and the CH^*/OH^* intensity ratio are investigated as a proxy for equivalence ratio of low-temperature combustion in an IC engine.

4.2 High-speed Spectroscopy Setup

Crank-angle resolved spectroscopic measurements are performed by coupling a high-speed intensified camera (Lambert HiCAM 5000) to a grating spectrograph (Acton SP-300i). Combustion luminescence is recorded through the quartz piston, via the 45° mirror (Fig. 4.1); under the operating conditions selected here, window fouling was found to be negligible. The field of view (FOV) of the spectrograph comprises a tangential section through the cylinder, so as to always focus on multiple combustion clouds (red line in Fig. 4.1). Specifications of the detection setup are presented in Table 4.1.

A mercury vapor lamp is used for calibration of the spectrograph. The spectrograph imaging system deforms the detected image. In Fig. 4.2a this pincushion distortion is illustrated for one of the mercury vapor emission lines. All images are corrected for pincushion distortion as depicted in Fig. 4.2b. Later the calibration is performed by relating the camera pixels to corresponding wavelength by means of the mercury spectrum as shown in Fig. 4.2c. This linear correlation is based on the first six peak positions.

Figure 4.1: Schematic of the spectroscopy setup. Combustion luminosity passes through the flat optical piston and is reflected by the stationary 45° tilted mirror. Then it passes through the entrance slit of the spectrograph and separates into a frequency spectrum which is recorded by the high-speed intensified camera. The spectrograph's field of view is shown by red color in top view.

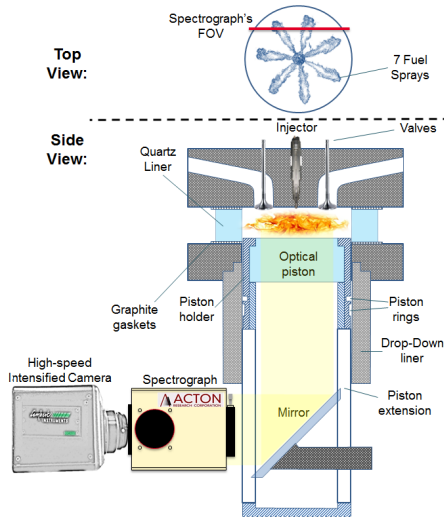
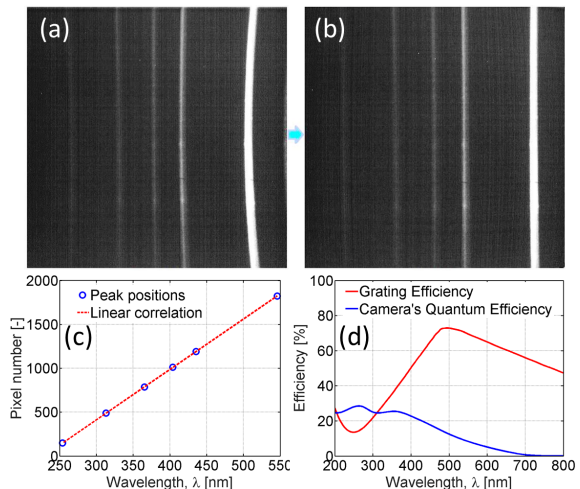


Table 4.1: Specifications of the camera and spectrograph.

Camera	Lambert HiCAM 5000 (built-in intensifier)
Imaging sensor	8 bit CMOS
Resolution	512 × 512 pixel ²
Frame rate	3600 fps
Exposure time	250 μs
Objective lens	UV Bernhard Halle Nachfl. 100 mm f/2
Spectrograph	Princeton Acton SP-300i
Groove frequency	150 l/mm
Blaze	500 nm
Wavelength range	270-540 nm
Linear dispersion	10.5 nm/mm

Figure 4.2: Calibration procedure of spectroscopy measurements. (a): Pin-cushion distortion of the mercury vapor lamp spectrum. (b): correction of the distorted image. (c): Calibration of spectrograph using the mercury vapor lamp spectrum. Camera pixels are linearly correlated to the corresponding wavelength. (d): Spectrograph grating efficiency and camera quantum efficiency curves which are combined to scale the spectra to constant detection efficiency.



The quantum efficiency of the intensified camera changes over the wavelength range as illustrated in Fig. 4.2d (based on the manufacturer data sheet). The grating efficiency of the spectrograph is also affecting the acquired spectra. The grating used in these experiments has a groove frequency of 150 l/mm and is blazed at 500 nm. In Fig. 4.2d, the grating efficiency curve is included as well. These data are combined to scale the spectra to constant detection efficiency. Since the transmission efficiency and collection angle of the other optics in the setup is constant over the whole wavelength range, no further correction was required.

4.2.1 Operating Conditions

For investigating different combustion modes, CA50 is held nearly constant by adjusting intake temperature for five different single-injection timings (different ignition delays) using direct injection at an injection pressure of 600 bar. The set of parameters for each injection timing are presented in Table 4.2; for all cases the amount of injected fuel is approximately 17 mg/cycle. For each measurements point, 30 firing cycles are recorded.

Table 4.2: Single injection strategies. Total injected fuel is approximately 17 mg/cycle in all cases.

Case	Injection timing [CAD]	Injection duration [CAD]	CA50 [CAD]	Intake temperature [K]	Oxygen percentage [Vol. %]	Air flow [g s^{-1}]	Global Equivalence ratio [-]
A	-200	5.6	8	323	19.0	6.8	0.40
B	-50	5.4	9	348	19.0	6.8	0.39
C	-25	5.4	9	348	18.8	6.7	0.40
D	-20	5.4	10	343	19.0	6.8	0.39
E	-15	5.5	10	413	18.8	6.5	0.41

The pressure and heat release rate curves for different injection timings (cases A-E of Table 4.2) are presented in Fig. 4.3. In case A, homogeneous combustion is achieved by injecting early, well before TDC. Cases C, D and E all represent partially premixed combustion with different injection timings and, therefore, different charge stratification levels, whereas case B can be classified as a transition point from HCCI to PPC. Case E, having the latest injection timing, causes the highest peak rate of heat release (ROHR) since higher local equivalence ratios (closer to stoichiometric) are formed for this case (see chapter 6).

To allow for investigation of equivalence ratios, the injection duration is slightly varied for injection strategies A and C. The corresponding sets of parameters are presented in Table 4.3. In order to maintain a constant airflow and a similar CA50, the intake pressure and temperature are slightly tuned. The global equivalence ratios for all experimental points are reported in Tables 4.2 and 4.3. However, for PPC operating points the local equivalence ratios are likely to be much different from the global ones. For that reason, the injected fuel mass has been used for labeling the results of PPC points in the next sections.

Figure 4.3: Time-resolved in-cylinder pressure for different charge stratification levels (Table 4.2). The inner graph shows the heat release rate as a function of crank angle degree for the same pressure traces. The time-resolved heat release rates are also shown in Fig. 6.9.

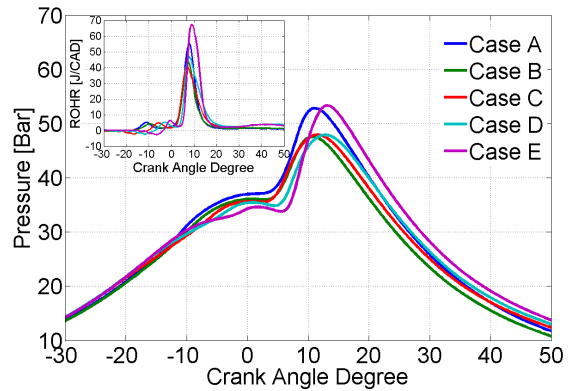


Table 4.3: Single injection strategies for varying equivalence ratio. Operating conditions correspond to Table 4.2

Case	Intake pressure [bar]	Intake temperature [K]	Injected fuel mass [mg/cycle]	Global Equivalence ratio [-]
A	1.18	303	19.70	0.44
	1.20	323	18.14	0.40
	1.21	348	16.58	0.36
	1.22	348	15.02	0.33
C	1.18	318	18.92	0.44
	1.20	348	16.97	0.40
	1.21	373	15.02	0.35
	1.22	398	13.07	0.31

4.3 Spectroscopy Analysis

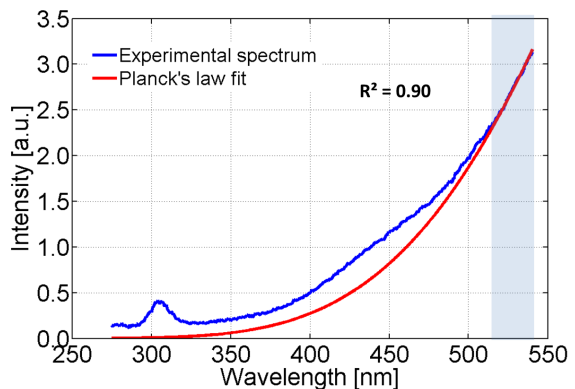
The spectroscopic measurements provide spectral and temporal information regarding the combustion [50, 51, 53]. The objective of these measurements is to analyze the chemiluminescence intensities of five different components, including thermal radiation, broadband chemiluminescence, and relatively narrow-band OH^* , CH^* and C_2^* emission, in the PPC combustion regime. To achieve this goal, the spectral signature over a wavelength range of 270-540 nm is recorded simultaneously. Spectra are integrated over the entire FOV, and corrected for detection efficiency, as explained above. The contribution of thermal (black body) radiation is estimated based on Planck's law. The remaining broadband luminescence is attributed to chemiluminescence of relatively large molecules, like HCO^* , H_2CO^* and CO_2^* . The contributions of OH^* , C_2^* and CH^* are determined based on their relatively narrowband emission in characteristic spectral ranges, as detailed below. Our desire to record a large spectral range simultaneously comes at the cost of a relatively low spectral resolution. Therefore, no attempt has been made to analyze spectral envelopes of the narrowband contributions.

Initially, the thermal radiation intensity was separated from the total spectrum. This has been done by evaluating the wavelength range of 500-540 nm and fitting Planck's law to the data. This wavelength range (500-540 nm) is less than desirable but the maximum that could be achieved given the spectrometer and the fact that the entire OH* band (on the other end of the spectral range) was to be acquired simultaneously. Here, Planck's law is described as

$$I(\lambda) = A \frac{2hc^2}{\lambda^5} \frac{1}{e^{\frac{hc}{\lambda k_b T}} - 1} \quad (4.1)$$

where c represents the speed of light [m s^{-1}], h and k_b represent the Planck constant [$\text{m}^2 \text{kg s}^{-1}$] and the Boltzmann constant [$\text{m}^2 \text{kg} / \text{s}^2 \text{K}$], respectively, λ is the wavelength [m], T represents the temperature [K] and A is a scaling factor. The unknown values for A and T are scaled such that Planck's law fits the data best, see Fig. 4.4 for an example. It should be noted that the good fit found in this particular figure is not representative for all cases. In the example of Fig. 4.5, broadband chemiluminescence dominates the spectrum, and the restricted wavelength range available for Eq. 4.1 does not allow to distinguish a separate contribution due to thermal radiation. The threshold criterion of 0.8 is used for the coefficient of determination (R^2) for the correlation between Planck's law and the experimental data. This threshold R^2 value is based on visual inspection of a large number of spectra. When the criterion is met ($R^2 > 0.8$), thermal radiation is considered to contribute perceptibly to the total spectrum. It is realized that the choice of the value of 0.8 is arbitrary, but ascertained that the results do not vary significantly for cut-off values in the range 0.7-0.9. The net contribution of the thermal radiation is then defined by integrating Planck's law over the full observed wavelength range. When the threshold criterion is not met, any contribution of the thermal radiation is included in the broadband chemiluminescence, discussed later in this section. In fitting Planck's law, temperature has been limited between 1000 and 2500 K. However, for $R^2 > 0.8$ the best-fit temperature is always between 2000 and 2400 K and it decreases towards the end of combustion.

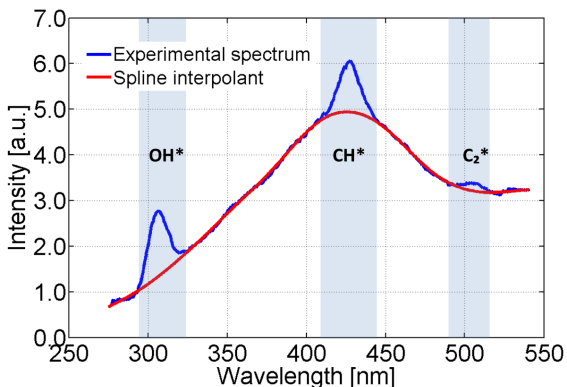
Figure 4.4: Planck's law fitted to the obtained spectrum in the wavelength range (shaded area) of 500-540 nm (case C, injected fuel mass: 16.97 mg/cycle, 23 CAD ATDC). The coefficient of determination (R^2) for this fitted curve is 0.9.



After subtraction of the thermal component (if present), in the remaining spectra a broadband signal is observed, stretching from approx. 300-500 nm. Literature relates this broadband spectrum to chemiluminescence of relatively large molecules like HCO*, CH₂O*, and CO₂* [61].

In order to separate the narrower OH^* , CH^* and C_2^* chemiluminescence from this broadband chemiluminescence, a smooth spline is fitted, based on the data in the wavelength ranges outside the well-defined OH^* , CH^* and C_2^* spectral ranges of 285-320 nm, 415-445 nm and 495-516 nm, respectively (indicated by shading in Fig. 4.5). Then, a spline interpolation is made in the shaded wavelength ranges. Again, this broadband chemiluminescence signal is subtracted from the total spectrum and integrated over the observed wavelength range to obtain a measure for this signal.

Figure 4.5: A smooth spline fitted to a typical observed spectrum (case C, injected fuel mass: 16.97 mg/cycle, 5 CAD ATDC). The spline fit is based on the data in the wavelength ranges outside the well-defined OH^* , CH^* and C_2^* spectral ranges of 285-320 nm, 415-445 nm and 495-516 nm, respectively (indicated by shading). This spline fit is representative of broadband chemiluminescence of relatively large molecules.



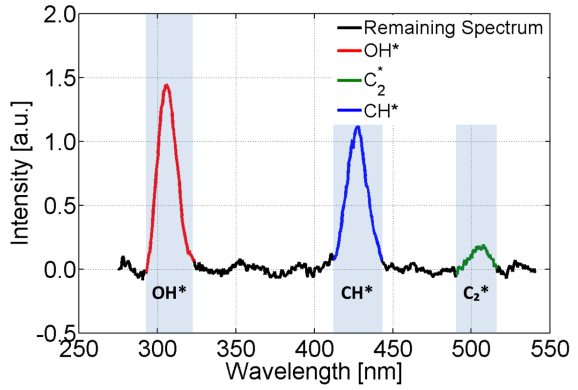
In Fig. 4.5 it is observed that the spectrum still might include some thermal radiation. However, in this particular experiment Planck's law does not correlate well to the data: $R^2 < 0.8$. This implies that in some measured spectra, especially within the early stage of combustion, the thermal radiation coincides with the broadband chemiluminescence signal and the measure for broadband chemiluminescence signal includes some thermal radiation. Evaluating a larger wavelength range (extended to the red) could overcome this problem, but this was not feasible with our available equipment.

An example of a remaining spectrum, after subtraction of both thermal and broadband chemiluminescence contributions, is displayed in Fig. 4.6. Due to finite spectrograph resolution and pressure broadening, species peaks are relatively broad. In order to define a measure for OH^* , CH^* and C_2^* chemiluminescence, the intensity is integrated from 285 to 320 nm, 415 to 445 nm and 495 to 516 nm, respectively.

4.4 Results and Discussion

Spectroscopy measurements have been performed for different combustion modes. All results presented in this section are based on mean data over 30 engine cycles in a single experiment. A high level of cycle-to-cycle repeatability is observed for the experimental points. First the effect of combustion stratification is investigated, followed by the assessment of the reliability of the bandpass filters and the relation to heat release rate. Finally, the effect of equivalence ratio has been investigated.

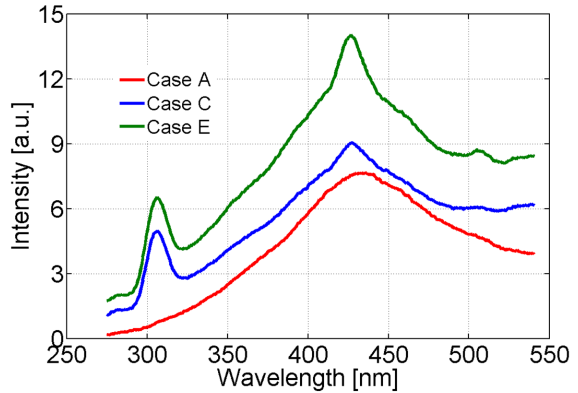
Figure 4.6: Remaining spectrum of Fig. 4.5 after subtraction of thermal radiation and broadband chemiluminescence (case C, injected fuel mass: 16.97 mg/cycle, 5 CAD ATDC). OH*, CH* and C₂* wavelength ranges are indicated (spectral ranges of 285-320 nm, 415-445 nm and 495-516 nm, respectively).



4.4.1 Effect of Combustion Stratification

Figure 4.7 displays the spectra for HCCI and PPC combustion at CA50. Clear differences can be noted; the PPC spectrum shows distinct features like OH*, CH* and C₂* chemiluminescence, whereas the HCCI spectrum only shows broadband chemiluminescence. As expected, HCCI combustion does not show thermal radiation at all. Also, there is almost no thermal radiation for the PPC points at CA50. However, thermal radiation is seen for PPC later in the combustion.

Figure 4.7: Spectra of HCCI (case A) and PPC (cases C and E) combustion at CA50. See Table 4.2 for operating conditions. The spectra of stratified cases (C and E) show distinct features of OH*, CH* and C₂* chemiluminescence, whereas the spectrum of the homogeneous case (A) only shows broadband chemiluminescence.



In order to highlight different aspects of the results, different normalization procedures are used. For Fig. 4.8, the time-integrated (cyclic) intensities attributed to individual sources are normalized by the total luminosity throughout the combustion cycle:

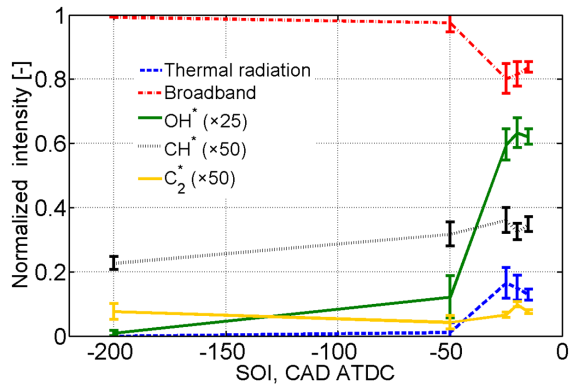
$$\bar{I}_{cl}(sp) = \frac{\int^{sp} d\lambda \int_{-180}^{+180} I_{sp}(\lambda, CA) dCA}{\int_{270}^{540} d\lambda \int_{-180}^{+180} I(\lambda, CA) dCA}, \quad \text{so} \quad \sum_{sp} \bar{I}_{cl}(sp) = 1 \quad (4.2)$$

where sp indicates signal over a wavelength range characteristic for a particular species, λ is wavelength [nm], CA is crank angle [CAD], $I(\lambda, CA)$ is the total recorded intensity as a function

of wavelength and time, $I_{sp}(\lambda, CA)$ is the contribution of either thermal radiation (Fig. 4.4), the spline interpolant for broadband chemiluminescence (Fig. 4.5), or the individual species intensity for OH^* , CH^* and C_2^* chemiluminescence (Fig. 4.6).

In Fig. 4.8, these normalized integrated intensities of different species ($\bar{I}_{cl}(sp)$) are presented as a function of SOI-timing, to illustrate the effect of charge stratification on combustion behavior. For OH^* , CH^* and C_2^* chemiluminescence, intensities are multiplied by factors of 25, 50 and 50, respectively, for sake of clarity. For homogeneous combustion points (early SOI, so long ignition delay) the predominant source of combustion luminosity is broadband chemiluminescence. Hardly any thermal radiation is detected and narrow-band chemiluminescence is all but absent as well. By moving from HCCI to PPC regime, the thermal contribution increases. Most likely, the latter is due to locally increased equivalence ratios (closer to stoichiometric) that give rise to enhanced formation of soot [5]. Furthermore, OH^* , CH^* and C_2^* chemiluminescence intensities all increase upon increasing charge stratification (as a consequence of moving from HCCI to PPC). This increase can be related to the influence of combustion temperature; locally higher equivalence ratios result in higher combustion temperature, this elevated temperature can be the cause of enhanced chemiluminescence. However, the exact chemical processes behind chemiluminescence are not sufficiently well known to provide definitive answers to the phenomena, particularly at elevated pressure [54, 62].

Figure 4.8: Cyclic normalized intensity based on Eq. (4.2) versus start of injection. Standard deviations over 30 measurement cycles are indicated. Intensities are multiplied for OH^* , CH^* and C_2^* chemiluminescence by factors of 25, 50 and 50, respectively, for the sake of clarity.



Time-resolved results for various species are presented in Fig. 4.9. In this figure, all curves are individually normalized such that their maximum values equal 1. This allows convenient comparison of peak timings of different luminosity sources. Figure 4.9a shows the results for HCCI combustion, while Fig. 4.9b illustrates the results for PPC. It is observed that HCCI combustion proceeds very fast, all luminosity sources observed culminate simultaneously. Furthermore, the luminosity behavior corresponds to that of the rate of heat release. Similar to Fig. 4.8, OH^* chemiluminescence and thermal radiation are not detected in this combustion mode. This spectral signature is similar to what Kim et al. [56] reported for HCCI combustion of PRF50. However, we did not see any spectral emission during the ignition delay and the low-temperature heat release, while Kim et al. reported a broadband emission with 3-4 orders of magnitude less intensity than the one during the main heat release. The absence of the spectral emission during the ignition delay of HCCI was also indicated by Augusta et al. [57], which is in agreement with our results.

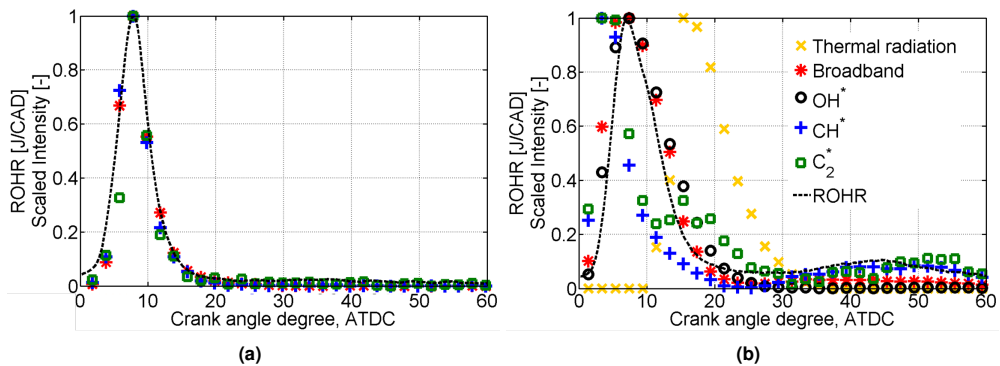


Figure 4.9: Crank angle-resolved behavior of different species for (a): HCCI combustion (case A) and (b): PPC combustion (case C), averaged over 30 cycles. Intensities of all species are scaled to 1. Note that OH* chemiluminescence and thermal radiation are not detected for HCCI combustion.

For PPC combustion, however, it is observed that C_2^* and CH^* chemiluminescence culminate first during the combustion. Subsequently, broadband and OH* chemiluminescence reach their peak simultaneously with the rate of heat release, whereas thermal radiation is typically dominant during the late phase of combustion, similar to conventional diffusion combustion. The early peak in C_2^* and CH^* chemiluminescence is likely due to the break-up of big molecules during the early stage of combustion, seen in highly turbulent premixed flames as well [63]. Around 45 CAD, a second, broader maximum is observed for all species, which is presumably caused by the burning of fuel escaping from crevice volumes as discussed in chapter 3. Still it correlates with the ROHR peak observed there as well. The high piston clearance in our optical engine (1 mm) is the main cause of a significant amount of trapped fuel, which would not be expected for a metal engine.

In Fig. A.1 in the Appendix A, the crank-angle-resolved results of different species for different injection timings are compared. By looking in more detail to Fig. 4.9b around 15 CAD, it can be seen that the C_2^* intensity increases a little bit where thermal radiation starts to be detectable. This behavior can also be seen for PPC points in Figs. A.1 and 4.12, especially for higher equivalence ratios: where thermal radiation of soot particles is maximum a second peak is seen for C_2^* . This is in agreement with results of Merola et al. [64] for the late stage of conventional diesel combustion. It can be concluded that there are two different chemical mechanisms for formation of C_2^* in the PPC regime; first during the early stage of combustion by the break-up of larger molecules and the second during the late stage of combustion when soot particles are forming.

4.4.2 Adequacy of Bandpass Filters

Since the observation is made that broadband chemiluminescence is dominant for both HCCI and PPC regimes, the question arises what is exactly investigated in studies that only apply optical bandpass filters to detect particular species in these combustion regimes [30,58]. This is

analyzed on the basis of the spectra for different levels of combustion stratification. Virtual OH^* , CH^* and C_2^* bandpass filters are applied to the recorded spectra to obtain integrated intensities in the wavelength regions of 285 to 320 nm (OH^*), 415 to 445 nm (CH^*) and 495 to 516 nm (C_2^*), see shading in Fig. 4.5. Also, the actual contribution of each species in its bandpass region is calculated by integrating the spectra after subtraction of all broadband contributions, see Fig. 4.5 and 4.6 for an example. The ratio of each species contribution to the total intensity in the corresponding filter region results in the percentage of that species at a given CA. The results are presented in Fig. 4.10.

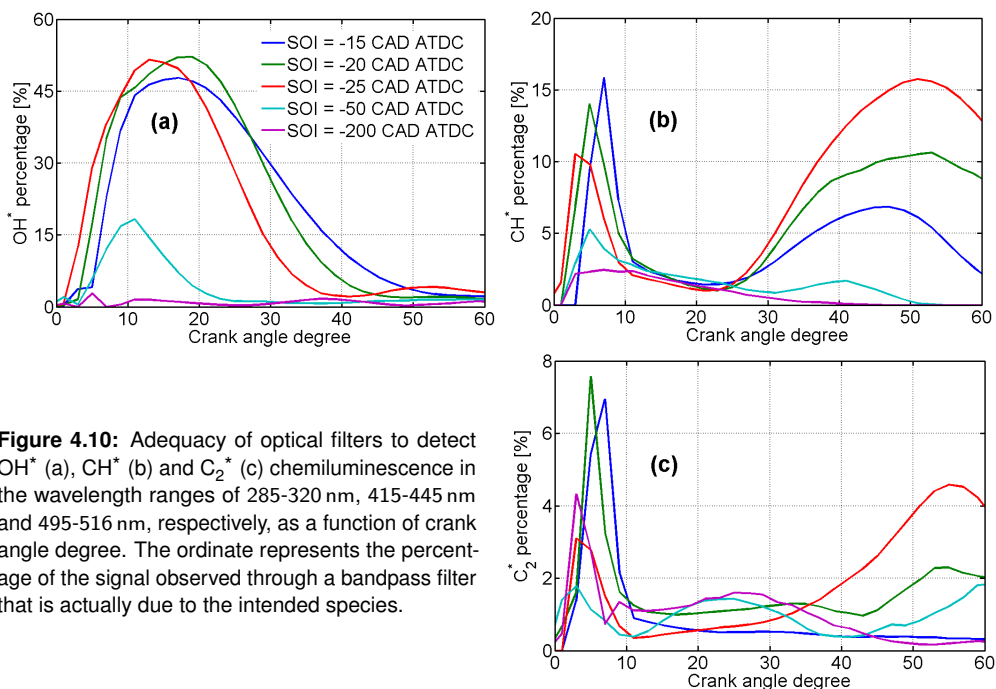


Figure 4.10: Adequacy of optical filters to detect OH^* (a), CH^* (b) and C_2^* (c) chemiluminescence in the wavelength ranges of 285–320 nm, 415–445 nm and 495–516 nm, respectively, as a function of crank angle degree. The ordinate represents the percentage of the signal observed through a bandpass filter that is actually due to the intended species.

It is observed from Fig. 4.10 that the adequacy of an optical filter to detect C_2^* and CH^* chemiluminescence is almost void for all combustion modes, due to the broadband chemiluminescence. For homogeneous condition cases (large ID), even the percentage of OH^* chemiluminescence is negligible. The increase in CH^* and C_2^* chemiluminescence percentage around 30–60 CAD ATDC is due to trapped fuel that escapes the crevices and burns as discussed in chapter 3. Concluding, even though the use of optical filters is indispensable for obtaining spatial information during combustion, the transmitted signal may largely be due to other chemical compounds than the one intended.

4.4.3 Chemiluminescence & Rate of Heat Release

In previous publications [30, 51, 58], OH^* chemiluminescence intensity measured through bandpass filters has been used as a proxy for the local rate of heat release. Since Fig. 4.10 illustrates that the percentage of actual OH^* signal observed through OH^* bandpass filters is often negligible, one may wonder whether the luminosity recorded through OH^* bandpass filters is still a measure for the heat release or not. To this end, the HCCI experiments with different equivalence ratios are analyzed (see Table 4.3, case A). Figure 4.11a shows the scaled accumulated intensity obtained through a virtual OH^* bandpass filter from CA10 to CA90 versus the scaled heat released in these experiments. The heat release period from CA10 to CA90 is chosen to focus only on the main heat release. Hence, the low temperature heat release, which is not accompanied by any emission, and the afterburning of trapped fuel, which is far from homogeneous, are not considered in Fig. 4.11. A linear relation is observed, with a high coefficient of determination. The residual scatter of data points is probably due not so much to low signal-to-noise ratios but rather to the relatively large time step between recorded images (compared to the heat release data) and the limited FOV of the spectrograph, which is merely a line whereas the heat release is volumetric. Still, these results indicate that the intensity observed through OH^* optical bandpass filters indeed can be used as a measure for the rate of heat release even though the signal is hardly a measure for OH^* at all. This analysis has been repeated for the total range of broadband chemiluminescence in Fig. 4.11b. A similar linear relation results, which shows that the broadband chemiluminescence can be taken as a measure for the heat release rate in this HCCI combustion mode. The same relation can already be seen in Fig. 4.9a, where the rate of heat release corresponds to the broadband chemiluminescence signal. This analysis is only done for HCCI combustion, because the limited FOV of the spectrograph in the stratified combustion mode (PPC) is not sufficiently representative to be used for comparison with the volumetric heat release.

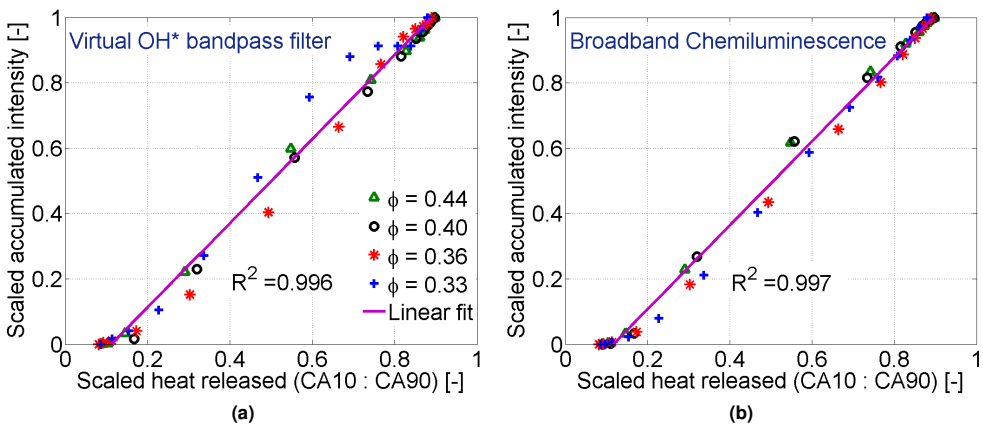


Figure 4.11: Relation between virtual OH^* bandpass filter intensity (a), broadband chemiluminescence (b) and the scaled heat released for several equivalence ratios in HCCI mode.

4.4.4 A Proxy for Equivalence Ratio

The effect of equivalence ratio on the spectral signature of combustion has been investigated for all operating conditions of Table 4.3. Figure 4.12 (next page) illustrates the wavelength-integrated signal intensities of different components. It is observed that increasing the injected fuel mass leads to an overall increase of luminescence, but otherwise nothing much happens. Regarding HCCI points, it is shown that the thermal radiation and OH^* chemiluminescence are absent for low equivalence ratios and significantly increase for the highest measured equivalence ratio ($\varphi = 0.43$). However, the signal intensity of OH^* chemiluminescence is still three orders of magnitude less than the broadband chemiluminescence in this point, supporting the low adequacy of using OH^* optical filters for detecting the OH^* signal, discussed in section 4.4.2, for PPC and HCCI operating conditions.

Finally, the average OH^*/CH^* chemiluminescence ratio is investigated for PPC conditions (case C). This analysis has been done for various amounts of injected fuel, and results are depicted as a function of CAD in Fig. 4.13a.

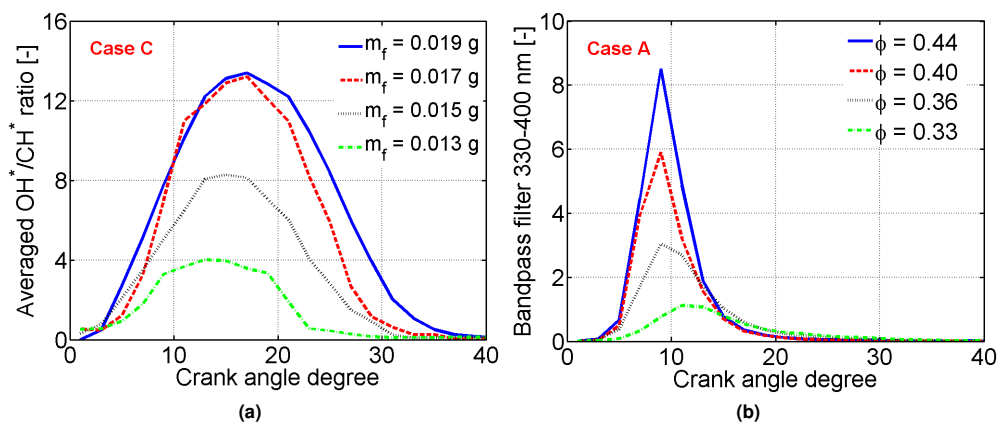


Figure 4.13: Average OH^*/CH^* ratio for different amounts of injected fuel of case C, (a) and 330-400 nm bandpass filter for different equivalence ratios of case A (b).

This figure shows that the average OH^*/CH^* chemiluminescence ratio increases with increasing equivalence ratio. An opposite relation is observed in premixed laminar flames [65]. This difference may be caused by the elevated in-cylinder pressure, turbulence, or flame stretch phenomena, as suggested by Nori et al. [65], who observed a monotonic decrease of the OH^*/CH^* intensity ratio upon increasing the equivalence ratio for atmospheric pressure methane combustion. For elevated pressures, however, they observed a monotonic increase of the OH^*/CH^* intensity ratio upon increasing the equivalence ratio. Furthermore, they concluded that the OH^*/CH^* ratio can be used for equivalence ratio sensing, but only at certain conditions. Since in-cylinder pressure varies dramatically over a stroke in an IC engine, it is impossible to consider the OH^*/CH^* ratio as representative of equivalence ratio. But there may be an

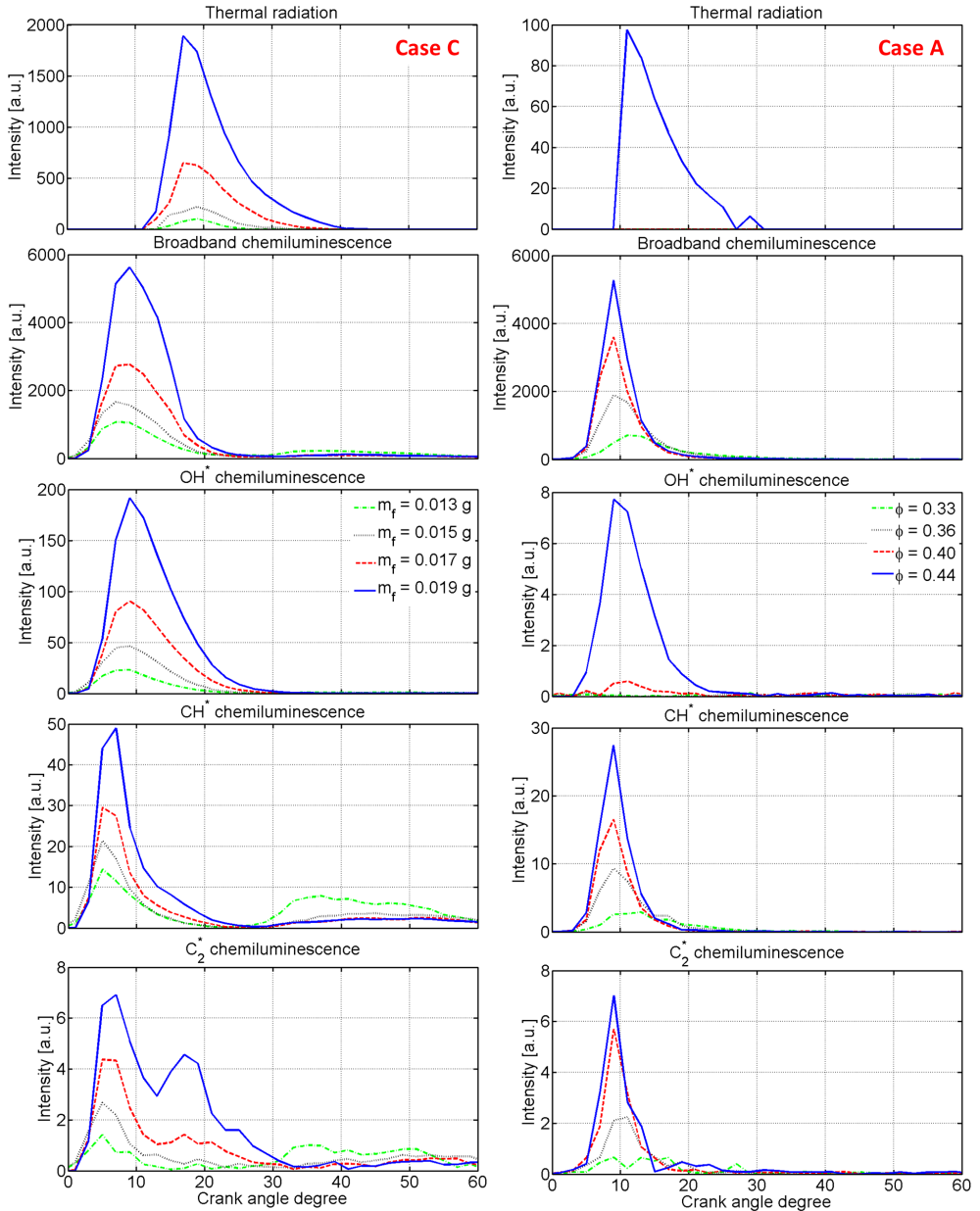


Figure 4.12: Time-resolved species chemiluminescence intensities for varying injected fuel mass. Left: SOI -25 CAD ATDC (case C). Right: SOI -200 CAD ATDC (case A). Species chemiluminescence intensities after 30 CAD are caused by the burning of fuel escaping from crevice volumes.

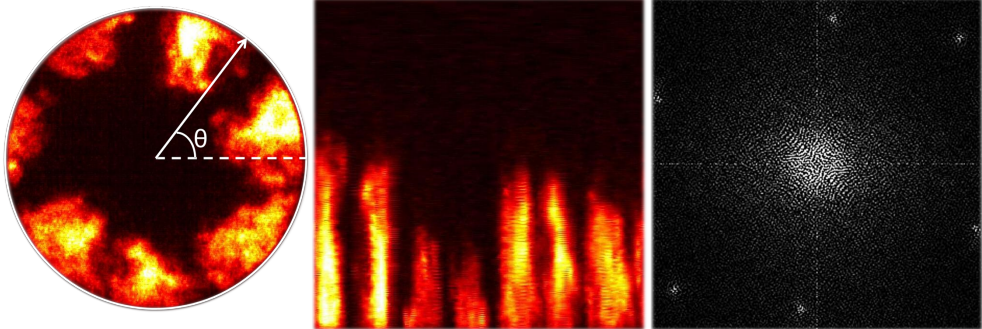
alternative. Figure 4.12 shows a strong correlation between equivalence ratio and broadband chemiluminescence intensity for both HCCI and PPC cases. We suggest using bandpass filters in the range of 330-400 nm to collect pure broadband chemiluminescence as a proxy of local equivalence ratio during combustion as shown in Fig. 4.13b. Note that this method demands precise calibration and further investigations.

4.5 Conclusions

The objective of this study was to evaluate the spectral signature of Partially Premixed Combustion at different stratification levels. Spectroscopic measurements were performed in order to analyze the sources of combustion luminosity in a light-duty optical engine. A method has been described to distinguish between different sources of light. Based on this analysis the following is concluded:

- Broadband chemiluminescence, a collective name for CO_2^* , HCO^* and CH_2O^* chemiluminescence, dominates the spectrum for HCCI combustion. With increasing stratification, narrowband OH^* , CH^* and C_2^* chemiluminescence intensities increase.
- Whether the in-cylinder combustion can be analyzed by means of optical filters is questionable, since a significant broadband chemiluminescence signal is transmitted for both PPC and HCCI regimes.
- Broadband chemiluminescence can be used as a measure for the heat release rate. This implies that, as broadband emission and OH^* chemiluminescence correlate strongly with local rate of heat release, an OH^* bandpass filter can still be used since its signal will be proportional to the rate of heat release anyway. However, further fundamental investigation and validation is required when different combustion parameters are used.
- Results show that there are two different chemical mechanisms for formation of C_2^* in PPC regime; first during the early stage of combustion, most probably due to the break-up of larger molecules, and the second during the late stage of combustion, when soot particles are forming.
- In atmospheric premixed laminar flames the OH^*/CH^* ratio monotonically decreases with equivalence ratio. However, at elevated pressures an inverse relation is observed [65]. This implies that the OH^*/CH^* ratio can be used for equivalence ratio sensing, but only at certain pressures and temperatures. Thus, it is impossible to apply these relations in an IC engine with varying pressure. However, the broadband chemiluminescence, particularly in the range of 330-400 nm, may be an alternative, because its intensity does correlate with equivalence ratio quite well in both HCCI and PPC regimes.

Fourier-based Stratification Analysis



This chapter is based on the following publications:

Izadi Najafabadi, M., Somers, B., Johansson, B., Dam, N., (2017) “**Combustion Stratification Study of Partially Premixed Combustion by Using Fourier Transform Analysis of OH* Chemiluminescence Images**”, *International Journal of Engine Research*, in Press, doi:10.1177/1468087417740270.

Izadi Najafabadi, M., Dam, N., Somers, B., Johansson, B., (2016) “**Fuel and Combustion Stratification Study of Partially Premixed Combustion**”, *ECCO-MATE Conference I: Combustion Processes in Marine and Automotive Engines*, Lund, June 2016.

5.1 Introduction

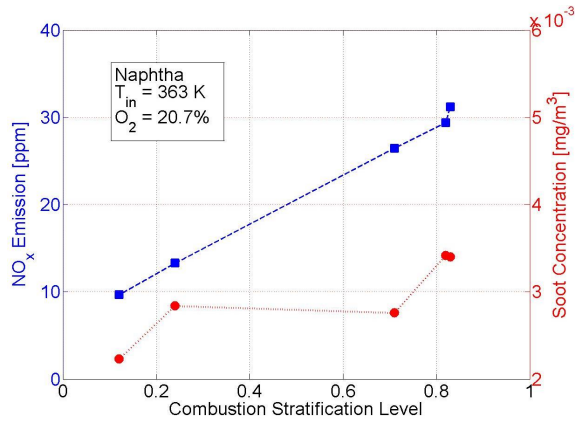
Partially premixed combustion (PPC) relies on an optimal ignition delay to achieve a partially premixed charge [5, 19, 20, 46–48]. Control of premixing is necessary to implement PPC combustion strategies particularly in transient mode and to improve the emission formation over the full load range [21, 47, 48]. The amount of premixing can be controlled in various ways, for instance by tuning the injection timing.

Combustion stratification (as a result of mixture stratification and/or thermal stratification) can qualitatively be considered as the lack of combustion homogeneity. For the PPC combustion concept, stratification is one of the main parameters affecting the combustion efficiency, and it improves the controllability of combustion in comparison with fully homogeneous (HCCI) combustion [48,66]. For this reason, various studies have tried to define a metric for combustion stratification and to correlate it to engine performance [58, 67, 68], as also discussed in chapter 3. However, there is no objectively quantifiable definition for 'stratification level' thus far.

OH* chemiluminescence imaging is an optical combustion diagnostic based on recording photons emitted by naturally excited OH* radicals when they return to the ground state. In practice, these so-called OH* bandpass images are recorded by an intensified CCD or CMOS camera through a spectral filter that nominally transmits light only in the wavelength interval that is characteristic for OH* luminescence, say 305-315 nm. OH* chemiluminescence imaging offers line-of-sight information across the volume imaged, and its time-dependent intensity is known as an indicator for the temporal behavior of heat release rate [29–32]. This feature is commonly used in literature. Zegers et al. investigated the position and size of PPC combustion clouds by analyzing OH* chemiluminescence images in a heavy-duty optical engine [31]. A clear correlation between ignition delay and flame location was observed. Tanov et al. analyzed the combustion stratification of different injection strategies in a light-duty optical engine [30]. The degree of stratification was determined as the ratio between the magnitude of intensity variations over the mean intensity of OH* bandpass images. Their results showed that the combustion following triple injection is more homogeneous compared to single or double injection. However, optical distortion by the piston bowl limited their study to only angular stratification analysis of PPC combustion in a narrow annular band inside the piston bowl. In the previous study [58] (see chapter 3), OH* bandpass imaging of PPC combustion was performed using a flat optical piston without any distortion. Therefore, the combustion stratification analysis used by Tanov et. al [30] could be improved and expanded to both angular and radial stratification over a wide field of view. The results presented in chapter 3 confirmed that the combustion stratification indeed is an important parameter, affecting the combustion efficiency and phasing. However, the results of the stratification definition used there (see sections 3.3.2 and 3.4.3) were significantly affected by noise, and it was hard to compare the stratification level of different PPC points objectively. Recently, the angular stratification method was applied by Vallinayagam et al. to study the combustion stratification for Naphtha ranging from CI combustion to PPC [37]. Their results showed a strong correlation between combustion stratification and NO_x/soot emissions as shown in Fig. 5.1.

All in all, the literature study confirms that stratification is playing a key role in controlling emis-

Figure 5.1: NO_x emission and Soot concentration as a function of combustion stratification for naphtha fuel (combined Figs. 15b and 17b of Ref. [37]). Measurements were performed in an optical engine with compression ratio of 9.5, driven at 1200 rpm with intake temperature of 363 K and intake oxygen percentage of 20.7 Vol. % in.



sions, ignition timing and heat release rate behavior of PPC. Hence, a robust and unambiguous quantification of this parameter would help to better understand PPC and can provide a tool to compare different studies.

This study improves and expands the combustion stratification study presented in chapter 3 by side view OH* bandpass imaging and analyzing the vertical stratification as well. Furthermore, an advanced stratification metric based on the spatial frequency domain and signal energy of OH* chemiluminescence images is proposed in this chapter. The new method can distinguish stratification levels where the old methods fail.

5.2 OH* Bandpass Imaging

OH* bandpass images are recorded at 1 CAD intervals by using a high-speed intensified camera. The flat optical piston used in this study provides optical access to the central 60 mm out of the 81 mm-diameter engine bore. The combustion is detected from below, by aiming the camera at the 45° mirror and from the side by aiming the camera directly at the quartz liner (Fig. 5.2). Bottom and side view imaging are not performed simultaneously. However, the same operating conditions are used for both.

Specifications of the detection setup are presented in Table 5.1. The light is recorded through a combination of a 315 nm bandpass filter with 20.4 nm FWHM and a 300 nm bandpass filter with 87.5 nm FWHM, to reject light with wavelength below 300 nm or above 330 nm. Transmissibility and optical density of the optical filters as well as their combination are depicted in Fig. 5.3. These filters are chosen to record OH* chemiluminescence wavelengths, which has peak emission around 310 nm, but it must be kept in mind that their transmission beyond the selected range is still finite.

Figure 5.2: Schematic of the side and bottom OH* bandpass imaging setups. For side view imaging, combustion luminosity passes through the quartz liner, is filtered by OH* bandpass filters and recorded by the high-speed intensified camera. For bottom view imaging, combustion luminosity passes through the flat optical piston, is reflected by the stationary 45° tilted mirror, filtered by OH* bandpass filters and in the end, recorded by the high-speed intensified camera. Note that side and bottom view imaging measurements were not performed simultaneously.

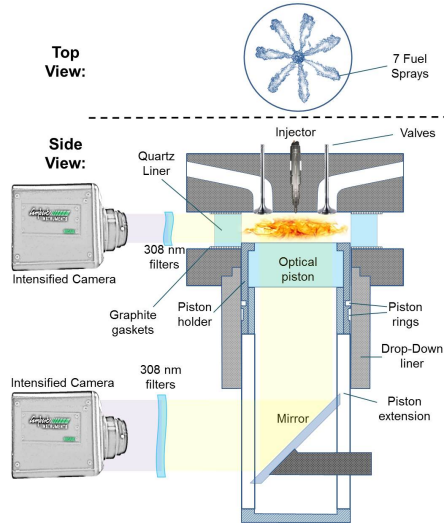


Table 5.1: Specifications of camera and optics. Bottom/side views refer to Fig. 5.2.

Camera	Lambert HiCAM 5000 (built-in intensifier)
Imaging sensor	8 bit CMOS
Intensifier	P46 with 0.2-0.4 μ s Phosphor decay time
Intensifier gain (bottom)	72 %
Intensifier gain (side)	58 %
Resolution (bottom)	352 \times 352 pixel ²
Field of view (bottom)	65 \times 65 mm ²
Resolution (side)	256 \times 512 pixel ²
Field of view (side)	45 \times 90 mm ²
Frame rate	7200 fps
Exposure time	25 μ s
Objective lens	UV Bernhard Halle Nachfl. 100 mm f/2

5.2.1 Operating Conditions

To investigate the effect of stratification, the CA50 is held constant at 8 CAD (by tuning the intake temperature) for four different single-injection timings (different ignition delays). These timings are detailed in Table 5.2; the amount of injected fuel is approximately 16 mg/cycle for all cases. In case A', port fuel injection is used as a reference point for the most homogeneous mixture and combustion. Stratification at other points can be evaluated with respect to this point. Due to the skip fire mode, the total amount of port-injected fuel does not end up in the fire cycle. Hence, for this case the amount of delivered fuel to the combustion chamber is tuned based on the accumulated heat release.

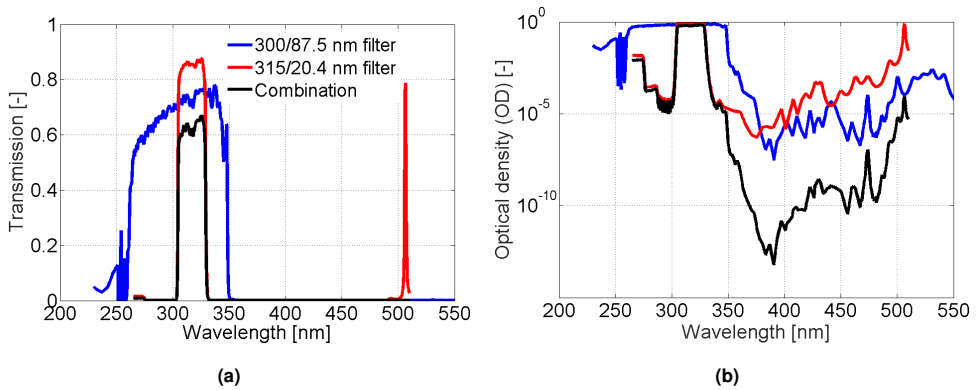


Figure 5.3: Transmittance (top) and optical density (bottom) of the optical filters used for OH^* bandpass imaging as well as their combination. The 315 nm bandpass filter with 20.4 nm FWHM is transmitting light in a narrow wavelength range around 500 nm. Hence, a 300 nm bandpass filter with 87.5 nm FWHM is added to reject light around 500 nm.

Table 5.2: Single injection timings. The total injected fuel mass is approximately 16 mg/cycle for all cases.

Case	Injection type	Injection timing [CAD]	Injection pressure [bar]	Injection duration [ms]	CA50 [CAD]	Intake temperature [K]	O_2 [Vol. %]	IMEP (net) [bar]
A'	Port	-340	4	3.30	8	348	18.2	3.6
B'	Direct	-100	600	0.740	8	348	18.3	4.2
C'	Direct	-25	600	0.725	8	368	18.4	4.3
D'	Direct	-15	600	0.720	8	393	18.4	4.6

5.3 Combustion Stratification Analysis

Time-resolved OH^* chemiluminescence imaging provides spatial and temporal information on the heat release rate during the combustion [29–32, 58]. The spectroscopy study for similar operating conditions, presented in chapter 4, showed that OH^* bandpass imaging is highly affected by broadband chemiluminescence of relatively large molecules, like HCO^* , CH_2O^* and CO_2^* , especially for HCCI points. However, it is observed that broadband chemiluminescence can be used as a measure for the heat release rate as well. This implies that an OH^* bandpass filter can still result in meaningful luminescence images, since the temporal behavior of the signal will be proportional to that of the heat release rate anyway [69].

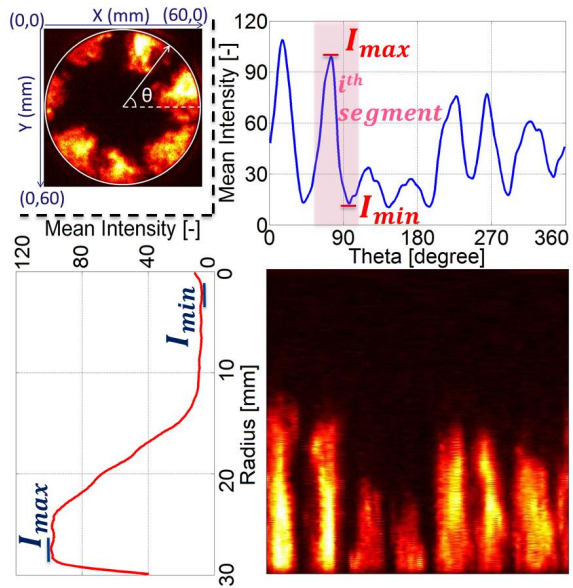
The goal of the image processing is to quantify the level of combustion stratification based on OH^* bandpass images. In this section, two methods are described to quantify the stratification. One method is based on previous works [30, 58], as also discussed in chapter 3, and the second is a newly proposed method based on the spatial frequency content of the chemiluminescence images. As before, the analysis is based on average recordings over 30 combustion cycles.

5.3.1 Angular, Radial and Vertical Stratification

As discussed in chapter 3 and in section 5.1, attempts to quantify the combustion stratification have been made previously [30, 58]. In this section, the angular, radial and vertical stratification analysis is based on the method discussed in section 3.3.2. Before data is analyzed, a background correction is carried out. The mean of 10 frames before the start of combustion is used as a background to be subtracted from all frames in a cycle. Imaging from beneath is analyzed in a polar coordinate system because of rotational symmetry of the spray configuration. For computational convenience, the recorded images (with a nominal center of symmetry at the nozzle position) are transformed into a Cartesian image with polar coordinates along the axes, based on linear interpolation (This will be referred as a direct space image; see Fig. 5.4).

To determine the angular stratification, the intensity is radially averaged and the average is plotted as a function of polar angle θ . The top right of Fig. 5.4 shows typical behavior of a PPC combustion by applying this method to an instantaneous OH^* bandpass frame. Based on that, the range of θ can be divided into 7 equal segments, representative of 7 combustion clouds (7 injector holes).

Figure 5.4: Typical behavior of intensity as a function of polar angle and radius for PPC combustion. Top left: original OH^* bandpass image at a certain CAD, top right: radially averaged intensity as a function of angle; the shaded region corresponds to one of the seven combustion clouds, bottom left: angularly averaged intensity as a function of radius, bottom right: image transformed into a Cartesian image with polar coordinates along the axes (direct space image). The graphs are derived from the bottom right image.



Referring to Fig. 5.4, the angular stratification of each image is defined in Eq. (3.2),

$$(Str_{\theta} = \frac{1}{n} \sum_{i=1}^n \frac{(I_{max} - I_{min})_i}{(I_{max} + I_{min})_i}).$$

To analyze radial stratification, for each radius (r), the intensity is averaged over all angles (θ). A typical example is illustrated in the bottom left part of Fig. 5.4. The radial stratification for each individual image is defined in Eq. (3.3),

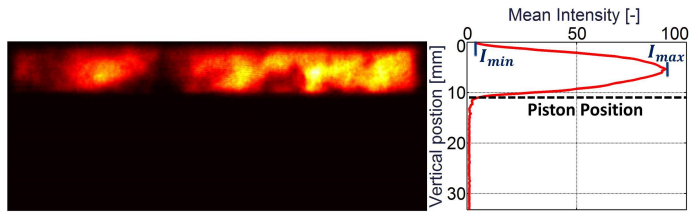
$$(Str_r = \frac{(I_{max} - I_{min})_{[0;R]}}{(I_{max} + I_{min})_{[0;R]}}).$$

To analyze the vertical stratification from the side view images, the intensity is averaged over the horizontal position and is plotted as a function of vertical position for individual crank angle degrees (Fig. 5.5). First the area of analysis is defined based on the piston position. Referring to Fig. 5.5, the vertical stratification, Str_z , of each image is calculated according to:

$$Str_z = \frac{(I_{max} - I_{min})_{[0:pp]}}{(I_{max} + I_{min})_{[0:pp]}} \quad (5.1)$$

where pp is the piston position relative to the cylinder head, and I_{max} (I_{min}) is the maximum (minimum) horizontally averaged intensity over the area of analysis.

Figure 5.5: Typical behavior of the horizontally averaged intensity as a function of vertical position for the side view images.



5.3.2 Fourier-based Stratification

The intensity-based analysis method, described in the previous section, is highly sensitive to noise by considering local intensities, and its outcome is not always informative, as will be discussed in section 5.3.3. To overcome the deficiencies of this method, a Fourier analysis-based stratification definition, that is explicitly considering combustion structure, is proposed and explained in this section.

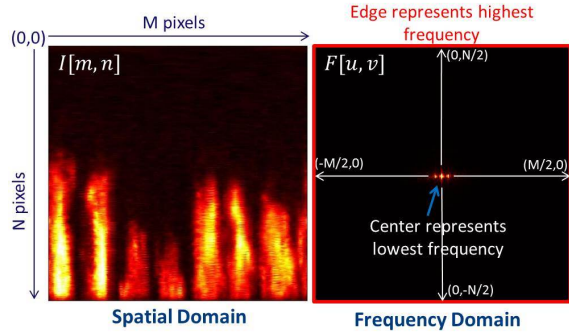
The Fourier-based method basically focusses on the spatial frequencies in a certain FOV. For ease of calculation, the recorded images (bottom view only) are again transformed into $M \times N$ direct space images, as above. In these images, the horizontal axis corresponds to polar angle, the vertical axis to radius. Over this 2D spatial domain, the discrete Fourier transform is applied based on Eq. (5.2) (see also Fig. 5.6):

$$F[u, v] = \sum_{m=0}^{M-1} \sum_{n=0}^{N-1} I[m, n] \cdot e^{-i2\pi(\frac{um}{M} + \frac{vn}{N})} \quad (5.2)$$

where $I[m, n]$ represents the intensity of pixel $[m, n]$ in direct space, and $F[u, v]$ represents the contribution of spatial frequency pixel $[u, v]$, in which u and v represent angular and radial frequency components, respectively. Note that the origin $[0, 0]$ in the direct space image is the top left corner, that in the Fourier space image is located in the center.

In direct space, the sampling unit is one pixel, corresponding to $\frac{2\pi}{M}$ [rad] (horizontal) or $\frac{R}{N}$ [m] (vertical), so the spatial frequencies in Fourier space are limited to the intervals $\pm \frac{M}{2}$ rad^{-1}

Figure 5.6: Transformation from the spatial domain to the frequency domain. In the frequency domain, the center represents the lowest frequency, while the edges represent the highest frequencies.



and $\pm\pi\frac{N}{R}$ (units of m^{-1}), respectively. Because the sampling in direct space is discrete, the sampling in Fourier space is discrete as well, with spatial frequency units corresponding to $2\pi/(\text{full range})$, where the full range corresponds to 2π rad (horizontal) and the bowl radius of 0.03 m (vertical), respectively. Note that the center of the frequency domain represents the lowest frequency (DC value), while the edges represent the highest frequencies [70].

Not all spatial frequencies in the Fourier domain are related to combustion stratification. Low spatial frequencies correspond to large scale variations, whereas the high spatial frequencies are largely due to noise. Hence, an intermediate spatial frequency range, A , should be selected, the signal energy of which (E_A) should be used to characterize the combustion stratification. This E_A should be properly normalized by the maximum possible signal energy. Thus, the normalized stratification will be independent of the camera, and allow to compare the combustion stratification obtained from different cameras and imaging methods (or any image format, as a result of numerical methods). Whereas the informative signal energy E_A is calculated from the Fourier space image, the maximum signal energy used for normalization can be calculated from the direct space image. Parseval's theorem can be used to relate the signal energy, E , of an image in the spatial and frequency domains [70]:

$$E = \frac{1}{MN} \sum_{u=-M/2}^{M/2} \sum_{v=-N/2}^{N/2} |F[u, v]|^2 = \sum_{m=0}^{M-1} \sum_{n=0}^{N-1} |I[m, n]|^2 \quad (5.3)$$

Writing

$$I[m, n] = k_{m,n} \times I_{max} \quad 0 \leq k_{m,n} \leq 1, \quad (5.4)$$

and using that the mean intensity of an image follows from

$$I_{mean} = \frac{1}{MN} \sum_{m=0}^{M-1} \sum_{n=0}^{N-1} I[m, n] \quad (5.5)$$

Parseval's equation can be rewritten as

$$\begin{aligned}
 E &= \sum_{u=-M/2}^{M/2} \sum_{v=-N/2}^{N/2} |I[m, n]|^2 = I_{max}^2 \sum_{m=0}^{M-1} \sum_{n=0}^{N-1} k_{m,n}^2 \\
 &\leq I_{max}^2 \sum_{m=0}^{M-1} \sum_{n=0}^{N-1} k_{m,n} = I_{max}(MN \times I_{mean}) \stackrel{\text{def}}{=} E_{max}
 \end{aligned} \tag{5.6}$$

in which the inequality could be introduced because $k_{m,n}^2 \leq k_{m,n}$. Equation (5.6) shows that the signal energy is always smaller than or at most equal to a particular maximum value, here denoted as E_{max} . This E_{max} can be objectively calculated from the direct space image, and is related to the mean intensity of this image. Note that I_{max} is the maximum pixel count for all combustion cycles and frames. The redistribution of pixel values inherent in the Cartesian-to-Polar transformation serves to suppress the effect of noise on I_{max} . The normalized Fourier-based stratification, Str_F , is now defined as

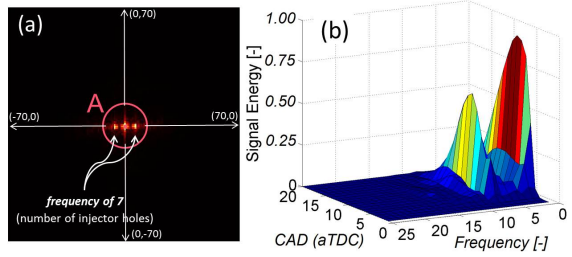
$$Str_F = \frac{E_A}{E_{max}} \tag{5.7}$$

Finally, the range A , containing the informative spatial frequency components, remains to be determined. A is a central portion of the Fourier plane, covering the frequencies physically relevant for stratification. In principle, it can have arbitrary shape, as long as it excludes the higher, noise-related frequencies. It is here chosen to be circular, as in Fig. 5.7a, but it will be shown later that this is not very critical. The relevant signal energy based on this spatial frequency range is calculated by

$$E_A = \frac{1}{MN} \sum_{(u,v) \in A} |F[u, v]|^2 \tag{5.8}$$

To specify the radius of spatial frequency range A , the images are divided in concentric rings around the origin, each one pixel wide. The signal energy is then calculated over each ring of radius k (similar to Eq. (5.8)) and the results are plotted as a function of k (spatial frequency). This is done for different crank angle degrees of the PPC combustion event illustrated in Fig. 5.10 (case C'). The result is shown in Fig. 5.7b. Two peaks are observed. The first peak, at $k = 1$, corresponds to the radial structure of the burning sprays, each filling about one quarter of the cylinder diameter, and the second peak, at $k = 7$, corresponds to the angular periodicity of the 7 sprays. On this basis, E_A is evaluated for the spatial frequency range of $1 \leq k_A \leq 2n$, where n represents the number of injector holes (see section 5.4.3 for more discussion). Based on this spatial frequency range, all critical spatial frequencies of a stratified combustion are covered in the stratification definition, while the effect of noise is minimized by not considering high spatial frequencies.

Figure 5.7: Typical spatial frequency domain for a PPC combustion image at a given crank angle degree (a), and signal energy as a function of radius k_A of the circular area A indicated in Fig. 5.7a (spatial frequency) for a sequence of crank angle degrees (b).



5.3.3 Validation

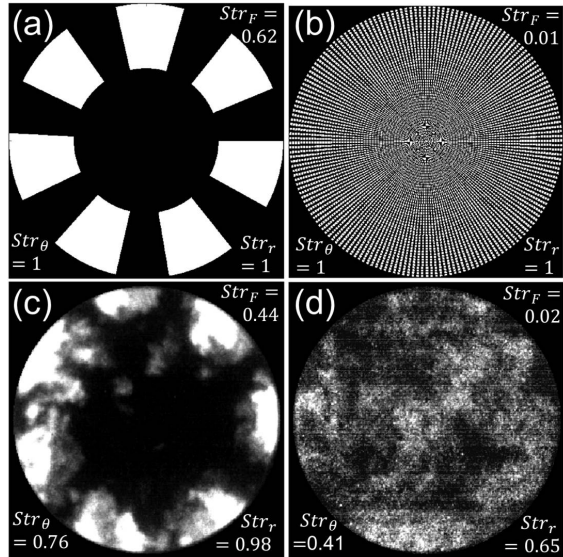
Two sample images, shown in Fig. 5.8a and 5.8b, are constructed to check the functionality of the Fourier-based method described in the previous section. Both images are composed of the same number of black (0) and white (1) pixels. As a result, both images have the same mean intensity and the same RMS fluctuation (the square root of mean square of pixel intensity fluctuations relative to the mean intensity). Their structure, however, is obviously very different. Figure 5.8a is a cartoon of typical PPC behavior (based on a 7-hole injector) like case D' as shown in Fig. 5.8c, while Fig. 5.8b represents an essentially homogeneous distribution, similar to typical HCCI behavior like case A', as illustrated in Fig. 5.8d. Both intensity-based stratification analysis (angular and radial stratification) and Fourier-based stratification analysis are implemented to extract the level of stratification from these images (actual values are added to the Fig. 5.8). The intensity-based method simply fails to distinguish between these two sample cases (a & b). Since there are radially-averaged and angularly-averaged intensities of 0 in both images, angular and radial stratifications equal 1 for both images (see Eqs. (3.2) and (3.3)). However, Fourier-based stratification clearly distinguishes the stratification levels of these two sample images, showing a stratification level of 0.62 for the stratified image (a) against a stratification level of 0.009 for the homogeneous image (b). For real OH^* bandpass images of case A' and D', it can also be seen that Fourier-based stratification can better distinguish between these two cases. From a physical point of view, this is fully understandable. RMS- and contrast-based methods do not specifically look at structure, but summarize integrated fluctuations. Fourier analysis, on the other hand, identifies spatial structure on various scales. For stratification analysis, which is all about structure, the latter is obviously the method of choice.

5.4 Results and Discussion

OH^* bandpass imaging has been performed for both bottom and side view. All the presented results in this section are the mean values over 30 measurement cycles, but error bars are omitted from intermediate results for the sake of clarity. However, a high level of repeatability is observed for the experimental points as can be seen in final results (Fig. 5.13).

Figure 5.9a shows the temporal heat release rate behavior for different injection timings (cases A'-D' of Table 5.2). As can be seen in this figure, the peak heat release rate does not correlate

Figure 5.8: Sample images: stratified (a), based on 7 angularly symmetric clouds, and homogeneous (b) distributions of pixel values of 0 and 1. Both images are composed of the same number of black (0) and white (1) pixels. OH* bandpass images: case D' at CA50 (c) and case A' at CA50 (d). Angular, radial and Fourier stratification levels are added to each image for comparison.



in a unique way to the injection timing. Case A' with SOI at -340 CAD can be classified as an HCCI point. Cases C' and D' represent PPC points with different charge stratification levels (injection timings at -25 and -15 CAD, respectively), whereas case B' with SOI at -100 CAD can be considered as a transition point from HCCI to PPC.

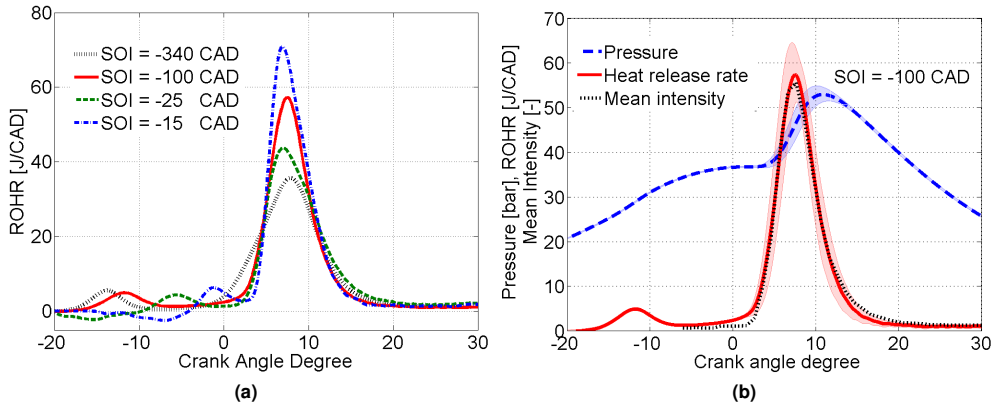


Figure 5.9: Rate of heat release (ROHR) for different injection timings (a) and comparison of pressure, ROHR and normalized mean intensity for SOI of -100 CAD (b).

In Fig. 5.9b, the normalized mean intensity and the heat release rate are compared for the injection timing of -100 CAD (case B' of Table 5.2). The very similar behavior of the heat release rate and the mean intensity shows the accuracy of OH* bandpass imaging as an indicator of heat release. However, for late injections (PPC points), a longer tail is observed

for the mean intensity in comparison with the heat release rate, which is probably due to soot luminosity transmitted through the optical filters. The combination of optical filters used in this study is relatively transmittive in the region around 500 nm (the optical density increases from 10^{-15} to 10^{-5} in this wavelength region; see Figure 5.3).

OH^* bandpass images around CA50 are demonstrated in Fig. 5.10 for different operating conditions. Based on inspection by eye, it can be seen that port fuel injection (case A') results in the most homogeneous combustion, while by retarding the injection timing toward -15 CAD ATDC (case D') the combustion stratification increases.

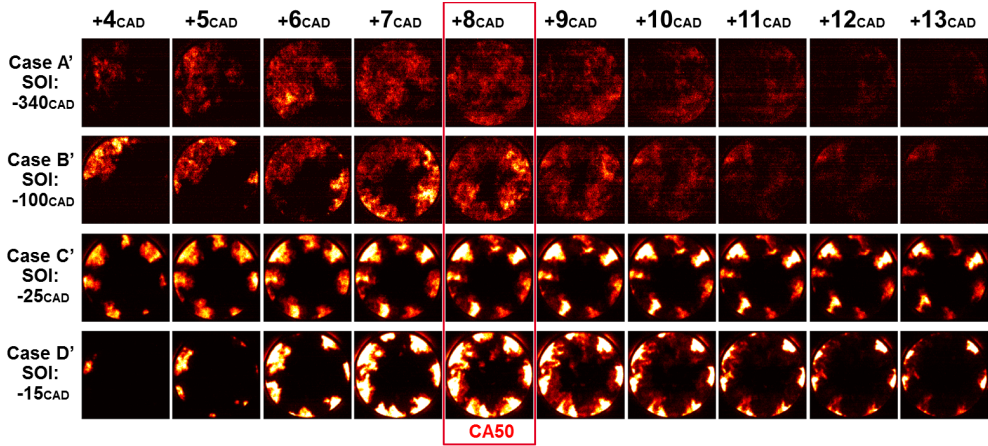


Figure 5.10: Representative bottom-view OH^* bandpass images around CA50 (8 CAD) for different cases (A'-D').

5.4.1 Angular, Radial and Vertical Stratification

The images captured from below are used to determine both angular and radial stratification, while side view images are used to determine the vertical stratification. Results of the combustion stratification for different injection timings are demonstrated in Fig. 5.11. As expected, the stratification levels of PPC combustions (SOI of -15 and -25 CAD) are higher than those of HCCI like combustion (SOI of -100 CAD and port injection), due to the shorter ignition delay which limits the fuel-air mixing process. For the late injections, however, the maximum angular, radial and vertical stratifications reach values close to 1, which doesn't allow to distinguish between SOI of -15 and -25 CAD. For early injections, the maximum level of stratification exceeds 0.4, which is relatively high, especially for the port fuel injection case, which is supposed to result in homogeneous combustion. This is all an artifact of the analysis. Figure 5.10 shows that radial lines and circles with mean intensities close to 0 (black color) can be easily found for all cases. This means that I_{min} in Eqs. 3.2 and 3.3 tends to 0, which automatically increases the stratification level towards 1, even for HCCI case A' (discussed in section 5.3.3 in relation to Fig. 5.8b).

As a noteworthy fact, a relatively high level of stratification is observed around 45 CAD for

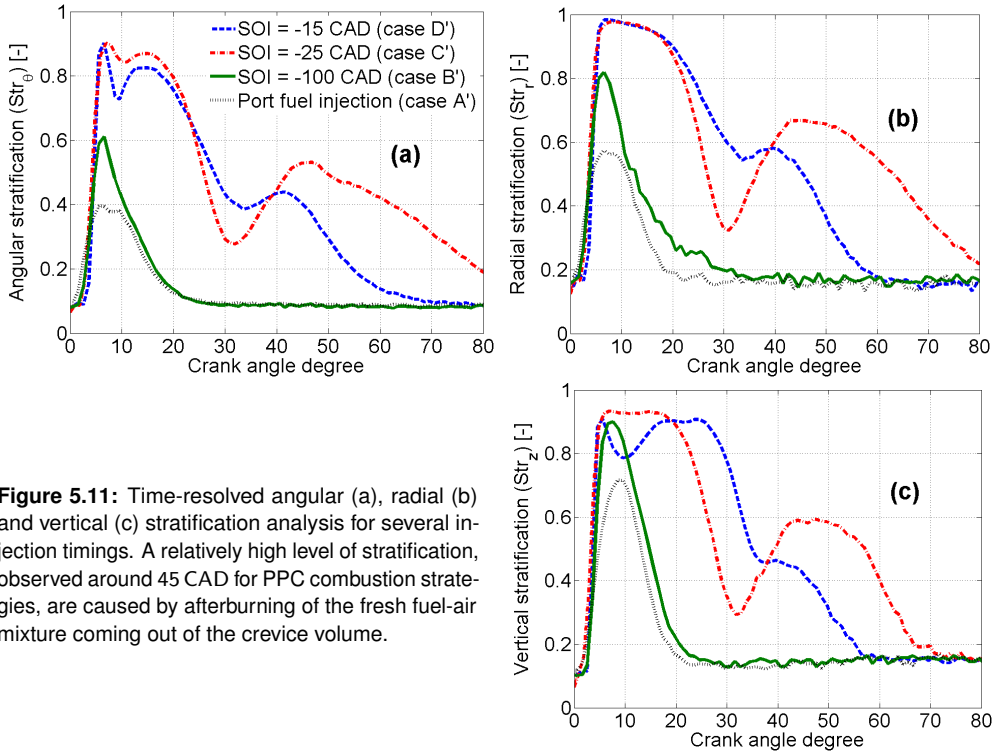


Figure 5.11: Time-resolved angular (a), radial (b) and vertical (c) stratification analysis for several injection timings. A relatively high level of stratification, observed around 45 CAD for PPC combustion strategies, are caused by afterburning of the fresh fuel-air mixture coming out of the crevice volume.

PPC combustion strategies (C' and D'). This is caused by afterburning of the fresh fuel-air mixture coming out of the crevice volume as discussed in chapter 3. This crevice fuel does not burn under the low temperature combustion conditions of HCCI cases. Obviously, the crevice fuel does not significantly contribute to the heat release. However, small intensity variations in chemiluminescence images can easily increase the intensity-based stratification level, as discussed in the previous paragraph. When comparing the results of the angular, radial and vertical stratifications, it is observed that the vertical approach leads to the highest stratifications. The weak combustion close to the relatively cold cylinder head and piston crown brings down the minimum vertical intensity close to the 0 during a combustion event, and hence yields a relatively large Str_z (Eq. (5.1)).

5.4.2 Fourier-based Stratification

The results of the Fourier-based stratification analysis for both bottom and side view imaging are given in Fig. 5.12. It is observed that the level of stratification is close to 0 for HCCI combustion strategies, while for PPC combustion the stratification level is significantly higher. There is a good level of distinction between stratification levels for SOI -15 and -25 CAD (higher stratification for later injection), illustrating how, contrary to the previous definitions, this Fourier-based definition allows to compare stratification levels of different PPC strategies. The

weak afterburning near the cylinder walls does not have a significant effect on the stratification in the Fourier-based analysis, as it should, because it does not significantly contribute to the heat release. The level of stratification is also 0 for images in which nothing is detected. It indicates that the method is sensitive to the temporal behavior of heat release rate, while it is not particularly sensitive to noise and insignificant intensity variations. The reason for this improvement offered by the Fourier-based stratification definition is twofold. The method focuses on the signal energy in the low-frequency part of the spectrum (thus disregarding noise), and the normalization is based on the highest possible signal energy, which provides a meaningful and objective outcome. Note that the Fourier-based stratification metric does not follow the order found in the peak heat release rates as can be seen by comparing Figs. 5.9a and 5.12a, while the temporal behaviors are similar. This also implies that for controlling the peak heat release rate, an optimum stratification level is needed and quantification of combustion stratification can be used as a tool for this optimization. The higher stratification level of case C' has lowered the peak heat release rate compared to case B' (an almost homogeneous case). However, the higher stratification level of case D' compared to case C', has increased the peak heat release rate, apparently because higher local equivalence ratios close to stoichiometric are achieved.

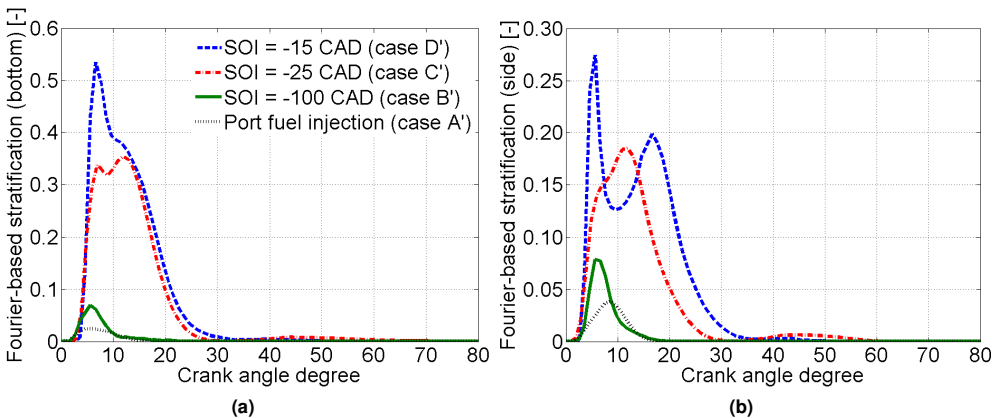


Figure 5.12: Time-resolved Fourier-based stratification analysis for various injection timings and bottom (a) and side (b) view images.

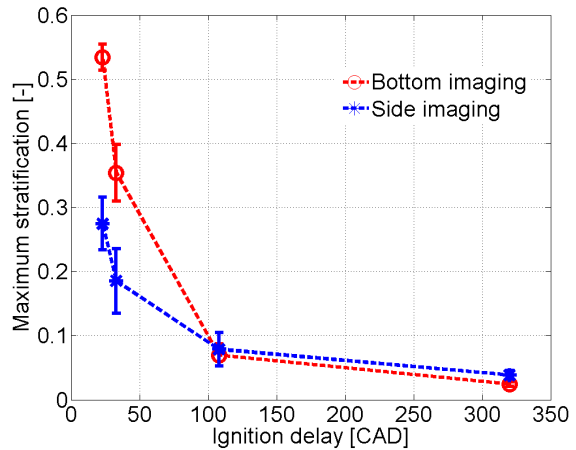
Fourier-based stratification analysis is performed for the side view images as well, in their original coordinate system (Fig. 5.12b). For SOI of -15 CAD, the stratification level drops around 10 CAD, but this is due to an experimental artifact, namely overexposure of the camera (overexposure can reduce the signal energy and the stratification level). Initially to eliminate the effects of camera intensifier gain factor on results of different methods, gain was kept constant for HCCI and PPC points. This caused the overexposure for SOI -15 CAD, while lower intensifier gain factors could strongly decrease the signal intensity of HCCI combustion strategies. However, variable intensifier gain factors can be implemented in future studies to avoid losing information, but a correction should be made later for the gain factor.

Figure 5.13 shows the maximum Fourier-based stratification achieved in a cycle as a function

of ignition delay. Here, the ignition delay is defined as the difference between start of injection (command) and CA10. It is observed that for increasing ignition delay the combustion stratification decreases. Regarding PPC points with small ignition delays, the lower stratification level of side view images is due to the overlap of individual combustion clouds in the line-of-sight imaging in side view. Similar stratification levels are obtained for longer ignition delays, since the homogeneity is then independent of the line-of-sight. Obviously, the results of imaging from below are more reliable considering the distinction of individual combustion clouds.

The results presented in this study might seem contradictory to the results obtained in the previous chapter 3. In that study it was stated that the combustion stratification decreases by retarding the SOI from -25 CAD to TDC. However, the CA50 was not kept constant for different injection timings in chapter 3, while the emphasis of this study is on the influence of ignition delay by keeping the CA50 constant.

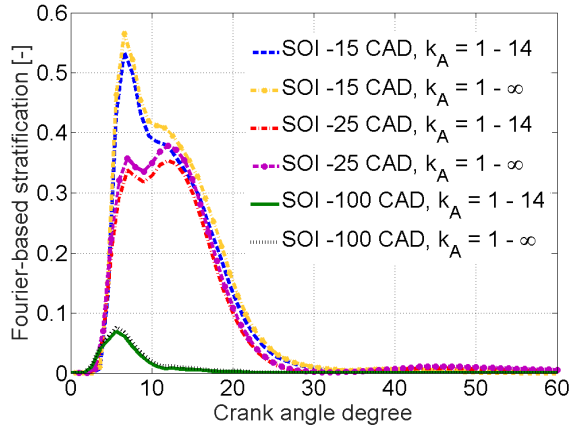
Figure 5.13: Maximum combustion stratification (Fourier-based) versus ignition delay for both bottom and side view imaging. Error-bars represent standard deviations over 30 cycles. By increasing the ignition delay, the combustion stratification decreases.



5.4.3 Effect of the Considered Spatial Frequency Range

The Fourier-based stratification definition is based on a selected specific spatial frequency range ($f : 1 \leq k_A \leq 2n$) to suppress noise and to focus only on typical frequencies that make up the stratified combustion (Fig. 5.7). The effect of the selected frequency range is illustrated in Fig. 5.14, where the combustion stratification based on the whole frequency domain is compared to the stratification based on a limited frequency range. Figure 5.14 confirms that the Fourier-based stratification method is not sensitive to high-frequency components. Apparently, their energy is low in comparison with the energy of low frequencies. However, analyzing the artificial sample images of Fig. 5.8 shows that the extension of the frequency range to infinity increases the Fourier-based stratification level of homogenous image (Fig. 5.8b) from 0.01 to 0.32, since the energy of high spatial frequencies is significant in that image (pixel to pixel variations), while it does not have any effect on the stratified image (Fig. 5.8a), since the energy of high spatial frequencies was almost 0 in that image.

Figure 5.14: Effect of the considered spatial frequency range on Fourier-based stratification metric. Two different frequency ranges are considered: $f : 1-14$ and $1-\infty$ for three different injection timings.



5

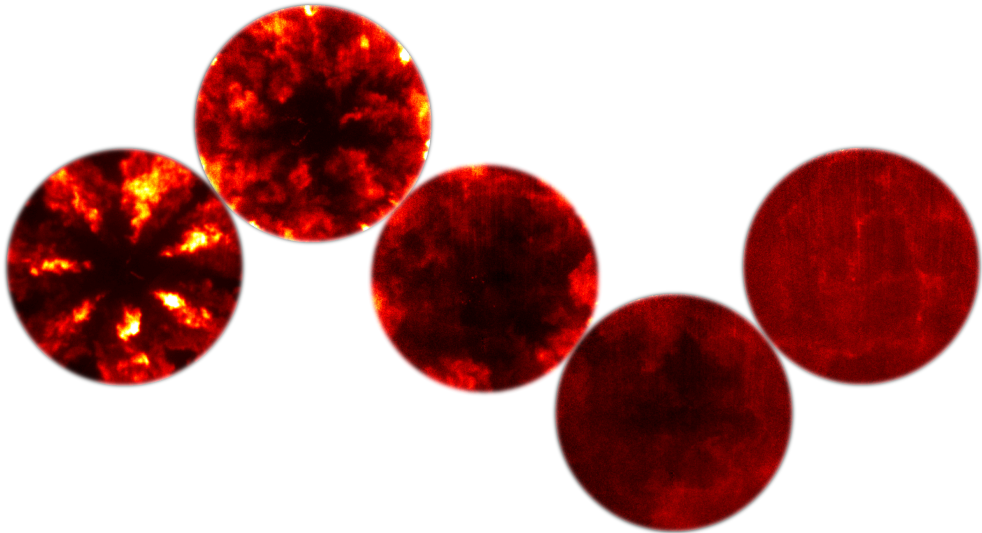
5.5 Conclusions

OH* bandpass imaging was performed in order to analyze the combustion in a light-duty optical engine. The objective of this study was to evaluate different metrics to quantify 'combustion stratification' of Partially Premixed Combustion. A new methodology is proposed based on the spatial frequency domain of OH* bandpass images to quantify the combustion stratification. Regarding this method, the following is concluded:

- Fourier-based stratification analysis is an objective method to compare the stratification of different combustion strategies, ranging from homogeneous HCCI combustion to stratified PPC combustion, and it clearly distinguishes those two regimes.
- Fourier-based stratification analysis of OH* bandpass-filtered images corresponds to the temporal behavior of heat release rate (not the peak orders) as an indicator of the combustion, whereas other definitions clearly do not.
- Low spatial frequencies contribute to the majority of the signal energy and combustion stratification.
- The rejection of high spatial frequencies renders the Fourier-based method relatively insensitive to noise.
- Results confirm that combustion stratification generally drops by increasing the ignition delay. However, there is an optimum combustion stratification level in the PPC regime where the peak heat release rate can be the lowest.

The method can also be implemented to analyze fuel stratification, based on e.g. fuel tracer Laser-Induced Fluorescence (LIF) measurements or other fuel-mixing indicator methods. Also, it is amenable to stratification analysis of numerical results.

Fuel Stratification



This chapter is based on the following publications:

Izadi Najafabadi, M., Somers, B., Johansson, B., Dam, N., (2017) “**Fuel Stratification Study of Partially Premixed Combustion Using Fuel-Tracer LIF**”, *Applied Physics B: Lasers & Optics*, under review.

Izadi Najafabadi, M., Dam, N., Somers, B., Johansson, B., (2016) “**Fuel and Combustion Stratification Study of Partially Premixed Combustion**”, *ECCO-MATE Conference I: Combustion Processes in Marine and Automotive Engines*, Lund, June 2016.

6.1 Introduction

The Partially Premixed Combustion (PPC) concept relies on a relatively long ignition delay, compared to conventional diffusion-controlled combustion, to achieve a partially premixed charge [5, 19, 20]. The amount of premixing in the PPC regime can be controlled in various ways, for instance by tuning the injection timing. Control of premixing is necessary to implement PPC combustion strategies and to improve the emission formation [21].

Fuel-tracer Laser-Induced Fluorescence (LIF) is widely used to measure the fuel distributions for various combustion modes [71–74]. In the LIF technique, molecules of the species of interest are excited by absorption of a laser photon of a selected energy. A transition takes place to a higher predetermined discrete energy level, followed by spontaneous photon emission (or interaction with the environment) [71]. Since there are multiple possibilities for the transition on which spontaneous photon emission can occur to a lower discrete energy level, there is a fluorescence spectrum. Both the excitation wavelength and the fluorescence spectrum are characteristic for the tracer, which allows to selectively monitor the tracer distribution in space and time.

In the partially premixed regime, fuel-tracer LIF is used in some studies to investigate the mixing process and its effects on the combustion behavior. Petersen et al. investigated the pre-combustion equivalence ratio distribution in a light-duty diesel engine under PPC conditions [74]. The tracer-based LIF technique was used in their optical engine with a production-like piston bowl to obtain quantitative results. The measured equivalence ratio distributions were combined with previous in-cylinder velocity and CO measurements [75, 76] to interpret combustion behavior and emissions. Fuel reactivity stratification was investigated by Kokjohn et al. as a method to control the heat release rate in a heavy-duty optical engine [77]. Quantified results were achieved by coupling a thermodynamic model to the LIF images of toluene as a tracer. Tang et al. studied a double injection strategy of PPC on a light-duty optical engine [78]. The fuel/air mixing of PPC was evaluated using fuel-tracer LIF. Double injection strategies with different first injection timing and fuel mass portioning between the two injections were compared, using PRF70 as a fuel. They showed that PPC was initiated by multipoint auto-ignition in locations where the local equivalence ratio was relatively high. The flame fronts of these ignition kernels subsequently expanded to the regions with lower fuel concentration. Another study, by Musculus et al., investigated fuel stratification to explain the emissions of a low-temperature combustion diesel engine [79]. Also in this study, toluene fuel-tracer fluorescence diagnostics was used to quantify the fuel distribution for various injection timings. As one of the most recent studies, Wang et al. used fuel-tracer LIF technique to study the mixing process in a transition from HCCI mode to PPC mode in a heavy-duty optical engine [80]. They did their measurement in a realistic piston bowl geometry without quantification of results. They could recognize four different mixing schemes as the SOI timings were varied during the transition from HCCI to PPC.

The present research aims to objectively quantify the fuel stratification in PPC, based on results of fuel-tracer LIF, and to investigate its relation to the spectral signature of the spontaneous combustion luminosity. To this end, an objective metric for fuel stratification is introduced, which

can be used as a tool in future investigations for optimization of fuel stratification.

Quantified results of fuel distribution are obtained by measuring the temperature dependency of toluene fluorescence (as the tracer) and the thermodynamic analysis of the fuel-tracer LIF images by using a much more efficient algorithm than available in literature. The effects of the injection timing on the fuel stratification and the heat release rate behavior are investigated. High-speed OH^* bandpass imaging (chapter 5) is used to investigate the combustion stratification and spatial information regarding the heat release rate. The fuel distribution results are linked to the spectroscopy study (chapter 4) as well, to investigate the effect of local fuel/air ratios on thermal radiation, broadband chemiluminescence, OH^* , CH^* and C_2^* chemiluminescence. A new metric for fuel stratification is presented based on two-dimensional Fourier analysis of fuel distribution. In the end, the effect of intake temperature on fuel stratification is investigated.

6.2 Fuel-Tracer LIF Setup

Toluene is used in this study as a fuel-tracer because of its expected stability at high temperatures [71]. In addition, toluene has a similar boiling point (110°C) as n-heptane (98°C) and iso-octane (99°C), which enables toluene to trace the PRF70 fuel (70 % by volume iso-octane and 30 % by volume n-heptane) quite well. A disadvantage of using a fuel tracer like toluene is that the fluorescence yield decreases exponentially when the temperature increases: a factor of 10 decrease every 215 K, which needs to be taken into account for interpreting the results [79]. PRF70 is doped with toluene by 1 % volume. This amount of toluene has been chosen to balance signal strength against undue laser light attenuation [79]. The experiments have been done with pure nitrogen instead of air to avoid the quenching effect of oxygen.

The fuel-tracer LIF setup is schematically illustrated in Fig. 6.1. Toluene is excited by a laser light sheet of 1 mm thickness and 60 mm width, entering the combustion chamber through a quartz liner to ensure that the entire access of the optical piston is used. The height at which the laser sheet enters the combustion chamber is set halfway between the cylinder head and the piston crown at top dead center. Since toluene can be excited by 266 nm radiation, a frequency-quadrupled Nd:YAG laser is used. The toluene fluorescence is detected by a blue-optimized intensified CCD camera (PI-MAX 1; Roper Scientific) through a 280-340 nm bandpass filter. The toluene fluorescence emission is in the range of 260-340 nm [71], however, to avoid capturing elastically scattered laser light at 266 nm, the bandpass region has been limited to 280-340 nm. The specifications of the imaging system are shown in Table 6.1. All measurements are performed with constant

Quantitative measurements of fuel distribution need calibration of the fluorescence signal based on a well-determined fuel/tracer density. In this study, a homogeneous mixture is made by early injection of a specific amount of toluene-doped fuel at -340 CAD ATDC and calibration images are recorded at TDC position. This method is also used in literature for making homogeneous calibration images [77, 79]. These calibration images are recorded for 100 cycles exactly before and after each experimental point. The mean of all these calibration images is used for each

Figure 6.1: Schematic of Fuel-Tracer LIF setup. Laser light sheet at wavelength of 266 nm enters the combustion chamber through the quartz liner. Consequently, fluorescence of excited toluene molecules passes through the optical piston, is reflected by the stationary 45° tilted mirror, and recorded by the intensified camera through a 280-340 nm bandpass filter. The laser light sheet with 1 mm thickness and 60 mm width is produced by a frequency-quadrupled Nd:YAG laser.

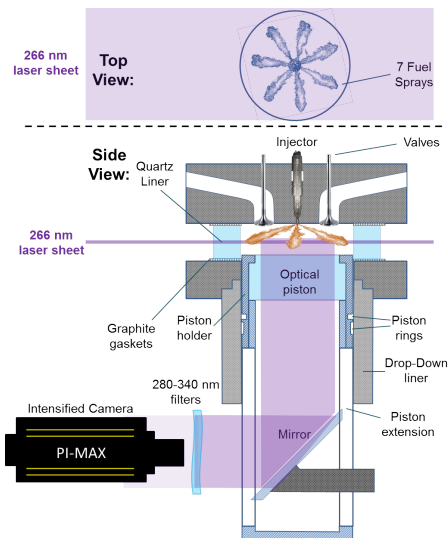


Table 6.1: Specifications of the imaging system.

Camera	PI-MAX 1, GEN II Intensified
Imaging sensor	16 bit CCD
Resolution	1024 × 1024 pixel ²
Frame rate	1 fps
Exposure time	200 ns
Objective lens	UV Bernhard Halle Nachfl. 100 mm f/2
1 st filter	300 nm bandpass filter with 80 nm FWHM
2 nd filter	280 nm longpass filter

measurement point in the quantification procedure to suppress the effect of probable laser power fluctuations.

For each operating condition, 100 cycles were recorded at TDC position. TDC position was chosen since for all the operating conditions, the main heat release starts at or a bit after TDC. Before each measurement point, 100 cycles were recorded again at TDC position without any injection while the laser was running. The average of these latter images was used for background subtraction, as will be discussed in section 6.3.

6.2.1 Operating Conditions

The set of operating conditions are exactly those used in chapter 5 (see Table 5.2). Combustion phasing, namely CA50, is kept constant for four different single-injection timings by tuning the intake temperature, resulting in four different ignition delays and different levels of stratification. However, for fuel tracer LIF measurements, pure nitrogen is used at the intake instead of air.

The pressure traces and high-speed OH* bandpass images are the same as those presented in chapter 5.

In order to see the effect of fuel stratification on combustion spectra, the operating conditions of the high-speed spectroscopy study (chapter 4) are also repeated in this study for fuel-tracer LIF measurements, to be able to make a direct link between them. These experimental points are presented in Table 4.2; they are quite similar to those presented in Table 5.2, just a bit higher in amount of injected fuel and oxygen percentage.

6.3 Post-processing of LIF Images

6.3.1 Background and Flat Field Corrections

Before starting the quantification procedure, the mean background image was subtracted from all LIF images, including the calibration images. To correct for laser sheet non-uniformities and variations in individual pixel sensitivities, a flat field correction should be applied. The flat field correction was based on the mean of 100 nominally identical calibration images. This mean image should be uniform because the calibration images were recorded on a homogeneous distribution. Hence, a correction factor was applied to each pixel in order to obtain the same mean calibration intensity at each pixel. These pixel correction factors were subsequently applied to all LIF images.

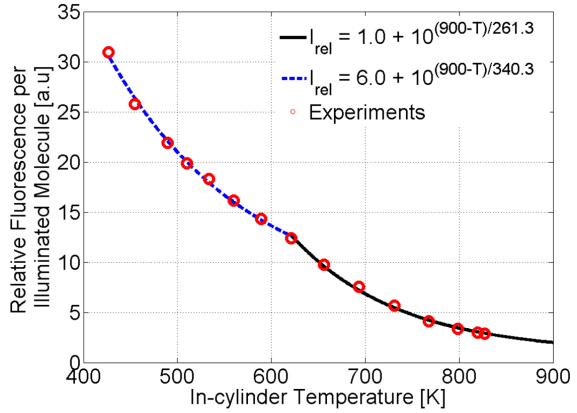
6.3.2 Temperature Dependency of Toluene Fluorescence

By increasing the temperature from 300 to 1000 K, the toluene fluorescence signal, upon 266 nm excitation, decreases by two orders of magnitude [71]. Stratification of the in-cylinder fuel distribution will result in non-uniformities of temperature because of temperature differences between the injected fuel and the in-cylinder charge (oxidizer), evaporative cooling and compression of gases with different heat capacity ratios. This means the in-cylinder LIF images of toluene contain information on both fuel density and temperature. To decouple these two parameters, the temperature dependency of the toluene signal should be determined at first. Since the toluene fluorescence signal has been limited using bandpass filters (280-340 nm), the temperature dependency measurements were done in the same experimental setup. A homogeneous mixture was made by early injection at -340 CAD ATDC, the same as for the calibration images. Then, LIF images were recorded at different positions during the compression stroke from -80 CAD to TDC. The average fluorescence signal at each crank angle degree (after background subtraction) was then corrected for compression density in order to see the effect of temperature.

Considering the fact that the field of view (FOV) was limited to 60 mm out of 81 mm bore diameter, far enough from cylinder walls, it is assumed that there is no heat transfer/loss in this region. Hence, the temperature at each CAD was determined based on a simple thermodynamic model considering the heat capacity ratios of nitrogen, iso-octane and n-heptane. Results of

fluorescence signal as a function of temperature are presented in Fig. 6.2.

Figure 6.2: Relative toluene fluorescence signal as a function of temperature. Toluene fluorescence signal is based on LIF images of a homogeneous mixture at different strokes during compression (from -80 CAD to TDC), corrected for compression density. Temperature is determined using a thermodynamic model.



As shown in Fig. 6.2, the behavior of fluorescence signal is somewhat irregular, and best fitted by two segments. For temperatures higher than 620 K, similar behavior was reported by Kokjohn et al. [77] for the same temperature range. They even found a similar equation as noted in Fig. 6.2. For lower temperatures, there is a red shift in toluene fluorescence spectra [81] which causes more signal to be blocked, considering the limited bandpass region (280-340 nm). That can be the reason of the slightly suppressed toluene fluorescence signal at lower temperatures (less than 620 K). It is also noteworthy that temperatures lower than 620 K are barely achieved considering the thermodynamic conditions of our experimental points.

6.3.3 Quantification Procedure

The logic of the quantification procedure in this study is similar to the procedures used by Sahoo et al. [73] and Kokjohn et al. [77], but with some changes to improve the efficiency of post-processing. The procedure used by Sahoo et al. [73] and Kokjohn et al. [77] was based on a numerical loop for each pixel including the following steps:

1. Assume a homogeneous distribution of temperature throughout the combustion chamber.
2. Estimate the fuel molar density for each pixel, based on the recorded LIF images pixel intensity, calibration data, and temperature dependency of toluene.
3. Estimate the temperature for each pixel based on its fuel molar density calculated from step 2 and using a thermodynamic model which considers the adiabatic evaporation/mixing and compression process from SOI.
4. Back to step 2 by updating the temperature of each pixel and continue the loop until convergence is achieved.

This procedure was overly time consuming for this study; running a convergence loop for 1 million pixels per image, while having 100 images for each measurement point. Hence, a

different, less time-consuming quantification procedure is used in this study, as schematically illustrated in Fig. 6.3. It essentially boils down to the creation of a look-up table for fuel mole fraction, since, for every operating condition, there is a unique relation between fuel mole fraction, temperature at TDC, and LIF signal yield.

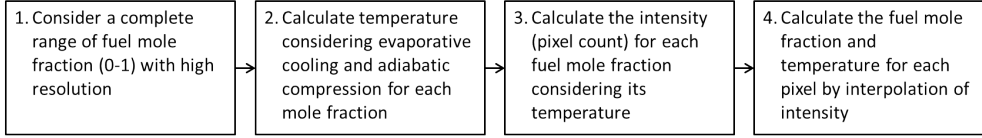


Figure 6.3: Quantification procedure used for toluene fuel tracer LIF images.

Firstly, a complete range of fuel mole fraction is considered from 0 to 1 with a high resolution (10^{-4} in this study). Secondly, the temperature for each fuel mole fraction at TDC (our chosen instant of measurement for all operating conditions) is estimated based on adiabatic evaporation/mixing (fuel temperature is needed) and compression for each operating condition. In the third step, the pixel count (intensity) is calculated for each mole fraction at its temperature at TDC using Eq. (6.1):

$$I = C \cdot I_{rel}(T) \cdot n_f \cdot \rho_m \quad (6.1)$$

in which I is intensity, $I_{rel}(T)$ is the relative fluorescence intensity (Fig. 6.2) at the estimated temperature (step 2), n_f is fuel mole fraction, ρ_m is the molar density (at TDC) for the given temperature and C is the calibration constant calculated from Eq. (6.2):

$$C = \frac{I_{cal}}{I_{rel}(T_{cal}) \cdot n_{f_{cal}} \cdot \rho_{m_{cal}}} \quad (6.2)$$

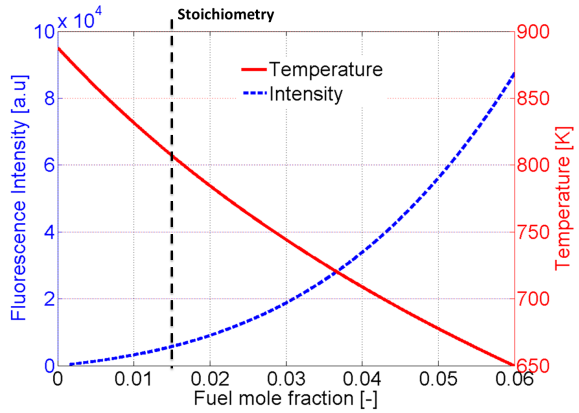
in which the symbols have the same meaning as above, but now for the calibration conditions. The ratio of molar densities (substitution of Eq. (6.2) in Eq. (6.1)) can easily be calculated from the ideal gas law:

$$\frac{\rho_m}{\rho_{m_{cal}}} = \frac{P \cdot T_{cal}}{P_{cal} \cdot T} \quad (6.3)$$

where pressures (P_{cal} and P) are experimentally measured for the calibration point and each operating condition at TDC. Figure 6.4 shows the results of temperature and fluorescence intensity as functions of fuel mole fraction for case C' (see Table 5.2). The maximum pixel value for a 16 bit camera (used in this study) is 65 535 ($= 2^{16} - 1$), where a fuel mole fraction higher than 0.06 could not be measured for this case. Such figures are saved as a table for each operating condition. The last step is using this lookup table to interpolate the intensity at each pixel of LIF images and finding the fuel mole fraction and temperature for that pixel. This procedure reduced the time costs of the post-processing significantly, since it is needed once only to calculate a table such as Fig. 6.4 and everything else is just a fast interpolation.

Moreover, the divergence issues can not affect the post-processing procedure.

Figure 6.4: Toluene fluorescence and temperature as functions of fuel mole fraction for case C' (Table 5.2). There is a unique relation between fuel mole fraction, temperature at TDC, and fluorescence intensity. Note that such a graph (or look-up table) should be made for every individual operating conditions, laser pulse energy and camera settings.



6.4 Results and Discussion

6.4.1 Fuel, Thermal and Combustion Stratification

The heat release rate behaviors for different injection timings (cases A'-D' of 5.2) were presented in Fig. 5.9a. In case A', homogeneous mixture and combustion are achieved by early injection at -340 CAD. Cases C' and D' represent partially premixed combustion with different injection timings (-25 and -15 CAD, respectively) and therefore different charge stratification levels, whereas case B' with SOI at -100 CAD can be classified as a transition point from HCCI to PPC.

In order to analyze the heat release rate behavior for different cases, fuel and thermal distributions at TDC, determined by fuel-tracer LIF, are demonstrated in Fig. 6.5, together with OH* bandpass images around CA50 (3-13 CAD ATDC). Fuel/thermal distributions and OH* bandpass images are depicted for an average of 100 cycles and 30 cycles, respectively, as well as for individual, representative cycles (labeled 'sample' in the figure).

It should be noted that the LIF measurements are performed with pure nitrogen as intake gas, hence, OH* bandpass images are recorded from another set of experiments with nominally identical settings. Moreover, OH* bandpass images are line-of-sight integrals, while fuel and thermal distributions are planar sections. Results in Fig. 6.5 shows that different levels of fuel and thermal stratifications have been produced at TDC by different injection timings, which affect the heat release rate and combustion behavior. Each case is discussed below.

Case A' (SOI at -340 CAD): The mean fuel and thermal distributions are homogeneous without any specific pattern, although individual cycles show random inhomogeneities; spots with higher equivalence ratios and (therefore) lower temperatures. These small and random inhomogeneities which are still in the lean region (equivalence ratio < 1) cause ignitions at random locations, which slowly propagate (based on individual OH* movies). The so-called

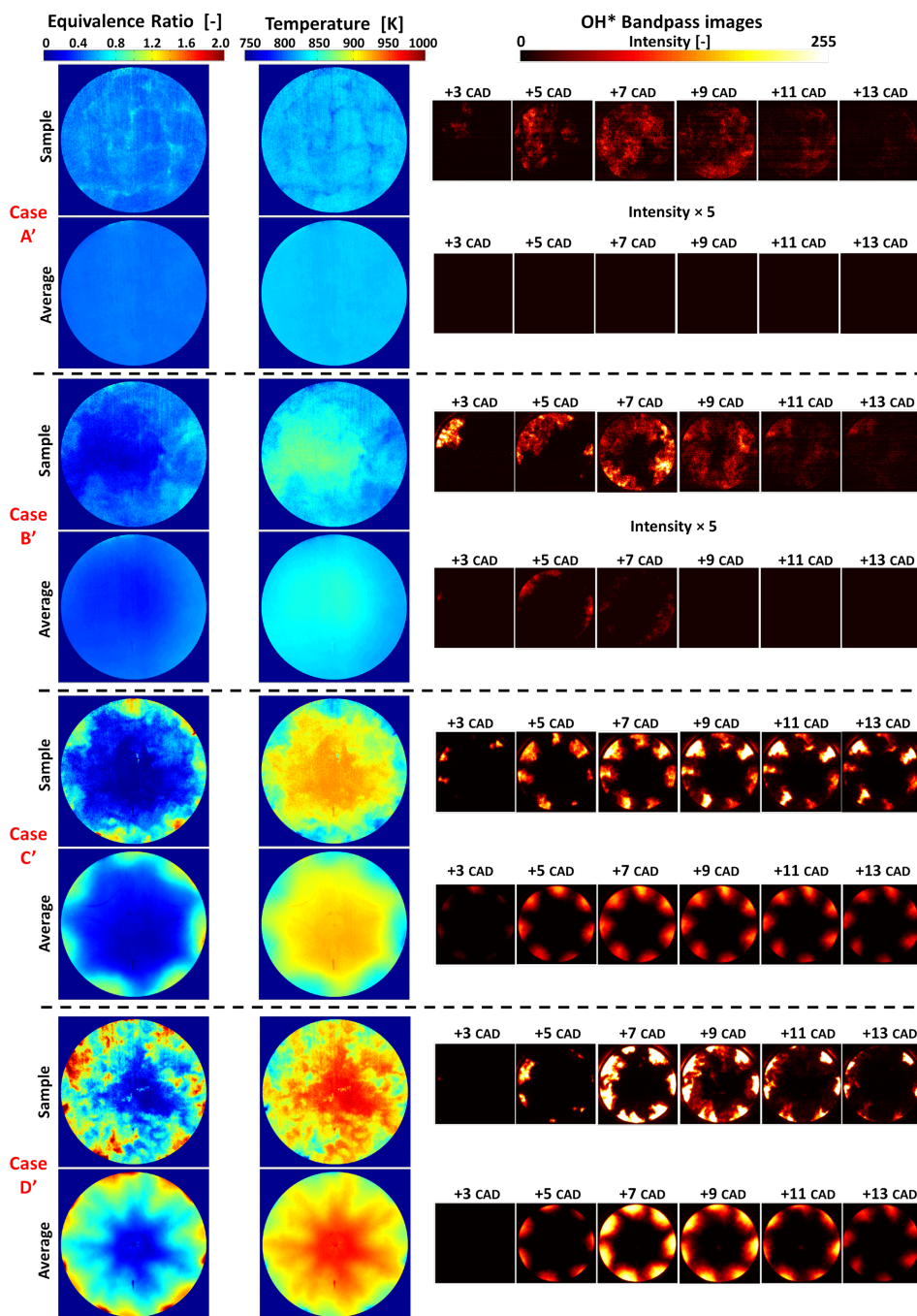
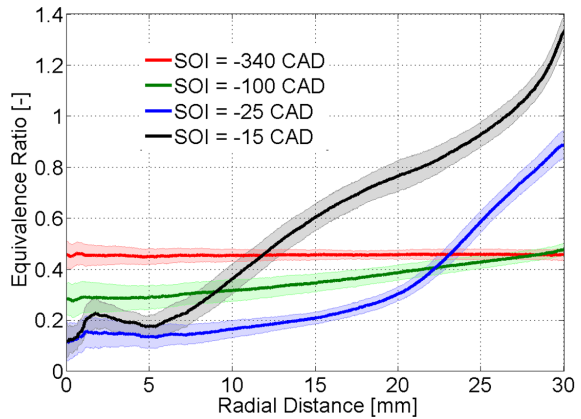


Figure 6.5: Fuel (left) and thermal (middle) distributions at TDC as well as OH* bandpass images (right) around CA50 for different charge stratification levels (Table 5.2). For the sake of clarity, the intensity of OH* bandpass images for cases A' and B' are multiplied by 5. Earlier images than 3 CAD are not shown because they were all black.

over-lean effect has increased the combustion duration and consequently lowered the peak heat release rate compared to other cases. The mean OH^* bandpass images do not show any pattern, confirming the random inhomogeneity behavior.

Case B' (SOI at -100 CAD): Fuel distributions show a radial increase of fuel density, while it is locally in the lean region and angularly not significantly stratified. A somewhat asymmetric distribution can be caused by the tumble motion. This monotonous increase of equivalence ratio is better shown in Fig. 6.6, where angularly averaged equivalence ratios are plotted as a function of radius for all cases studied.

Figure 6.6: Angularly averaged equivalence ratios as a function of radius for different injection timings. The shaded regions represent standard deviations over 30 cycles. Note that the bore radius is 40.5 mm; the other 10.5 mm is not optically accessible.

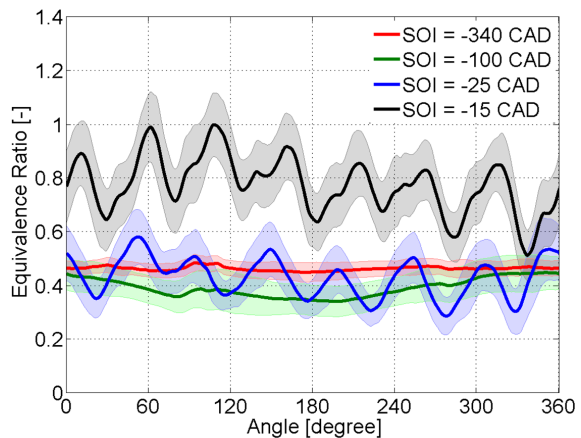


Close to the center of the combustion chamber, the mean equivalence ratio for case B' is much lower than that for case A'. With increasing distance from the center of combustion chamber, the mean equivalence ratio for case B' goes higher than the one for case A', which is almost a horizontal line (homogeneous). Note that the cylinder radius is 40.5 mm, and significantly higher equivalence ratios for case B' close to the cylinder walls are expected, based on the behavior shown in Fig. 6.6. Based on the OH^* chemiluminescence imaging (Fig. 6.5), the combustion always starts from the regions close to the cylinder walls (higher equivalence ratio) and propagates toward the center of combustion chamber. This can also be seen in the mean OH^* bandpass images, although it is a weak pattern. The other difference between case B' and case A' is a relatively higher temperature for case B' caused by later injection (related to the heat capacity ratio during the compression stroke). To summarize case B' it should be mentioned that higher equivalence ratios close to the cylinder walls without any significant angular stratification accompanied by a slightly higher temperature compared to case A', cause spontaneous ignition close to the cylinder walls, which propagates fast towards the center of the combustion chamber and leads to a much higher peak heat release rate compared to case A'.

Case C' (SOI at -25 CAD): There are explicit stratification patterns for fuel and temperature, both radially and angularly (Fig. 6.5). The radial increase of equivalence ratio is stronger than for case B' (Fig. 6.6), as expected, since there has been less time for mixing. Moreover, this increase is not linear any more probably because the spray hits the piston (more information regarding the spray targeting can be found in chapter 3). To see the angular stratification, the

radially averaged equivalence ratio is plotted as a function of angle in Fig. 6.7 for different injection timings (Table 5.2).

Figure 6.7: Radially averaged equivalence ratios as a function of angle for different injection timings. The shaded regions represent standard deviations over 30 cycles. Seven fuel clouds are easily distinguishable for late injection timings (cases C' and D'). Slightly different angular phases of fuel clouds for cases C' and D' are the consequence of swirl motion.

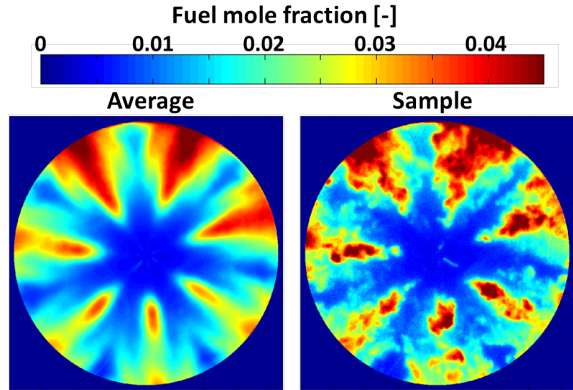


Seven fuel clouds can clearly be distinguished in Fig. 6.7. The emergence of this angular stratification is the main difference between case C' and the previous cases (A' and B'). The local fuel/air ratio (Fig. 6.5) is close to stoichiometric and a bit higher at the core of each fuel cloud and gradually decreases moving away. The temperature behaves inversely, it will increase by moving away from the core of each fuel cloud. Ignition starts in regions with equivalence ratio around 1, even though these have lower temperature, and propagates toward the lower equivalence ratio regions (with higher temperatures). The mean OH* bandpass images (and also the individual ones) in Fig. 6.5 clearly show that ignition starts at 3 CAD in the high equivalence ratio regions and propagates toward the low equivalence ratio regions at 5 CAD and later. Although the local fuel/air ratios are higher for case C' compared to case B', the peak heat release rate of case C' is lower than the one of case B', related to the significant angular stratification for case C'.

Case D' (SOI at –15 CAD): Fuel and thermal distributions at TDC are highly stratified since it is just a few crank angle degrees after the end of injection. Locally rich regions are much larger than those of case C', and generally at higher temperatures (because of higher intake temperature). However, the fuel clouds are a bit irregular and closer to the center of the combustion chamber. One of the reasons is that the sprays hit the piston closer to the center compared to case C'. OH* bandpass images show the same story as in case C': ignition at high equivalence ratio regions, propagating towards low equivalence ratio regions. However, there are two differences. Firstly, the intensities of OH* images for case D' are much higher than those of case C', attributable to even higher local equivalence ratios and temperatures. Secondly, the combustion clouds propagate more towards the center of combustion chamber, as expected based on fuel distributions. Figures 6.6 and 6.7 show that case D' is the most radially and angularly stratified with the highest equivalence ratios. These high fuel/air ratios close to stoichiometric and above, lead to significantly higher peak heat release rate. The same trend was reported by Kokjohn et al. [77] for SOI at –15 CAD in a heavy-duty optical engine, where high fuel stratification sharpened the heat release rate.

To better understand the effect of SOI on mixing process, the distribution of fuel mole fraction at TDC for SOI at -10 CAD (so TDC is almost at the end of injection) is demonstrated in Fig. 6.8. This is one of the most stratified distributions, in which the structure of each spray is completely clear. However, it was not possible to have the same CA50 for this point, even at high intake temperatures (up to 430 K). Note that higher fuel densities for the upper three sprays are not due to laser absorption, since the laser was entering the combustion chamber at the bottom side of the images. These higher fuel densities are probably due to hole-to-hole variations of the injector.

Figure 6.8: Fuel mole fraction distribution at TDC for SOI at -10 CAD, intake temperature of 348 K and injection duration of 5.4 CAD. There is no combustion experiment recorded for this case. Hence, results are presented based on fuel mole fraction (a mixture of nitrogen and fuel). Left: average of 100 cycles; right: an individual cycle. The laser enters the combustion chamber at the bottom side of the images.



To summarize this section, we conclude that fuel stratification alone can both decrease or increase the peak heat release rate. In the homogeneous regime, over-lean effect or smooth patterns of fuel distribution play a main role as discussed for cases A' and B'. To decrease the peak heat release rate in the PPC regime, the angular stratification plays a significant role, however, local fuel/air ratios close stoichiometric and richer should be avoided.

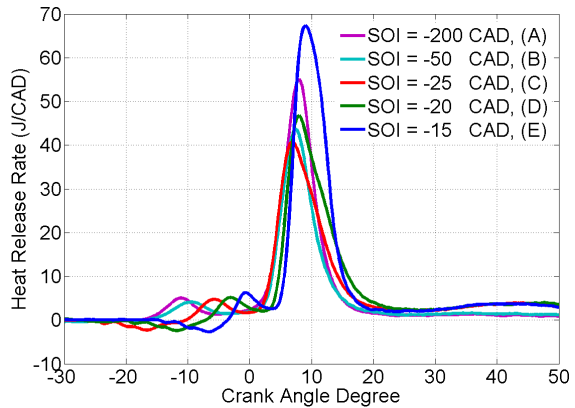
6.4.2 Fuel Stratification and Spectral Signature

In this section, results of fuel distribution for the same experimental points as in the previous spectroscopy study (chapter 4) are presented and linked to those spectroscopy results. The heat release rate behavior for these experimental points (cases A-E of Table 4.2) is shown in Fig. 6.9. In case A, almost homogeneous mixture and combustion are achieved by early injection at -200 CAD. Cases B to E with SOI from -50 to -15 CAD represent partially premixed combustion with different levels of stratification.

Fuel distributions for different injection timings are depicted in Fig. 6.10 for an average of 100 cycles and an individual one together with the normalized results of combustion spectroscopy (see also Fig. A.1 in the Appendix), including thermal radiation, broadband chemiluminescence, OH^* , CH^* and C_2^* chemiluminescence.

Regarding the effect of fuel stratification on heat release rate, a similar behavior as in the previous section is seen. For SOI at -200 CAD (case A), a radial increase of fuel density is seen, similar to case B' (SOI at -100 CAD) in the previous section, which leads to a sharp heat

Figure 6.9: Heat release rate as a function of crank angle degree for different injection timings (Table 4.2). Pressure tracers were shown in Fig. 4.3. Case A is almost HCCI combustion by early injection at -200 CAD, while cases B to E (SOI from -50 to -15 CAD) are PPC.



release rate. For SOI at -50 CAD, the local equivalence ratios are not close to stoichiometric, however, there is a strong radial stratification and a bit of angular stratification. As mentioned in the previous section, the radially asymmetric pattern can be caused by the in-cylinder tumble motion. This higher amount of stratification for case B, compared to case A, has lowered the peak heat release rate. A higher stratification level for SOI at -25 CAD (case C) has lowered even more the peak heat release rate, however, local fuel/air ratios are getting close to stoichiometric. For SOI -20 and -15 CAD, higher and higher stratification levels are achieved, but locally rich zones have changed the heat release rate behavior and increased the peak heat release rate as mentioned for case D' in the previous section.

Before discussing the spectroscopy results, it should be noted that these results were based on spectrally resolved line-of-sight information, integrated over a narrow strip in the combustion chamber (see the top left panel of Fig. 6.10), for a wavelength range from 270 to 540 nm. A post-processing method was applied to distinguish broadband chemiluminescence (probably due to larger, electronically excited, species) from thermal radiation (black body radiation: soot), and several specific chemiluminescing species were identified (see section 4.3). Crank-angle-resolved chemiluminescence intensities of different species are normalized by the total luminosity of the combustion cycle to study the role of each species in a cycle.

For the almost homogeneous combustion, case A (SOI at -200 CAD), broadband chemiluminescence is the dominant luminosity source and no thermal radiation is detected, as expected considering the locally lean regions. At the same time, since the fuel distribution is lean, local temperatures are low, resulting in almost no OH^* chemiluminescence. Broadband, CH^* and C_2^* chemiluminescence all follow exactly the temporal behavior of the main heat release rate (see Fig. 4.9a).

By moving towards stratified cases in the PPC regime, the role of broadband chemiluminescence in the total cycle luminosity drops, while the thermal radiation appears late in the combustion. There is no thermal radiation detected for case B, since there are no any locally rich regions for this case, but for the higher stratification levels (cases C-E), the thermal radiation appears. This is due to locally high equivalence ratios (> 1) that enhance the formation of soot [5]. Note that the relative magnitudes of thermal radiation curves are not necessarily

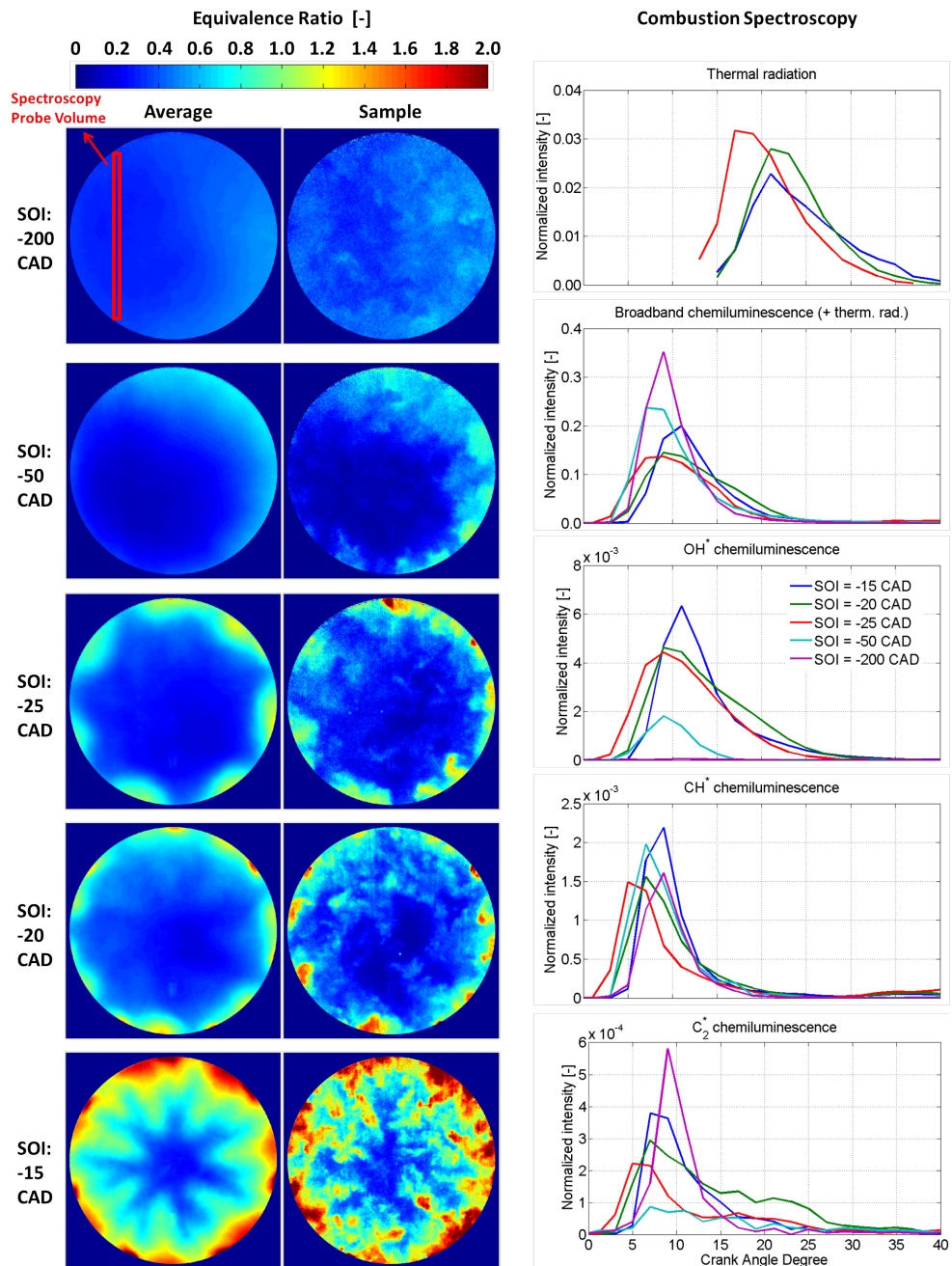


Figure 6.10: Fuel distributions at TDC (left) and species chemiluminescence intensities (right) for different injection timings (Table 4.2). Species chemiluminescence intensities are normalized by the total intensity of the combustion cycle to see the overall species behavior within a cycle. The legend in the center-right graph holds for all others as well.

representative of the relative magnitude of soot formation, since the thermal radiation is more dependent on the temperature than the soot density (Planck's distribution). Furthermore, the role of OH^* and C_2^* chemiluminescence intensity in the total luminosity of a cycle increases upon increasing fuel stratification. The exact chemical processes behind chemiluminescence are not sufficiently understood, particularly at elevated pressures [54, 65]. However this may be, the increase of OH^* and C_2^* chemiluminescence intensity can be interpreted as a result of higher temperature; locally higher equivalence ratios would produce higher combustion temperature. The contribution of CH^* chemiluminescence to the total cycle luminosity seems to be less sensitive to fuel stratification compared to all other species, although the integrated results of CH^* chemiluminescence still increases with increasing fuel stratification (see Fig. 4.8).

Spectroscopy results of the almost-HCCI case (case A) show that this case does not follow the general order of higher fuel stratification \Rightarrow larger contribution of C_2^* chemiluminescence to the total cycle luminosity, which holds for all PPC cases (case B-E) discussed above. The time-resolved C_2^* chemiluminescence intensity of case A exactly follows the main heat release rate, which has one of the highest peaks (Fig. 6.9). This can show a strong correlation between C_2^* formation and the main heat release rate in the HCCI regime. For PPC points, the C_2^* chemiluminescence intensities start in the early stage of combustion, during the breaking of big fuel molecules, and continues up to the time of main heat release rate. Still there is another chemical mechanism for C_2^* formation in this regime, at the late stage of combustion during formation of soot particles [69], which can be seen in Fig. 6.10 as well (a tail for highly stratified cases).

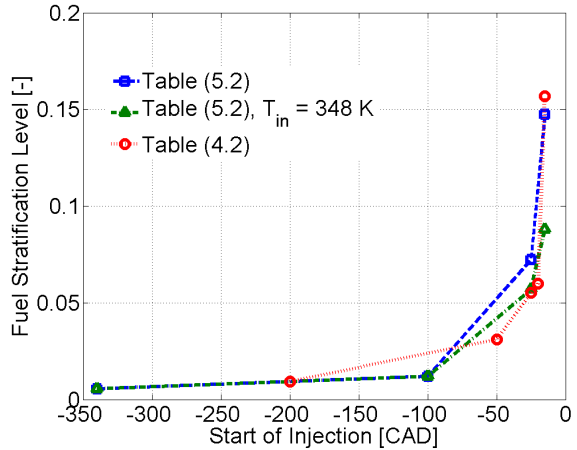
6.4.3 Fourier-based Stratification Analysis

A Fourier-based metric for combustion stratification was proposed in chapter 5, based on the spatial frequency domain of OH^* bandpass images. In this method, the stratification is defined as the signal energy of an intermediate spatial frequency range (E_A), normalized by the maximum signal energy (E_{max}) [82]. This same method is applied in this section to analyze the fuel stratification based on quantified results of fuel-tracer LIF. To evaluate the fuel stratification, exactly the same method and equations (see section 5.3.2) are used as for combustion stratification just by substituting "equivalence ratio" for "luminescence intensity". To determine the maximum signal energy, the maximum equivalence ratio is considered as 2 for all cases. Note that equivalence ratio has a global meaning, while the intensity does not, hence a global maximum equivalence ratio can be considered instead of local maximum intensities used for combustion stratification analysis.

Results of fuel stratification at TDC as a function of SOI are illustrated in Fig. 6.11 for different operating conditions (Table 5.2, Table 5.2 at a constant intake temperature, and Table 4.2). Although these results are based on different operating conditions, there is a unique and strong correlation between SOI and fuel stratification at TDC. These results confirm that ignition delay plays a significant role in the mixing process. Furthermore, this fuel stratification metric can be used as a tool to optimize the stratification in the PPC regime from different points of view, such as emissions, efficiency, heat release rate and controllability. For instance, it can be seen from the previous section that stratification lower than 0.035 will be accompanied by the absence of

thermal radiation (soot formation), or that a fuel stratification level higher than 0.1 will result in a high peak heat release rate. This optimization of fuel stratification based on this new metric can also be implemented when using double and triple injection strategies to improve control over the mixing.

Figure 6.11: Fourier-based fuel stratification level at TDC as a function of SOI for different operating conditions (Table 5.2, Table 5.2 at a constant intake temperature and Table 4.2). There is a strong correlation between fuel stratification and combustion stratification which can be seen by comparing this figure to Fig. 5.13.



6.4.4 Effects of Intake Temperature on Fuel Stratification

This section on the effect of intake temperature on fuel stratification is based on only few experimental points investigated in this study, and the results should be taken as preliminary; further investigation is highly recommended.

To see the effect of intake temperature, cases C' and D' (Table 5.2), with intake temperatures of 368 and 398 K, respectively, are repeated with an intake temperature of 348 K, without changing any other parameter. Fuel molar density distribution and its average as a function of radius are presented in Fig. 6.12 for an average of 100 cycles. Results are presented based on fuel molar density to see the fuel distribution independent of oxygen percentage or the intake density. For the present cases, the fuel stratification can better be seen when angularly averaged fuel densities are plotted as a function of radius. For a homogeneous case a horizontal line is expected, as was the case for case A' in Fig. 6.6. When the temperature is reduced, the fuel density as a function of radius becomes more constant, meaning that close to the center of combustion chamber the mean fuel density increases compared to the higher temperature case, while it decreases by moving away from the center, again compared to the higher temperature. Results of Fourier-based stratification analysis, presented in Fig. 6.11, also show that the lower intake temperature for cases C' and D' (Table 5.2, $T_{in} = 348$ K) has resulted in lower fuel stratification level for these cases.

The lower fuel stratification for lower temperature can be explained considering two facts. First, at a lower intake temperature, the gas density is higher (since the intake pressure is kept constant), resulting in a larger cone angle [83] which can improve mixing. Secondly, lower temperature will result in lower viscosity (in gas phase) which increases the turbulence level

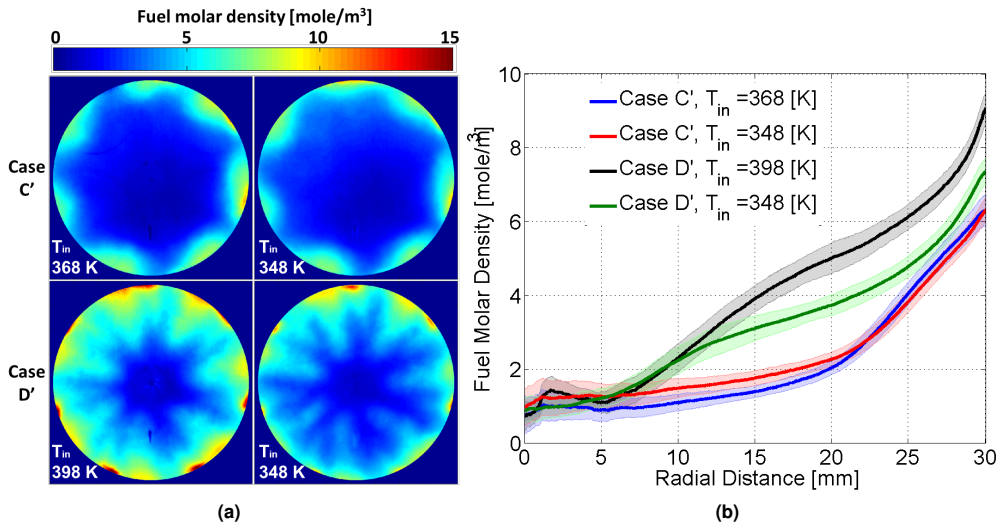


Figure 6.12: Mean fuel molar density distribution (a) and its average as a function of radius (b) for cases C' and D' (Table 5.2) at different intake temperatures.

(Reynolds number) and consequently the mixing efficiency [84]. Note that the field of view is limited in this study and the remaining area, which is out of FOV, might show different behavior. It might have happened that more fuel is beyond the FOV for lower temperatures, caused by increased spray penetration (the lower the gas temperature, the larger the liquid length [85]). Hence, it is recommended to study the effects of intake temperature on mixing process more in deep.

6.5 Conclusions

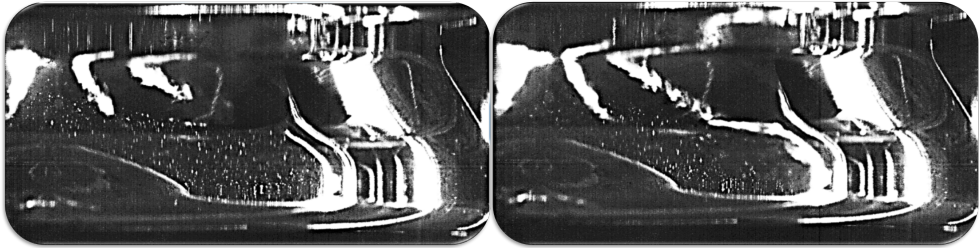
The objective of this study was to measure the fuel density distributions at different fuel stratification levels and to investigate the effect of fuel stratification level on combustion and heat release rate behavior. Fuel-tracer LIF measurements were performed in a light-duty optical engine in a horizontal planar cross-section at the middle of combustion chamber at TDC. Quantified results of the fuel distribution were obtained by measuring the temperature dependency of the toluene fluorescence signal and implementing a thermodynamic model. Results of fuel distributions were compared to the results of high-speed OH* bandpass imaging and the high-speed spectroscopy to investigate the effects of fuel stratification on ignition, combustion, thermal radiation and various chemiluminescing species. The following is concluded based on our results:

- Fuel stratification can either decrease or increase the peak heat release rate, depending on the stratification pattern and the values of equivalence ratio.
- In the nearly homogeneous regimes, small inhomogeneities or mild gradients in fuel

distribution are the main parameters affecting the heat release rate.

- In the PPC regime, the angular stratification plays a significant role to diminish the peak heat release rate, however, high local equivalence ratios (close to one and higher) should be avoided, e.g. by enhancing the mixing efficiency.
- Thermal radiation in the PPC regime can be zero if high local equivalence ratios (> 1) are avoided.
- The role of OH^* chemiluminescence intensity in combustion luminosity increases with the level of fuel stratification, and is essentially absent in HCCI conditions.
- Fourier-based analysis of fuel distribution can provide an objective metric for fuel stratification. Results show the fuel stratification at TDC strongly correlates with start of injection.

Turbulence and Stratification



This chapter is based on the following publications:

Izadi Najafabadi, M., Tanov, S., Wang, H., Somers, B., Johansson, B., Dam, N., (2017) **“Effects of Injection Timing on Fluid Flow Characteristics of Partially Premixed Combustion Based on High-Speed Particle Image Velocimetry”**, *SAE International Journal of Engines*, 10(4), doi:10.4271/2017-01-0744.

Wang, H., Tanov, S., Izadi Najafabadi, M., Wang, Z., Johansson, B., (2016) **“Time-resolved in-cylinder PIV measurement in a light duty optical engine under PPC conditions”**, *Lisbon 2016 International Symposium on the Application of Laser and Imaging Techniques to Fluid Mechanics*.

Tanov, S., Johansson, B., Izadi Najafabadi, M., Wang, H., (2016) **“Analyzing of In-Cylinder Flow Structures and Cyclic Variations of Partially Premixed Combustion in a Light Duty Engine”**, *FISITA 2016 World Automotive Congress*, F2016-ESYF-005.

7.1 Introduction

Very low NO_x and soot emissions coupled with high efficiency have made PPC an attractive research topic for CI combustion [5, 86, 87]. The long ignition delay of PPC (compared with conventional diesel combustion), achieved by using gasoline-like fuels and Exhaust Gas Recirculation (EGR), increases the level of premixing and prevents the persistence of locally rich zones during combustion, resulting in low soot formation, and low temperature combustion, leading to less NO_x formation [88–90].

PPC provides better controllability compared to HCCI due to higher levels of mixture stratification (spatial inhomogeneities). This level of mixture inhomogeneity, adjustable by injection timing and injection strategy, can be used as a tool to control combustion phasing [21, 91]. The mixing process is mainly governed by the injection process and is highly dependent on flow and turbulence from start of injection (SOI) till start of combustion (SOC) [92]. The outcome of this process determines the ignition timing and the combustion duration, the most important parameters to be controlled. Hence, in order to better understand mixture formation in PPC, investigating the flow structure and turbulence from injection up to combustion is an essential milestone.

Flow field measurements have been carried out in optical engines for a single point, a two-dimensional plane or a three-dimensional volume, depending on the purpose of the research. Laser Doppler Anemometry (LDA) uses the Doppler shift of scattered laser light to determine the velocity at a single point, and is implemented in optical engines to measure velocity vectors at critical points, like the spark plug area in SI engines or the piston bowl area in Diesel engines [93–95]. Particle Image Velocimetry (PIV) can be applied in an optical engine as a non-intrusive laser diagnostic technique to measure flow fields in a two-dimensional plane [92, 96–98]. In this technique, a pair of images is captured over a short time interval of Mie scattered light off seeding particles which should be chosen such that they faithfully follow the flow. Velocity vector fields can later be calculated from particle displacements in the image pairs. The PIV technique can also be used for three-dimensional measurements, so-called Tomo PIV, which needs two, three or four cameras depending on the number of velocity components to be measured and the seeding density [99].

To investigate the mixing process inside the combustion chamber, single-point measurements do not provide sufficient spatial information. Three dimensional measurements (Tomo PIV), on the other hand, are significantly more expensive and time costly (from a post-processing point of view). Two-dimensional PIV can still provide global information about the mixing process if a proper plane is chosen, while it is not too expensive and much less time consuming for post-processing compared with 3D PIV. Hence, high-speed 2D PIV is employed in this study to investigate the flow and turbulence structures during mixing and combustion.

For PPC regimes, PIV has been used to measure the 2D in-cylinder flow structures [92, 96–98, 100]. One of the first studies was conducted by Miles et al. [96], who measured vertical plane velocity fields inside the piston bowl and the squish region of a light duty (LD) optical engine (Volvo D5). They describe the bulk flow structures, and investigate the mixing process

and the formation of emissions. The measured velocity fields also indicate the locations of heat release [97]. However, their PIV measurements were carried out with a low repetition rate (10 Hz). Consequently, the turbulence behavior, as an important parameter which affects the mixing process, was not measured in itself (mixed with cycle-to-cycle variations). High-speed PIV gives the opportunity to measure cycle-resolved turbulence. One of the first high-speed PIV measurements (3 kHz) of the PPC mixing process was performed by Zegers et al. [98], who studied flow structure in a horizontal plane close to the cylinder head of a heavy-duty (HD) optical engine. Their measurements concerned non-reactive conditions to see the effects of injection timings and strategies on the flow field. High-speed PIV was recently implemented by Wang et al. [92] and Tanov et al. [100] in a Volvo D5 optical engine for both non-reactive and reactive conditions, respectively, for different injection strategies. Their measurements were carried out for every 2 CAD (2.4 kHz) which resulted in a relatively long time scale for extraction of cycle-resolved turbulence.

In the present research, the resolution of the PIV system corresponds to 1 CAD, to reduce the time scale of measurements and to improve results on cycle-resolved turbulence. Both non-reactive and reactive conditions are studied to better understand injection, mixing, ignition and combustion phenomena for various injection timings. Using skip-fire mode for experiments (one fire per five cycles) allows to compare each fired cycle with its previous motored one. This provided a normalization option to compare results of, for example, different intake temperatures which have different turbulence levels. Furthermore, for the first time, PIV results for 5-hole and 7-hole injectors have been compared to investigate their effect on flow, turbulence and heat release behavior of PPC combustion.

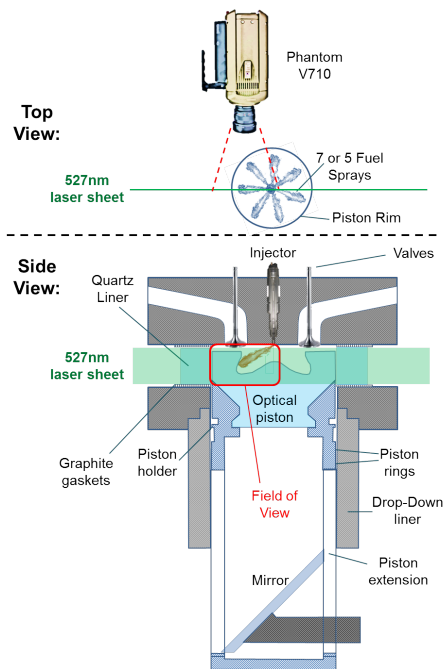
Experiments are performed at Lund University on a VOLVO D5 light-duty optical engine, identical to the one used for the work presented in previous chapters (at Eindhoven University of Technology). Operating conditions of this study are also similar to those earlier experiments (chapters 3-6). The results presented in this chapter are mostly from Ref [84], derived from the same experimental campaign as the publications by Wang et al. [101] and Tanov et al. [102].

7.2 PIV Setup

Details of the optical engine and general operating conditions used for this study are already discussed in section 2.7. Figure 7.1 shows the high-speed PIV setup used for our measurements. The aim is to measure fluid velocity in a vertical planar cross-section through the centerline of one of the fuel sprays to study the injection-driven turbulence and flow characteristics during air/fuel mixing. Titanium dioxide (TiO_2) powder with an average particle diameter of 2-3 μm and a density of 4260 kg/m^3 is used as PIV seeding. Assuming Stokes flow, the time constant (t_0) characterizing the ability of these particles to follow flow velocity changes is about 30 μs at TDC thermodynamic conditions (a pressure of 35 bar and a temperature of 900 K). This is smaller than the estimated Kolmogorov time scale, so our seeding particles should be able to follow the flow and turbulence quite well. The TiO_2 powder has been baked for 24 h before experiments to avoid particle agglomeration, and is supplied from a cylindrical container fed by a swirling airflow to make a homogeneous air-seeding mixture. The seeding stream is controlled by a

mass flow meter before mixing with air-EGR at the intake manifold.

Figure 7.1: Schematic of high-speed PIV setup. A double-pulse vertical light sheet at 527 nm with an interval of $15\ \mu\text{s}$ passes through the combustion chamber, at the center line of one of sprays, every crank angle degree. Image pairs of illuminated TiO_2 particles (seeded at the intake air) are captured from side view using the high-speed camera. The field of view is limited to half of the piston bowl as shown in the figure (red color).



A commercial diode-pumped double-cavity Nd:YLF high-speed laser (DualPower 30-1000, $\lambda = 527\ \text{nm}$) is used as PIV light source. The laser is synchronized with the crankshaft encoder to fire a double-pulse light sheet every crank angle degree (4.8 kHz) with an interval of $15\ \mu\text{s}$. A light sheet optics unit is used to provide a diverging light sheet with a height of 25 mm (same height as the optical liner). The light sheet passes immediately below the injector tip with a thickness less than 1 mm. The energy of each laser pulse after all mirrors and optics (just before passing through the engine liner) is 13 mJ.

A high-speed Phantom V710 CMOS camera is used to capture image pairs from side view every crank angle degree. Table 7.1 shows specifications of the imaging system. Each exposure time comprises one of the laser pulses; a little more time for the second exposure to allow the camera to finalize recording of the first exposure. The field of view is limited to only one side of the piston bowl because of the symmetric geometry of the combustion chamber (see Fig. 7.1).

Imaging the squish region and the piston bowl simultaneously was not feasible. Hence, another set of experiments was performed to capture the flow structure in the squish region, under nominally the same experimental conditions. Flow fields from the piston bowl and the squish region are merged to each other whenever needed. Piston bowl measurements are performed from -30 to $30\ \text{CAD}$ (ATDC), while squish region measurements are performed from -45 to $45\ \text{CAD}$. Capturing the narrow squish region from -20 to $20\ \text{CAD}$ was not possible due to low laser power close to the cylinder head (affected by piston reflection as well) and insufficient resolution of the images in that small region.

Table 7.1: Specifications of the imaging system.

Camera	Phantom V710
Imaging sensor	8 bit CMOS
Resolution	976 × 640 pixel ²
Frame rate	4800 pairs/s
Exposure time of 1 st frame	87 μs
Exposure time of 2 nd frame	120 μs
Objective lens	AF Nikkor, $f = 105$ mm, visible-light
Aperture	$f/16$

7.2.1 Operating Conditions

The general operating conditions are explained in sections 2.6 and 2.7. The engine is motored at 800 rpm, based on a skip-fire mode (one fire per five cycles). To investigate the effect of SOI on flow characteristics of Partially Premixed Combustion, SOI is swept from -60 to -15 CAD (ATDC) for two different injectors (5- and 7-hole). The operating conditions are detailed in Table 7.2. The injection durations are 2.5 and 2.6 CAD for 5-hole and 7-hole injectors, respectively, to inject the same amount of fuel (12.4 mg/cycle) at a pressure of 850 bar. Hence, the accumulated heat release is representative for the combustion efficiency of these experimental points as represented in Table 7.2. Intake temperature is tuned to keep the CA50 constant (7.0 ± 0.8 CAD ATDC), while the intake oxygen is kept constant at 20 vol. %.

Table 7.2: Different injection timings and intake temperatures.

5-hole Injector (orifice diameter: 159 μm)				
SOI [CAD]	Intake Tem- perature [K]	SOC (CA05) [CAD]	CA50 [CAD]	Accumulated heat release [J/cycle]
-60.0	423	-3.0	6.4	206.1
-25.0	393	-0.8	7.3	276.2
-22.5	368	-0.5	6.3	343.5
-20.0	363	1.0	7.7	373.4
-17.5	383	1.5	7.3	385.4
-15.0	411	2.1	6.8	381.1
7-hole Injector (orifice diameter: 140 μm)				
-60.0	403	-2.5	7.6	240.9
-25.0	363	-1.0	7.6	319.7
-22.5	353	-0.5	7.1	372.9
-20.0	343	0.2	6.5	421.3
-17.5	353	1.4	7.3	424.2
-15.0	383	2.1	7.2	420.8

7.3 PIV Post-Processing

7.3.1 Image Distortion and Adaptive PIV

Image distortion, caused by the re-entrant piston bowl geometry, has considerable effects on PIV results, and needs to be corrected for. The dewarping procedure includes imaging a reference target with and without distortion. Based on these two images, a local weighted-mean algorithm is implemented in Matlab to correct all images. Fig. 7.2 shows the reference target image with distortion and after distortion correction. In this study, a dot target was used, with uniformly located dot markers ($1\text{ mm} \times 1\text{ mm}$) on its surface.

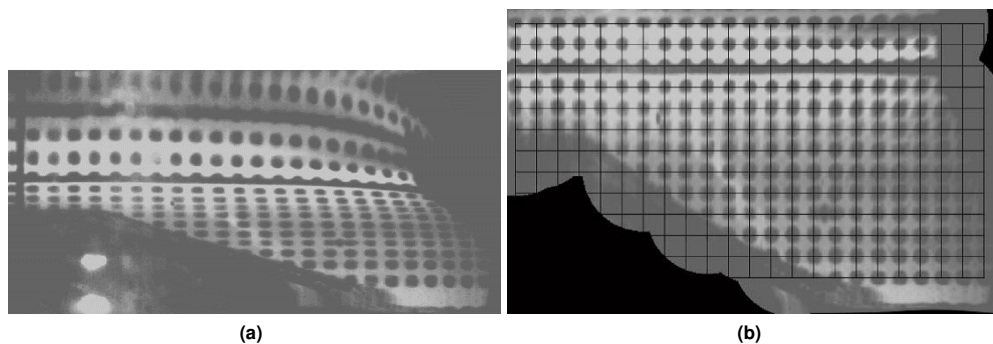


Figure 7.2: Dot target image: (a) raw image before distortion correction; (b) after distortion correction. All PIV images are dewarped in the same way before post-processing.

The commercial PIV software of Dantec Dynamics is used for post-processing of dewarped PIV images based on an adaptive PIV method. This method could iteratively adjust size, shape and orientation of Integrative Area (IA) to cover a wider range of particle movements. The IA size is adjusted from 8×8 pixels to 64×64 pixels for our measurements. This adaption is beneficial for PIV measurements in engine conditions with direct injection which includes a wide range of velocities. During injection, fuel droplets of the spray will also scatter the light, so that they, too, can act as seeding particles and are useful for calculation of PIV vectors in those regions to achieve the flow field of the spray [92].

7.3.2 Ensemble Average Velocity and Cycle-resolved Turbulence

Ensemble averages of flow fields will provide the overall behavior of in-cylinder flow and would be the first step to understand the mixing process and combustion. In this study, 43 fired cycles are measured for each experimental operating condition. The ensemble average of any velocity component at a given time and location, \bar{U}_{EA} , is calculated from:

$$\bar{U}_{EA}(\theta) = \frac{1}{N} \sum_{i=1}^N U(\theta, i) \quad (7.1)$$

where U is one of the two instantaneous velocity components, θ is the crank angle degree, i is the cycle index and N is the number of cycles (that is, $N = 43$ in this case).

In order to assess the fluctuations in the flow field, we need to extract a measure for the turbulence from the PIV images. A parameter that is often used to this end is the rms value of velocity fluctuations, derived from a preferably large number of instantaneous velocity field realizations. In our case, however, this is not an attractive idea, because of the occurrence of cycle-to-cycle variations between individual engine strokes, that also affect the mean flow (relative to which the velocity fluctuations would be defined). We would prefer to use a measure for turbulence within each individual cycle. The high-speed PIV sequences should in principle allow that, a prerequisite being that a mean flow field can be derived. This is not a trivial issue, the more so because we cannot evaluate the out-of-plane velocities. A pragmatic approach is followed here, based on variations in the velocity field over a few crank angles [92, 100]:

$$u'(\theta, i) = \sqrt{\frac{1}{M} \sum_{j=1}^M [U(\theta + \frac{2j - M - 1}{2} \Delta\theta, i) - \bar{U}(\theta, i)]^2} \quad (7.2)$$

where u' is the cycle-resolved fluctuating velocity component, at crank angle θ and cycle index i . $\Delta\theta$ is the CAD step size (1 CAD for our measurements), and M is the total number of crank angle degrees in the considered time window. In our study M equals five, implying that, for any θ , the velocity fields of five CADs are considered, i.e. $\theta + l \cdot \Delta\theta$ with $l = -2, -1, 0, 1, 2$. The mean velocity at the center CAD is calculated from:

$$\bar{U}(\theta, i) = \frac{1}{M} \sum_{j=1}^M C(j) U(\theta + \frac{2j - M - 1}{2} \Delta\theta, i) \quad (7.3)$$

where $C(j)$ is a sine weight factor:

$$C(j) = \frac{\sin(\frac{j}{M+1}\pi)}{\sum_{j=1}^M \sin(\frac{j}{M+1}\pi)} \quad j = 1, 2, \dots, M. \quad (7.4)$$

Obviously, $\sum_{j=1}^M C(j) = 1$.

Our measure for turbulence is essentially the rms-value of the velocity changes over a few crank angles. We realize the shortcomings of this parameter, for instance its being sensitive to the structure of the out-of-plane flow field, but expect it to at least scale with the real amount of turbulence present in the instantaneous flow field. In our study, M equals five since the

time scale of the phenomena in the engine operating conditions cannot be bigger than a few crank angle degrees. The absolute fluctuating velocity at a given time and location ($U'(\theta, i)$) is calculated from the square root of the sum of the squares of the fluctuating velocity components:

$$U'(\theta, i) = \sqrt{u'_x(\theta, i)^2 + u'_y(\theta, i)^2} \quad (7.5)$$

where $u'_x(\theta, i)$ and $u'_y(\theta, i)$ are fluctuating velocity components calculated from Eq. (7.2). The fluctuating velocity at a given CAD is determined later by averaging the absolute fluctuating velocities of all positions in the piston bowl and all cycles.

For presenting turbulence results, the fluctuating velocity (Eq. (7.5)) at a given CAD is normalized by the mean fluctuating velocity of the previous motoring cycle from -30 to 30 CAD. This is called the turbulence level. Motoring measurements are performed based on the skip-fire mode, meaning that for each fire cycle, the PIV images of the previous motoring cycles are recorded as well. This normalization method allows to compare turbulence levels of different operating conditions with different intake temperatures (Table 7.2). The same averaging and normalization method is used to calculate the normalized velocity at a given CAD.

7.4 Results and Discussion

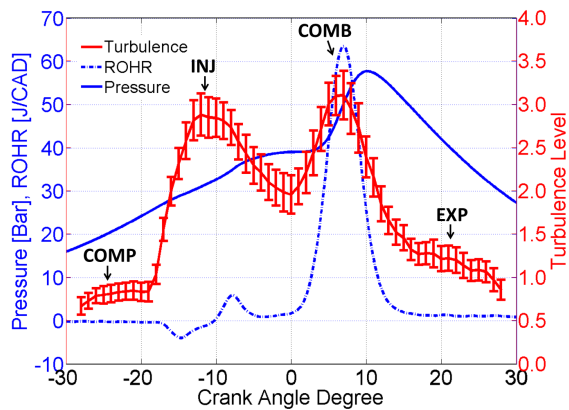
PIV measurements are processed in combination with heat release analysis of pressure traces to study effects of flow characteristics on mixing and combustion behavior. Turbulence has a significant effect on mixing, ignition timing and duration of PPC. Hence, turbulence is the main focus of this chapter. In this section, the flow field of PPC is discussed first. Next, effects of injection timing on flow and heat release characteristics are investigated. Reactive and non-reactive cases are compared, and finally, differences between 5-hole and 7-hole injectors are examined.

7.4.1 Flow Characteristics of PPC: from SOI to End of Combustion

Typical curves for pressure, rate of heat release and turbulence level of PPC combustion are illustrated in Fig. 7.3 (SOI: -17.5 CAD, 7-hole injector). The magnitude of the error bars is similar in other experimental results. Hence, for the sake of clarity, they are not included in the following graphs.

Various phenomena which affect flow characteristics in the combustion chamber occur from -30 to 30 CAD, including compression, injection, mixing during the ignition delay, combustion and expansion. Each step is detailed below in combination with the velocity fields shown in Fig. 7.4. There is a small area close to the piston bowl rim in which the laser sheet was reflected, causing unreliable PIV data. That is the reason velocity vectors are absent in this region in Fig. 7.4.

Figure 7.3: Characteristic time development of pressure trace, rate of heat release (ROHR) and turbulence level in PPC for injection timing at -17.5 CAD ATDC using a 7-hole injector. The labeled arrows indicate the phases discussed in the text (COMP: compression, INJ: injection, COMB: combustion, and EXP: expansion).



Compression: By approaching TDC from -30 CAD, the flow is mainly governed by upward piston motion and the flow velocity decreases as the piston velocity decreases. This is clearly visible in Fig. 7.4 by comparing velocity directions and magnitudes at -26 and -18 CAD. However, the turbulence level is increasing upon approaching TDC (see Fig. 7.3). The upward motion of the piston compresses the flow in the squish region and pushes it into the piston bowl. The interaction of this squish flow with swirl motion enhances the turbulence level in the combustion chamber [92].

Injection: There is a little hydraulic delay causing the spray to reach the piston bowl at -16 CAD for SOI of -17.5 CAD ATDC (see Fig. 7.4). The flow field at -16 CAD shows that the spray penetrates the piston bowl and at -15 CAD the spray has stabilized and caused a clockwise vortex, governed by the piston bowl geometry. Another significant flow structure which is created during injection is air entrainment, large upward vectors below the injector tip especially at the beginning of the injection. This air entrainment behavior is exactly similar to that seen and discussed by Zegers et al. [98]. The spray velocity is higher than the piston velocity and the mean velocity in the combustion chamber. Hence, the mean velocity (in the chosen PIV plane) dramatically increases by the injection. It also effects the turbulence level within the combustion chamber, increasing it by a factor of 2 to 4 (depending on the injection timing).

Ignition delay: The vortex inside the piston bowl, driven by the spray, persists during ignition delay. By approaching TDC, the flow in the squish region is pushed into the piston bowl, supporting the clockwise vortex [92, 95, 97, 100]. This vortex structure improves the mixing process, even though turbulence level and mean velocity decrease after the end of injection (see Figs. 7.3 and 7.4). The (out-of-plane) swirl motion can also cause a velocity and turbulence drop in the observation plane [103]. However, different decreasing rates of velocity and turbulence level shown in Figures 7.6 and 7.7 for different injection timings prove that this decrease cannot be only caused by the swirl motion since the swirl ratio was the same for all cases. This velocity and turbulence drop decreases the mixing efficiency until the start of combustion.

Combustion: Strong turbulence during combustion and auto-ignition causes random behavior in the flow field inside the piston bowl. Hence, the mean flow field does not show a clear flow structure. Comparing flow fields at 6 and 7 CAD indicates that high mean velocity regions

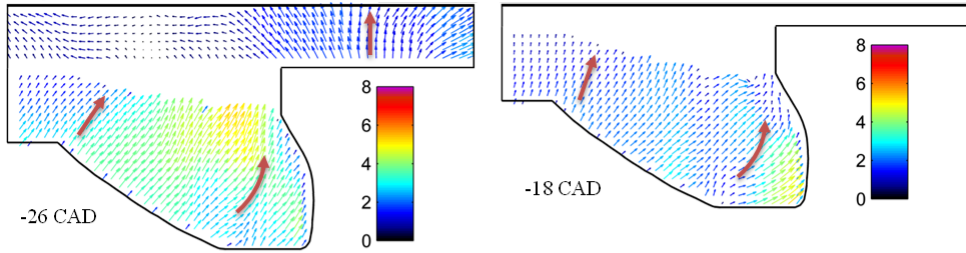
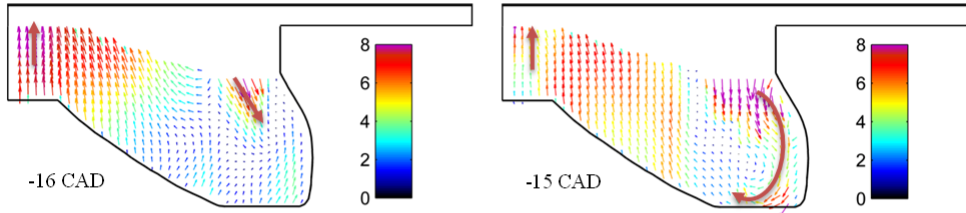
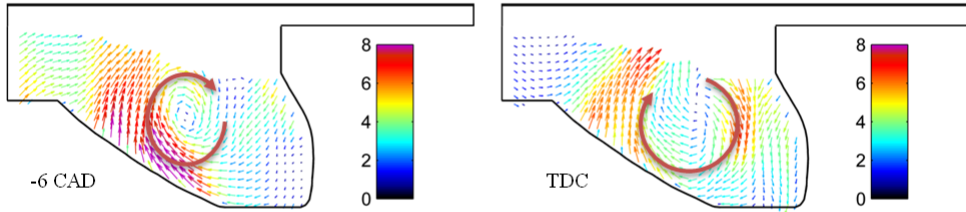
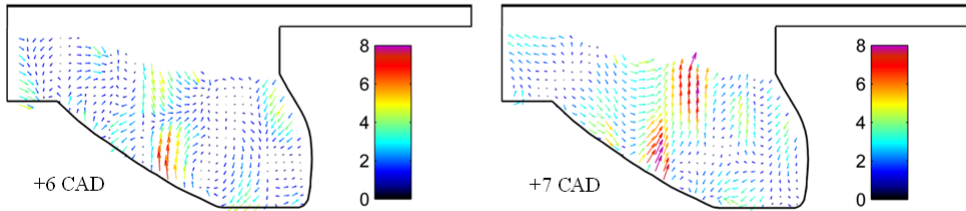
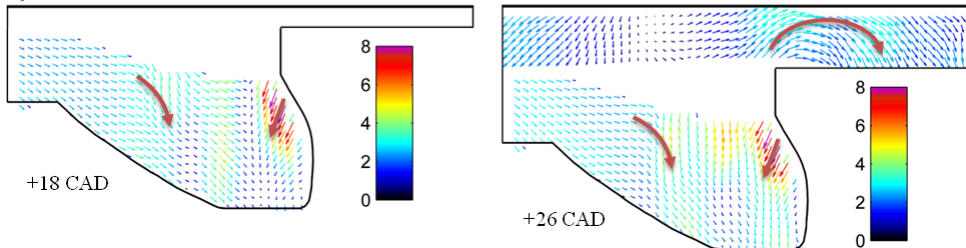
Compression:**Injection:****Approaching TDC:****Combustion:****Expansion:**

Figure 7.4: Mean flow field at different crank angle degrees for SOI at -17.5 CAD ATDC using the 7-hole injector (units in m s^{-1}). Red arrows indicate the overall flow behaviors.

move through the piston bowl, showing the motion of the combustion region [92, 100]. Mean velocity and turbulence levels during combustion follow the heat release rate quite well, in other words, an increase in the rate of heat release is followed by an increase of mean velocity and turbulence level and vice versa.

Expansion: After the end of combustion, the flow is again governed by piston motion, and the mean velocity increases as the piston velocity increases. The inner wall of the piston bowl at the right side has the highest effect on the flow field, by trapping and pushing the flow downward (Fig. 7.4). By the expansion of the squish region, flow goes from the piston bowl into the squish region (see Fig. 7.4 at 26 CAD) [92, 95, 97, 100].

7.4.2 Effects of Injection Timing

Injection timing is one of the main factors to control combustion phasing and the smoothness of heat release rate. Ignition delay (= mixing time) depends on the injection timing, and the amount of combustion stratification is governed by that. In this study, the combustion phasing is kept constant at 7 ± 0.7 CAD ATDC, meaning that later injection causes less mixing time (ignition delay). The mixing process from SOI until -3 CAD (minimum SOC for all cases) is not affected by combustion, and can be investigated from a mixing efficiency point of view. Experimental results presented in this section are obtained with a 7-hole injector and based on operating conditions mentioned in Table. 7.2.

Figure 7.5: Heat release rate for different injection timings using 7-hole injector. Combustion phasing is kept constant at 7 ± 0.7 CAD ATDC by tuning the intake temperature (see Table 7.2). Minimum SOC for all cases is at -3 CAD ATDC.

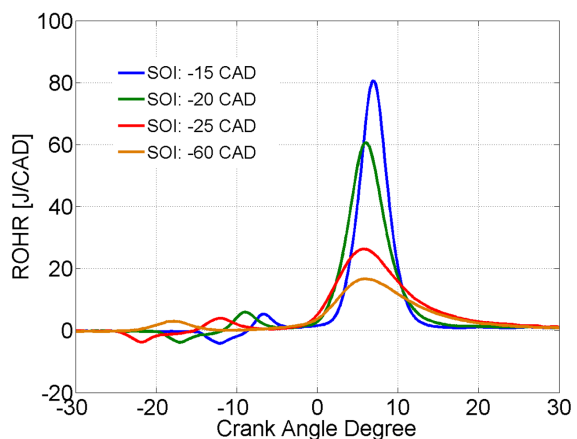


Figure 7.5 shows the heat release rate behavior for 4 different injection timings between -60 and -15 CAD ATDC. There are three main parameters affecting the smoothness of heat release rate: mixture temperature, mixture homogeneity and the turbulence level at SOC. From Table 7.2 it follows that the intake temperature for SOI -15 CAD is 40 K higher than that for SOI -20 CAD, causing a higher peak heat release rate in the former case. Less mixing time for SOI -15 CAD compared to all other points can increase the mixture stratification and induce local equivalence ratios closer to stoichiometry, resulting in the highest peak heat release rate as discussed in chapter 6. The relatively high turbulence level can also speed up the combustion

process resulting in the highest peak heat release rate as will be discussed in detail in the next section. However, comparing intake temperatures of SOI -20 CAD (343 K) with SOI -25 and -60 CAD (363 and 403 K, respectively) does not explain the smoothness of ROHR for these cases, as the higher intake temperature has nevertheless led to lower peak heat release rate. Hence, mixture homogeneity and turbulence are the main controlling factors of ROHR behavior in our experiments. It should be mentioned that the experiment with SOI -60 CAD has lower combustion efficiency (see Table 7.2), attributable to a large amount of fuel trapped in the crevice volumes (as discussed in chapter 3).

Mixture stratification is mainly governed by ignition delay (available time to mix) and mixing efficiency. Increased mixing duration provides more homogeneity if the mixing efficiencies would be similar for all cases. In principle, stronger turbulence will increase mixing. This can now be studied with the PIV results of velocity and turbulence level. Figures 7.6 and 7.7 demonstrate mean velocity and turbulence level as a function of crank angle for different injection timings.

Figure 7.6: Normalized velocity versus crank angle degrees for different injection timings using 7-hole injector. The normalization is based on the mean velocity (over time and space) of the previous motoring cycle from -30 - 30 CAD. Normalized velocity of a motoring case is also shown as a reference.

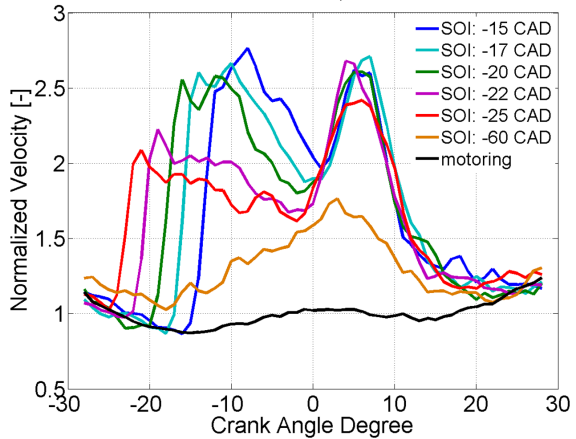
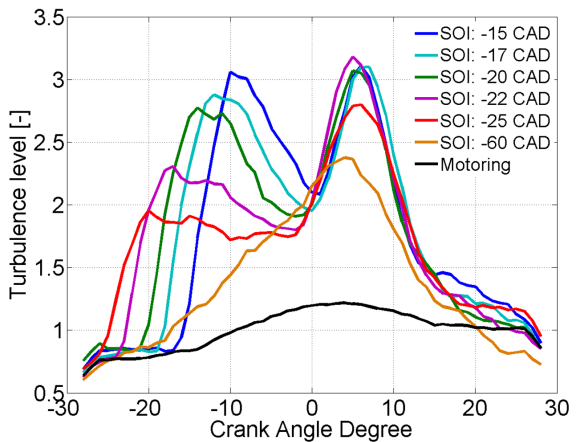


Figure 7.7: Mean turbulence level (over space) versus crank angle degrees for different injection timings using 7-hole injector. The turbulence level is defined as the fluctuating velocity (Eq. (7.5)) at a given CAD, normalized by the mean fluctuating velocity of the previous motoring cycle from -30 to 30 CAD. Turbulence level of a motoring case is also shown as a reference.



These results show that later injection leads to higher mean velocity and turbulence level inside

the piston bowl. This behavior is probably caused by the geometry and the position of the piston bowl relative to the spray targeting. The decay rates of mean velocity and turbulence level after the end of injection are also higher for later injections. Nevertheless, higher turbulence levels are achieved at SOC for later injections, speeding up the combustion process. On the other hand, the mixing efficiency would be higher for later injections based on the higher velocities and turbulence levels, which would be a trade off with mixing duration to affect mixture homogeneity. Based on our operating conditions, effects of mixing duration and the turbulence level at SOC seem to overcome the effects of mixing efficiency on charge stratification, since steeper heat release rates are achieved for later injections with shorter ignition delays. Results presented in chapter 3 shows that combustion stratification drops upon retarding the SOI from -25 to -15 CAD ATDC for similar operating conditions (see Fig. 3.15). In those experiments CA50 was not kept constant and these different injection timings had almost the same ignition delays and intake temperatures. Hence, the only parameter affecting the combustion homogeneity was mixing efficiency, which can be explained by these PIV results, proving higher mixing efficiencies by later injections.

In contrast with the low velocity magnitudes of the mean flow field shown in Fig. 7.4 at 6 and 7 CAD (around CA50), the mean velocity magnitudes derived from individual cycles show a significant increase during combustion (see Fig. 7.6). Velocity vectors of individual cycles during auto-ignition are large and directionally unstructured. Hence, their mean magnitudes are large while the mean flow field (average of velocity vectors over 43 cycles) shows small velocity vectors.

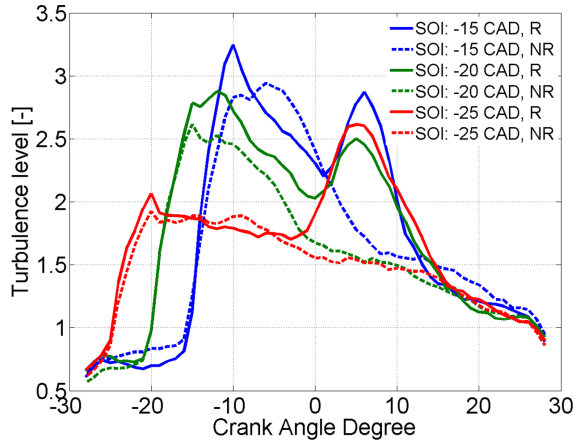
For SOI -60 CAD, the turbulence and velocity behaviors inside the piston bowl were not accessible during injection. As expected, the flow field does not show any spray-related features, and we will omit the results for this SOI-case in the remainder.

7.4.3 Injection-Driven vs Combustion-Driven Turbulence

Comparing flows for reactive and non-reactive operating conditions (20 and 0 vol. % oxygen, respectively) allows to distinguish between injection-driven and combustion-driven flow characteristics. Figure 7.8 compares the turbulence level of reactive and non-reactive cycles for three different injection timings using a 5-hole injector. Clearly, the second bump (between 0-10 CAD) in the turbulence level is combustion-driven turbulence which is absent in non-reactive cycles.

The combustion-driven increase in turbulence level can be estimated by subtraction of the non-reactive turbulence level from the reactive one from TDC to 30 CAD where the combustion has ended. Injection-driven turbulence level, on the other hand, can be determined by subtraction of motoring turbulence level from the fired one up to TDC (start of combustion). TDC is chosen as a reference point for separation of combustion from mixing, since the average CA05 for our experiments is at TDC. The injection-driven turbulence level at SOC is determined by averaging of the injection-driven turbulence level from -5 CAD to TDC. Figure 7.9a shows the injection-driven turbulence level at SOC as a function of injection timing. Obviously, by retarding the injection, the injection-driven turbulence level at SOC is linearly increasing. Figure 7.9b demonstrates a linear decrease of combustion-driven turbulence level by later

Figure 7.8: Comparison of reactive (R) and non-reactive (NR) turbulence level behaviors for different injection timings using 5-hole injector. Operating conditions of reactive and non-reactive cases are exactly the same, except for oxygen percentage (20 and 0 vol. %, respectively).



injection. Note that the maximum combustion-driven turbulence level does not change much for different injection timings (see Figs. 7.6 and 7.8). However, the duration of combustion has a considerable effect on the mean combustion-driven turbulence level which is averaged from TDC to 30 CAD.

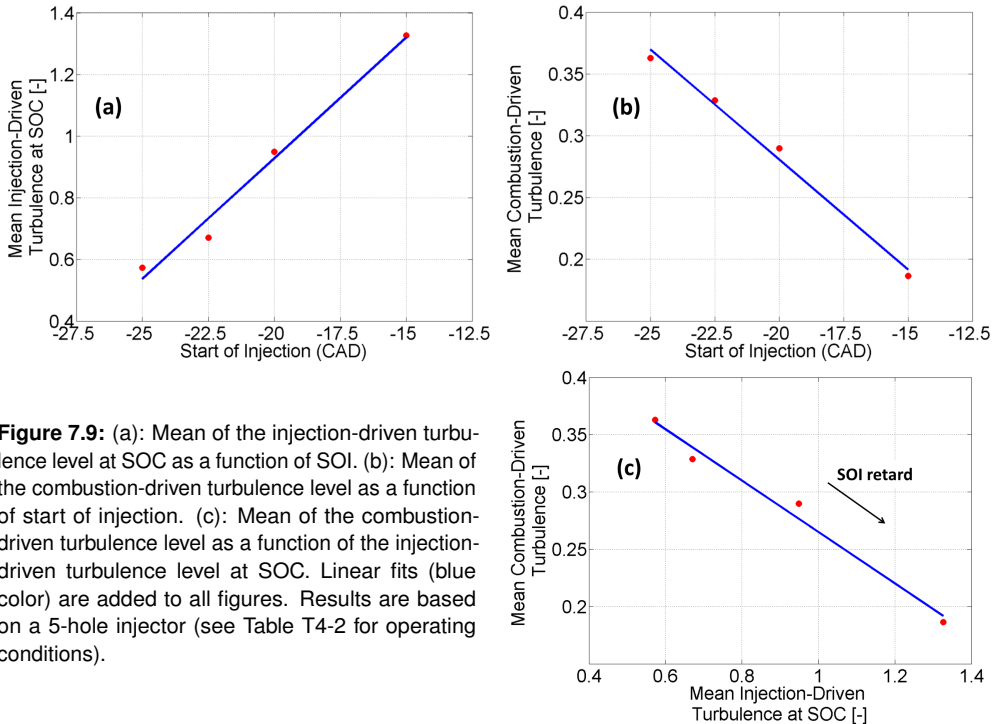


Figure 7.9: (a): Mean of the injection-driven turbulence level at SOC as a function of SOI. (b): Mean of the combustion-driven turbulence level as a function of start of injection. (c): Mean of the combustion-driven turbulence level as a function of the injection-driven turbulence level at SOC. Linear fits (blue color) are added to all figures. Results are based on a 5-hole injector (see Table T4-2 for operating conditions).

The mean combustion-driven turbulence level as a function of the injection-driven turbulence level at SOC is shown in Fig. 7.9c; obviously, they are linearly related as well. Higher injection-driven turbulence level at start of combustion would speed up the combustion process [104] and consequently the mean combustion-driven turbulence level decreases linearly. Note that the effect of swirl motion is not seen in our measurements, meaning that the center of the combustion cloud during the main heat release is not within the spray cross-section plane which we have measured. Hence, we recommend using volumetric simulations to better understand the effects of injection-driven turbulence level on the combustion-driven one.

POD Analysis

To see the role of cycle-resolved turbulence in cycle-to-cycle flow variations, our cycle-resolved turbulence results are compared to cycle-to-cycle flow variation results of Tanov et al. [100]. They used the phase-invariant proper orthogonal decomposition (POD) technique to investigate the cyclic-variations on in-cylinder flows of different injection strategies, based on the same PIV experimental setup and similar operating conditions as used in this study.

The POD decomposition technique provides a classification method based on an energy criterion by which the mean flow is seen as a superposition of coherent structures. From their temporal coefficients it is possible to characterize the cycle to cycle variations, in which turbulence is playing a key role. Liu et al. showed that the standard deviation of POD coefficients is representative for cycle-to-cycle flow variations [105].

Figure 7.10 shows the standard deviation of all POD coefficients as a function of CAD for SOI at -16 CAD. The POD coefficients are obtained by projecting the POD modes onto the original velocity fields. More details regarding the POD analysis and operating conditions can be found in Ref. [100].

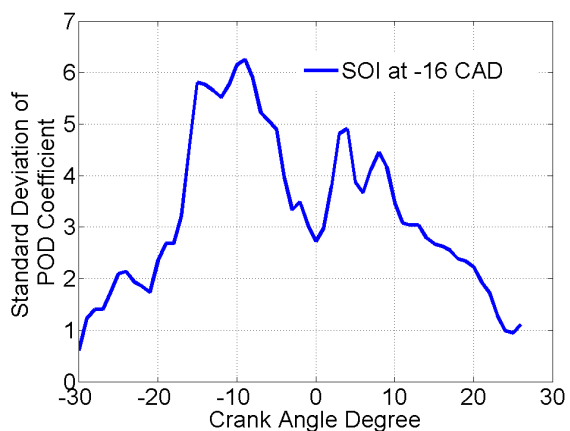


Figure 7.10: Standard deviation of POD coefficients over 44 fire cycles for SOI at -16 CAD [100]. The standard deviation of POD coefficients can be considered as an index for cycle-to-cycle flow variations [105].

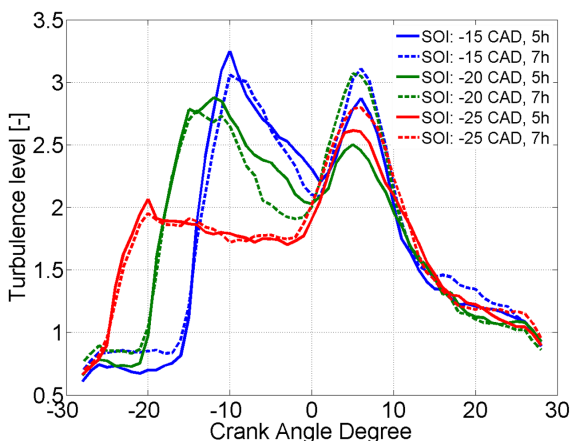
Injection-driven and combustion-driven turbulence can also be distinguished in Fig. 7.10. The temporal behavior of standard deviation of POD coefficients is similar to that of turbulence level (for example Fig. 7.7). Considering the standard deviation of POD coefficients as an index

for cycle-to-cycle flow variations [105], it can be concluded that turbulence is one of the main factors affecting the cycle-to-cycle flow variations for our PPC operating conditions.

7.4.4 Comparison of 7-hole and 5-hole injectors

The 5-hole injector has bigger orifice diameters ($159\ \mu\text{m}$) compared to the 7-hole injector ($140\ \mu\text{m}$), ensuring almost equal spray velocities but higher mass flow rate per spray for the 5-hole injector. Figure 7.11 compares the turbulence levels for these two injectors for different injection timings. During the mixing time there are only small differences between the two injectors, the 5-hole injector may cause a slightly larger increase of the turbulence, but this lies within the range of error bars (see Fig. 7.3 for the uncertainty range of turbulence level). As a conclusion, we see a similar injection-driven turbulence level per individual spray for both 5-hole and 7-hole injectors.

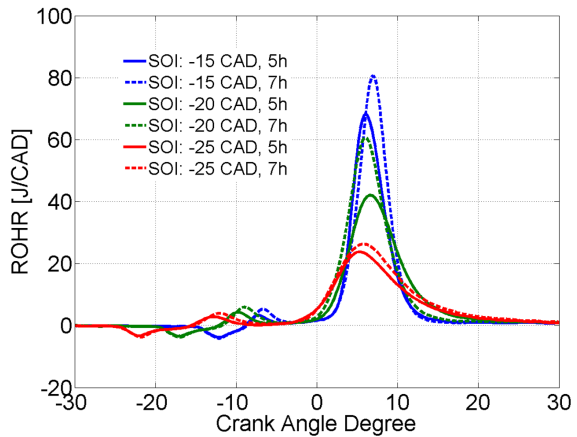
Figure 7.11: Comparison of turbulence level behaviors of 5-hole and 7-hole injectors for different injection timings. A similar injection-driven turbulence level per individual spray is seen for both 5-hole and 7-hole injectors, while the combustion-driven turbulence level for the 7-hole injector is higher than for the 5-hole injector.



Higher peak heat release rates are achieved by using the 7-hole injector, as shown in Fig. 7.12, even though the intake temperatures are a little bit lower compared to those of the 5-hole injector experiments (see Table 7.2). Hence, the heat release rate behavior has to be related to differences in homogeneity and flow characteristics. The results also show that combustion efficiency for the 7-hole injector is a little higher than for the 5-hole injector (see Table 7.2). Individual sprays of both nozzles behaving similarly, the total turbulence produced by a nozzle will scale with the number of holes. Hence, the 7-hole injector causes more turbulence and kinetic energy in the piston bowl compared to the 5-hole injector. Consequently, we can expect less stratification of both fuel and combustion for the 7-hole injector. Higher turbulence levels at SOC will result in faster combustion as discussed in the previous section. Hence, higher peak heat release rates are achieved for a 7-hole injector, with a better mixing and higher combustion efficiencies.

The maximum combustion-driven turbulence level for the 7-hole injector is noticeably higher than for the 5-hole injector. This difference cannot be explained by higher peak heat release rates since the combustion-driven turbulence level results presented in Fig. 7.6 show that the

Figure 7.12: Comparison of heat release rate of 5-hole and 7-hole injectors for different injection timings. Combustion phasing is kept constant at 7 ± 0.7 CAD ATDC by tuning the intake temperature (see Table 7.2). Higher peak heat release rates are achieved by using the 7-hole injector compared to the 5-hole injector.



maximum combustion-driven turbulence level is almost the same for different ROHR behaviors. Although not visible in our results, it is hypothesized that interactions are stronger between 7 combustion clouds (7-hole injector) compared to 5 clouds (5-hole injector), resulting in higher turbulence level, heat release rate and combustion efficiency.

7.5 Conclusions

The objective of this study was to measure cycle-resolved flow characteristics of PPC from injection to the end of combustion. High-speed PIV measurements were performed in a light-duty optical engine in a vertical planar cross-section in the piston bowl and the squish region containing the centerline of one of the sprays. The flow field, mean velocity and turbulence level for different injection timings were analyzed. Injection-driven and combustion-driven turbulence level were identified based on reactive and non-reactive conditions. Finally, flow characteristics of two different injectors with 5 and 7 holes were compared to investigate their effects on PPC.

The following is concluded based on our results:

Flow characteristics of PPC:

- During injection, the turbulence level noticeably increases by 2 to 4 times depending on the injection timing. The vortex inside the piston bowl, driven by the spray, persists during the ignition delay period.
- After the end of injection, turbulence level and mean velocity decrease, which decreases the mixing efficiency until the start of combustion.
- During combustion, mean velocity and turbulence level follow the heat release rate quite well.
- After the end of combustion, flow features are governed by the piston downward motion.

- Turbulence is one of the main factors affecting the cycle-to-cycle flow variations in PPC regime.

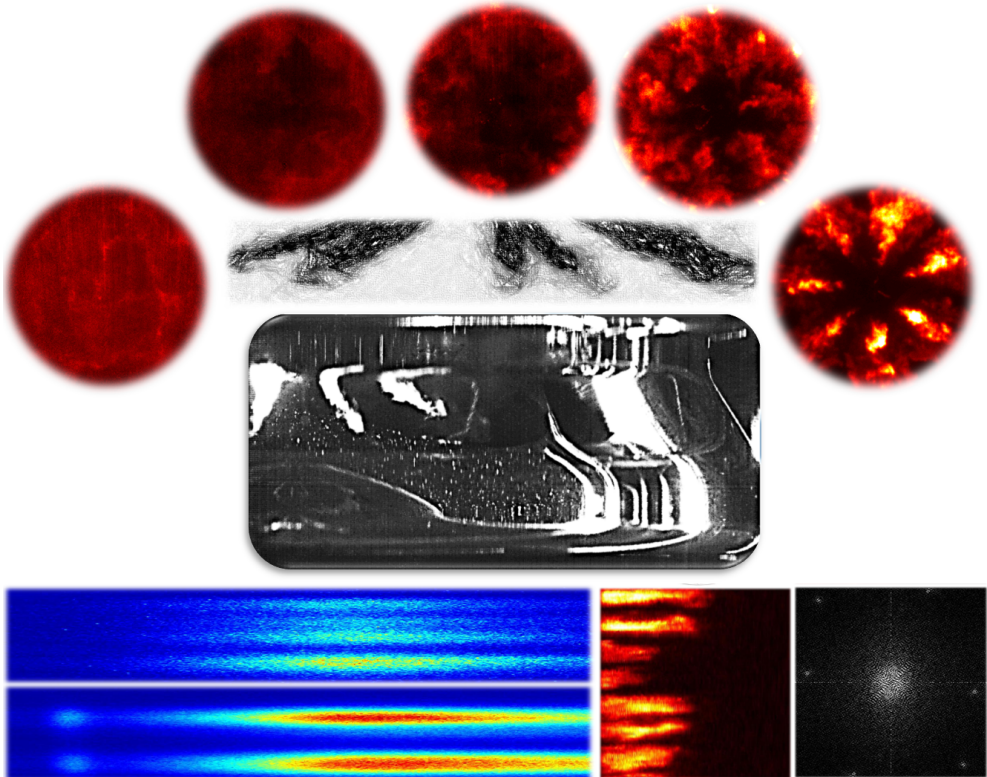
Effects of injection timing:

- Later injection (up to a certain point) causes higher mean velocity and turbulence level inside the piston bowl, and consequently higher mixing efficiency.
- Later injection causes higher injection-driven turbulence at SOC, and consequently higher peak heat release rate.
- Later injection results in less combustion-driven turbulence.

5-hole vs 7-hole injector:

- The injection-driven turbulence per individual spray is similar for both 5-hole and 7-hole injectors, indicating identical spray behavior.
- The 7-hole injector leads to higher peak heat release rates, better mixing and higher combustion efficiency compared to the 5-hole injector.
- The 7-hole injector produces higher combustion-driven turbulence than the 5-hole injector.

Conclusions and Outlook



8.1 Introduction

The main objective of this study was to optically investigate different aspects of stratification for partially premixed combustion for further understanding this combustion concept. A light-duty optical engine was used and different optical diagnostic techniques were implemented to study the combustion process. To summarize the study, three main topics, based on the research objectives, are generally discussed below. Firstly, various aspects of stratification in the PPC regime are summarized, starting from the mixing process, followed by fuel and thermal stratifications as the outcome of the mixing process, and finally the combustion process and stratification. Secondly, the proposed Fourier-based stratification index is discussed. Finally, quantification of laser and optical diagnostics is commented upon.

8.2 PPC and Stratification

Mixing

The fuel/air mixing process starts by injection, is governed by time and fluid flow characteristics, and ends by combustion. Fuel and thermal stratification at the start of combustion are the outcome of this mixing process.

Injection timing, as one of the main PPC-controlling parameters, has been investigated throughout this study in the range of -340 to -10 CAD. Shadowgraphy results showed that later injection (up to TDC) results in faster evaporation and shorter spray penetration. Both can be explained by higher in-cylinder charge temperature and pressure. PIV results showed that later injection leads to higher mean velocity and turbulence levels inside the piston bowl. Although the decay rates of mean velocity and turbulence level after the end of injection are also higher for later injections, higher turbulence levels persist up to SOC for later injections. The overall conclusion is that later injection would provide higher mixing efficiency, based on higher evaporation rate, shorter liquid penetration and higher turbulence levels. Hence, a more homogeneous mixture and combustion might be expected for later injections, if everything else particularly the ignition delay would be unchanged. This fact is illustrated by Fig. 3.15, where it can be seen that combustion stratification decreases by retarding the injection timing from -22.5 to -15 CAD, under condition of almost constant ignition delay.

However, everything else is not the same during a stroke, and notably the ignition delay seems to be a major governing parameter for the mixing process. Longer ignition delay would provide more mixing time and consequently a more homogeneous mixture at the start of combustion. Results of fuel stratification at TDC for different injection timings, presented in Fig. 6.11 based on fuel tracer LIF measurements, showed that for later injections, fuel stratification is much higher, although the mixing efficiency is higher for later injections. Hence, mixing duration (ignition delay) is the governing parameter in the mixing process, at least for the PPC operating conditions used in this study. However, for similar ignition delays, higher mixing efficiency of later injections reduces the fuel and combustion stratification.

Combustion

The outcome of the mixing process determines the subsequent combustion behavior and its stratification level.

Although it is still under debate whether a flame structure is dominant in the PPC regime or it is all volumetric auto-ignition, we saw some evidence that supports the case for a flame structure in the PPC regime. High-speed OH^* bandpass images showed a strong flame propagation structure for PPC, although it was too fast. High-speed PIV studies of reactive and non-reactive operating conditions allowed to distinguish between injection-driven and combustion-driven flow characteristics, showing that the injection-driven turbulence at the start of combustion inversely correlates with the combustion duration and the combustion-driven turbulence. In principle, volumetric auto-ignition would be independent of turbulence, while combustion speed (and consequently combustion duration) is related to the turbulence level for a flame propagation phenomenon. It is recommended for future work to use volumetric simulations to better understand the relation between injection-driven and combustion-driven turbulence, and to study flame structure in the PPC regime.

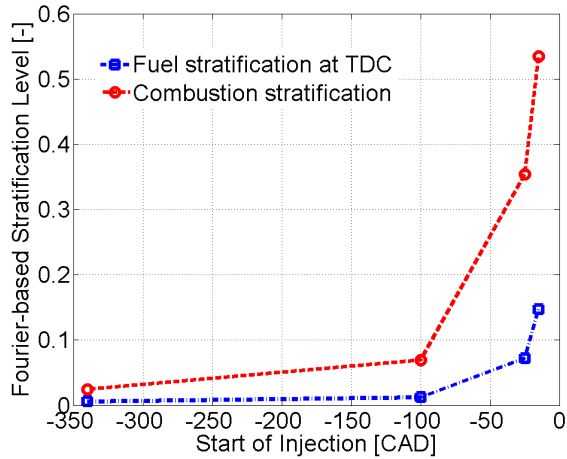
Results on fuel distribution at the start of combustion confirmed that, in the PPC regime, ignition starts in regions of high equivalence ratio, even though these have lower temperature, and then propagates toward the lower equivalence ratio regions (with higher temperatures). This relatively high gradient of equivalence ratio in the PPC regime (compared to HCCI), can be quantified as fuel stratification, and is a governing parameter to control the heat release behavior and the ignition timing of PPC. This study showed that the angular stratification plays a significant role in reducing the peak heat release rate, however, high local equivalence ratios (close to unity and higher) should be avoided, e.g. by enhancing the mixing efficiency and duration. Results of fuel stratification (chapter 6) and combustion stratification (chapter 5) are compared for the same operating conditions in Fig. 8.1. It can be seen that combustion stratification correlates with fuel stratification. To accurately assess the roles of thermal and fuel stratifications in combustion stratification, it is recommended to study the reactivity of such fuel/temperature distributions as achieved in this study.

Spectroscopy results showed that fuel stratification changes the chemistry as well. It is observed that HCCI combustion proceeds very fast; all luminosity sources observed culminate simultaneously. For PPC combustion, however, C_2^* and CH^* chemiluminescence culminate first during the combustion. Subsequently, broadband and OH^* chemiluminescence reach their peak simultaneously with the rate of heat release. Thermal radiation typically dominates during the late phase of combustion, when a second peak for C_2^* chemiluminescence is also observed.

8.3 Stratification Index

One of the main objectives of this study was to define a meaningful stratification index for PPC. In chapter 5 a stratification metric was proposed for objective quantification of combustion

Figure 8.1: Fourier-based fuel stratification level at TDC and the maximum Fourier-based combustion stratification as a function of injection timing for the operating conditions detailed in Table 5.2. There is a strong correlation between fuel stratification and combustion stratification.



stratification based on two-dimensional Fourier transforms of in-cylinder OH^* bandpass images. The same method was implemented on equivalence ratio distributions in chapter 6, to quantify fuel stratification. Results confirmed that this Fourier-based stratification index is a robust, objective and intrinsic metric to characterize different aspects of stratification in the PPC regime. The Fourier-based stratification index for fuel (or temperature) is even more robust than that for combustion stratification, since the fuel distribution can be globally characterized, based on equivalence ratio, as a meaningful parameter.

The same Fourier-based stratification analysis can be applied to temperature distributions to extract thermal stratification level. However, thermal stratification was not analyzed in this study since the temperature distribution was only estimated in chapter 6, but not measured. This is actually one of the main suggestions for future work: to study thermal stratification and to investigate its effects together with fuel stratification on combustion stratification. Two-color fuel tracer LIF is one of the laser diagnostic techniques that can be applied to simultaneously measure both fuel and temperature distributions.

Although the limited time and purpose of this study did not allow the author to go further in the application of the stratification index, this index has the potential to be used as an engineering means to optimize the mixing process, combustion efficiency and emissions, as discussed in the Introduction (chapter 1). It should be noted that the application of this index is not limited to experimental results and can be used in numerical studies as well.

8.4 Laser/Optical Diagnostics and Quantification

Quantification of the outcomes of laser and optical diagnostic techniques comprised a significant part of this study. Spray penetration as a function of injection timing and pressure was measured based on Shadowgraphy in chapter 3. The time-resolved results of the flow field, mean velocity and turbulence level were achieved based on PIV measurements (chapter 7), and fuel tracer LIF measurements were performed (chapter 6) to determine the fuel density distributions. An

analysis method was also proposed in chapter 5 to quantify combustion stratification based on OH^* bandpass images.

Although quantified measurements provide more information than qualitative measurements, it is usually needed to make some assumptions to be able to quantify the outcomes of laser and optical diagnostics. These assumptions can affect the quantified outcomes, even when the experimental errors are negligible. For instance, for quantification of fuel tracer LIF measurements in this study, the following assumptions are made:

Measurements:

- There is no shot-to-shot laser power variation.
- There is no shot-to-shot laser beam structure variation.
- Toluene evaporation and mixing characteristics are the same as for PRF70 fuel.
- The toluene fluorescence signal is not dependent on the pressure after correction for the temperature.

Temperature estimation:

- Adiabatic evaporation/mixing.
- Mass transfer is neglected, meaning that the fuel distribution is frozen from injection timing to TDC.
- No heat transfer within the field of view.

As one can imagine, these assumptions are not trivial and are definitely affecting the final results. It is possible to eliminate some of these assumptions by improving the experimental methods, for instance, by measuring the laser shot-to-shot power, a correction for the laser power can be applied. Alternatively, two-color fuel tracer LIF technique can be used instead of single-color method to measure the temperature distribution as well. Although two-color fuel tracer LIF demands its own assumptions, the outcome would be much more accurate than the temperature estimation procedure done in this study, which assumes adiabatic evaporation/mixing without heat and mass transfer.

Assumptions are also made for the PIV measurements, for instance, it is assumed that TiO_2 particles are able to perfectly follow the in-cylinder flow, or the out-of-plane velocities are not affecting the two-dimensional plane measurements.

Making such these assumptions results in a simple conclusion: there is a level of uncertainty for the obtained quantified results, although it might have been possible to improve it more and more. In this study, the focus was more on the trends and behaviors, therefore uncertainty analysis was neglected for different quantification procedures. However, some levels of uncertainty should be taken into account for all these quantified outcomes, particularly by those researchers who want to validate their numerical results with these quantified experimental data.

8.5 Conclusion

Efficiency plays a key role in future IC engines. Achieving 60% indicated efficiency for an IC engine is currently the biggest aim of many researchers in the field. On the one hand, new combustion concepts, such as PPC, have shown a potential to improve the efficiency, while maintaining low NO_x and soot emissions. On the other hand, conventional concepts have been studied and improved over a century, being the first reliable choice of manufacturers. The emerging technology of hybrid electric vehicles and upcoming limiting CO_2 emissions are providing an opportunity for the new combustion concepts to take over the role of conventional concepts. However, it can only happen if fundamental and applied investigations of the new combustion concepts, such as PPC, proceed faster, since these new combustion concepts might not have a chance to be investigated for a century.

Species Chemiluminescence

The time-resolved normalized intensity of thermal radiation and different species chemiluminescence are presented in this section for different injection timings and normalization methods. Results are based on the high-speed spectroscopy measurements and the post-processing method described in chapter 4.

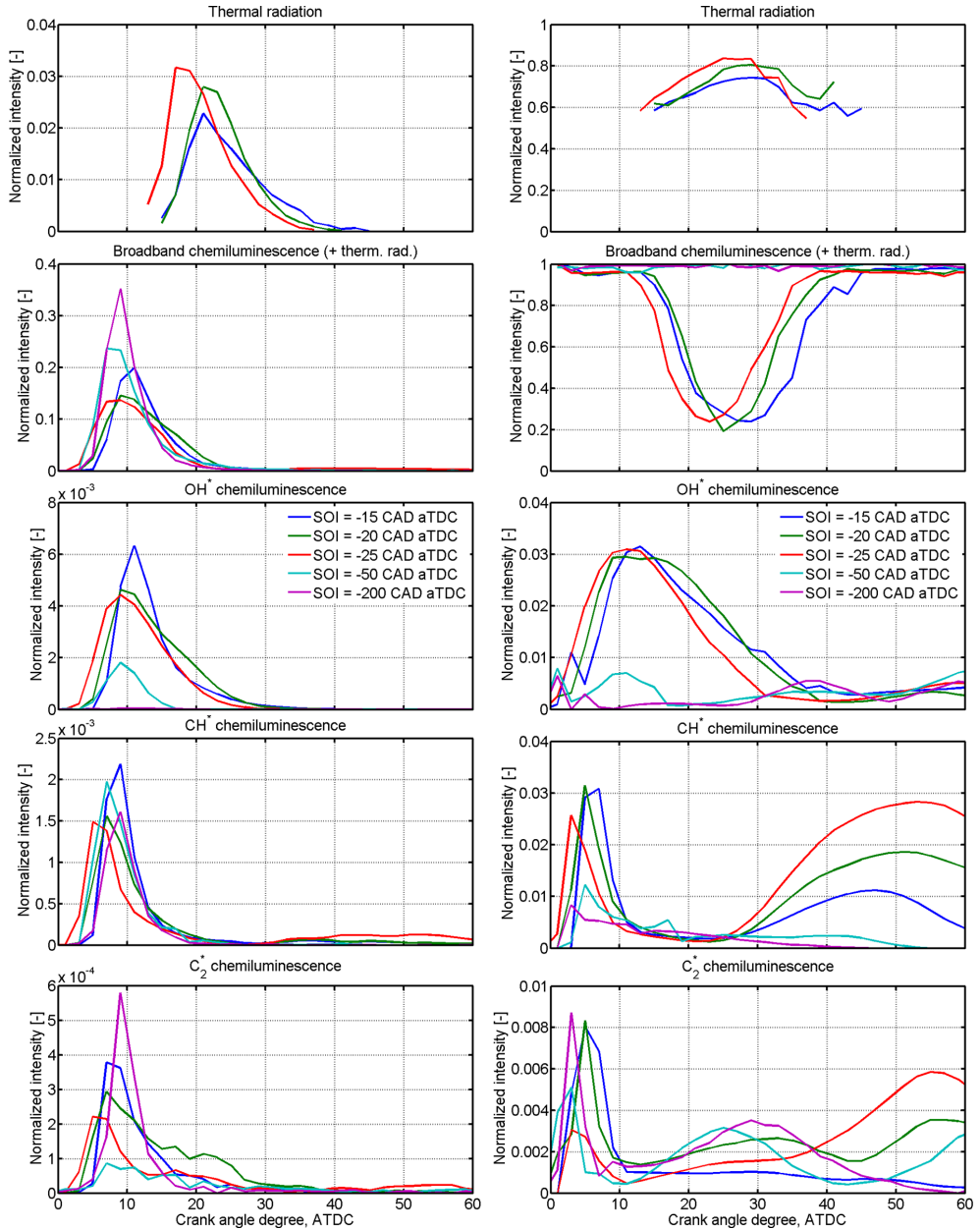


Figure A.1: Species chemiluminescence intensities for different injection timings based on two different normalization methods; Left column: Normalized by the total intensity of the combustion cycle to see the overall species behavior within a cycle. Right column: Normalized by the total intensity at a given CAD (Dynamic normalization) to see the role of each species at each CAD independently.

Abbreviations

AHRR	Apparent heat release rate
ATDC	After top dead center
BEV	Battery electric vehicle
CA50	Crank angle at 50 % burn
CA50 _{abs}	Crank angle at which 50 % of total injected fuel is burned
CAD	Crank angle degree
CCD	Charge-coupled device
CFD	Computational fluid dynamics
CH*	Electronically-excited methylidyne
CH ₂ O	Formaldehyde
CH ₂ O*	Electronically-excited formaldehyde
CI	Compression ignition
CMOS	Complementary metal–oxide semiconductor
CO	Carbon monoxide
CO ₂	Carbon dioxide
CO ₂ *	Electronically-excited carbon dioxide
C ₂ *	Electronically-excited dicarbon
DI	Direct injection
EGR	Exhaust gas recirculation
FOV	Field of view
fps	Frames per second
FWHM	Full width at half maximum
HCCI	Homogeneous charge compression ignition
HCO*	Electronically-excited formyl
HEV	Hybrid electric vehicle
IC	Internal combustion
ID	Ignition delay
IMEP	Indicated mean effective pressure
LDA	Laser doppler anemometry
LED	Light emitting diode
LIF	Laser-induced fluorescence
LTC	Low temperature combustion

Abbreviations

NO _x	Nitrogen oxides
OH*	Electronically-excited hydroxyl
POD	Proper orthogonal decomposition
PIV	Particle image velocimetry
PPC	Partially premixed combustion
ppm	Parts per million
PRFnn	Primary reference fuel, nn = the percentage of iso-octane in iso-octane/n-heptane mixture
rms	Root mean square
RANS	Reynolds averaged Navier-Stokes
ROHR	Rate of heat release
rpm	Revolutions per minute
SCCI	Stratified charge compression ignition
SI	Spark ignition
SOC	Start of combustion
SOI	Start of injection
TDC	Top dead center
TU/e	Eindhoven University of Technology

Bibliography

- [1] G. Kalghatgi and B. Johansson, "Gasoline compression ignition approach to efficient, clean and affordable future engines," *Proceedings of the Institution of Mechanical Engineers, Part D: Journal of Automobile Engineering*, pp. 1–21, 2017.
- [2] International Energy Agency, "Global EV outlook 2017: Two million and counting."
- [3] R. Agarwal, "Review of technologies for sustainable ground transportation," *SAE Technical Paper*, 2013-01-1039, 2013.
- [4] "ExxonMobil outlook for energy: Journey to 2040, <http://corporate.exxonmobil.com/en/energy/energy-outlook>."
- [5] C. Noehre, M. Andersson, B. Johansson, and A. Hultqvist, "Characterization of partially premixed combustion," *SAE Technical Paper*, 2006-01-3412, 2006.
- [6] M. Lewander, *Characterization and Control of Multi-Cylinder Partially Premixed Combustion*. Lund University, PhD dissertation, 2011.
- [7] F. Zhao, T. N. Asmus, D. N. Assanis, J. E. Dec, J. A. Eng, and P. M. Najt, *Homogeneous charge compression ignition (HCCI) engines : key research and development issues*. Warrendale, PA: Society of Automotive Engineers, 2003.
- [8] J. Warnatz, U. Maas, and R. Dibble, *Combustion: Physical and Chemical Fundamentals, Modeling and Simulation, Experiments, Pollutant Formation*. Berlin, Germany: Springer, 2006.
- [9] S. M. Aceves, D. L. Flowers, F. Espinosa-Loza, J. Martinez-Frias, J. E. Dec, M. Sjöberg, R. W. Dibble, and R. P. Hessel, "Spatial analysis of emissions sources for HCCI combustion at low loads using a multi-zone model," *SAE Technical Paper*, 2004-01-1910, 2004.
- [10] A. B. Dempsey, S. J. Curran, and R. M. Wagner, "A perspective on the range of gasoline compression ignition combustion strategies for high engine efficiency and low NO_x and soot emissions: Effects of in-cylinder fuel stratification," *International Journal of Engine Research*, vol. 17, no. 8, pp. 897–917, 2016.

- [11] F. Bowditch, "A new tool for combustion research a quartz piston engine," *SAE Technical Paper*, 610002, 1961.
- [12] K. Mollenhauer and H. Tschöke, *Handbook of diesel engines*. Berlin/Heidelberg: Springer-Verlag, 2010.
- [13] I. Truedsson, *Measuring and Describing Auto-Ignition for HCCI Combustion Engines*. Lund University, Doctoral dissertation, 2014.
- [14] P. Bakker, J. D. A. Goes, L. Somers, and B. Johansson, "Characterization of low load PPC operation using RON70 fuels," *SAE Technical Paper*, 2014-01-1304, 2014.
- [15] L. Egelmeers, *Chemiluminescence and Spectroscopy Study of Partially Premixed Combustion in a Light-Duty Optical Engine*. Eindhoven University of Technology, Master dissertation, 2016.
- [16] J. Desantes, J. López, S. Molina, and D. López-Pintor, "Design of synthetic EGR and simulation study of the effect of simplified formulations on the ignition delay of isoctane and n-heptane," *Energy Conversion and Management*, vol. 96, pp. 521–531, 2015.
- [17] G. Woschni and J. Fieger, "Determination of local heat transfer coefficients at the piston of a high speed diesel engine by evaluation of measured temperature distribution," *SAE Technical Paper*, 790834, 1979.
- [18] J. Gatowski, E. Balles, K. Chun, F. Nelson, J. Ekchian, and J. Heywood, "Heat release analysis of engine pressure data," *SAE Technical Paper*, 841359, 1984.
- [19] L. Hildingsson, G. Kalghatgi, N. Tait, B. Johansson, and A. Harrison, "Fuel octane effects in the partially premixed combustion regime in compression ignition engines," *SAE Technical Paper*, 2009-01-2648, 2009.
- [20] M. Lewander, K. Ekholm, B. Johansson, P. Tunestål, N. Milovanovic, N. Keeler, T. Harcombe, and P. Bergstrand, "Investigation of the combustion characteristics with focus on partially premixed combustion in a heavy duty engine," *SAE International Journal of Fuels and Lubricants*, vol. 1, no. 1, pp. 1063–1074, 2009.
- [21] L. Yin, G. Ingesson, S. Shamun, P. Tunestål, R. Johansson, and B. Johansson, "Sensitivity analysis of partially premixed combustion (PPC) for control purposes," *SAE Technical Paper*, 2015-01-0884, 2015.
- [22] K. Kunkulagunta, "Video imaging and analysis of common rail sprays in an optical engine using shadowgraphy technique," *SAE Technical Paper*, 2000-01-1255, 2000.
- [23] J. Pastor, J. García, J. Pastor, and L. Zapata, "Evaporating diesel spray visualization using a double-pass shadowgraphy/schlieren imaging," *SAE Technical Paper*, 2007-24-0026, 2007.
- [24] S. Kaiser, V. Salazar, and A. Hoops, "Schlieren measurements in the round cylinder of an optically accessible internal combustion engine," *Applied Optics*, vol. 52, no. 14, pp. 3433–3443, 2013.

- [25] M. Weinrotter, E. Wintner, K. Iskra, T. Neger, J. Olofsson, H. Seyfried, M. Aldén, M. Lackner, F. Winter, A. Vressner, A. Hultqvist, and B. Johansson, "Optical diagnostics of laser-induced and spark plug-assisted HCCI combustion," *SAE Technical Paper*, 2005-01-0129, 2005.
- [26] T. Fujikawa, T. Ozasa, and K. Kozuka, "Development of transparent cylinder engines for schlieren observation," *SAE Technical Paper*, 881632, 1988.
- [27] T. Ozasa, K. Kozuka, and T. Fujikawa, "Schlieren observations of in-cylinder phenomena concerning a direct-injection gasoline engine," *SAE Technical Paper*, 982696, 1998.
- [28] K. Kozuka, T. Ozasa, T. Fujikawa, and A. Saito, "Schlieren observation of spark-ignited premixed charge combustion phenomena using a transparent collimating cylinder engine," *Journal of Engineering for Gas Turbines and Power*, vol. 125, pp. 336–343, 2003.
- [29] M. Founti, Y. Hardalupas, C. Hong, C. Keramiotis, K. Ramaswamy, N. Soulopoulos, A. Taylor, D. Touloupis, and G. Vourliotakis, "An experimental investigation on the effect of diluent addition on flame characteristics in a single cylinder optical diesel engine," *SAE Technical Paper*, 2015-24-2438, 2015.
- [30] S. Tanov, R. Collin, B. Johansson, and M. Tuner, "Combustion stratification with partially premixed combustion, PPC, using NVO and split injection in a LD - diesel engine," *SAE International Journal of Engines*, vol. 7, no. 4, pp. 1911–1919, 2014.
- [31] R. Zegers, J. Aussems, B. Somers, N. Dam, C. Luijten, and L. de Goey, "Correlating flame location and ignition delay in partially premixed combustion," *SAE Technical Paper*, 2012-01-1579, 2012.
- [32] Z. Li, X. Yu, G. Lequien, T. Lind, M. Jansons, O. Andersson, and M. Richter, "Comparison of the lift-off lengths obtained by simultaneous OH-LIF and OH* chemiluminescence imaging in an optical heavy-duty diesel engine," *SAE Technical Paper*, 2015-24-2418, 2015.
- [33] A. Maghbouli, T. Lucchini, G. D'Errico, M. I. Najafabadi, and B. Somers, "Numerical investigation of PPCI combustion at low and high charge stratification levels," *SAE Technical Paper*, 2017-01-0739, 2017.
- [34] J. Heywood, *Internal Combustion Engine Fundamentals*. McGraw-Hill, 1988.
- [35] K. Myong, M. Arai, H. Suzuki, J. Senda, and H. Fujimoto, "Vaporization characteristics and liquid-phase penetration for multi-component fuels," *SAE Technical Paper*, 2004-01-0529, 2004.
- [36] K. Kim, C. Bae, and B. Johansson, "Spray and combustion visualization of gasoline and diesel under different ambient conditions in a constant volume chamber," *SAE Technical Paper*, 2013-01-2547, 2013.
- [37] R. Vallinayagam, S. Vedharaj, Y. An, A. A. Dawood, M. I. Najafabadi, B. Somers, and B. Johansson, "Combustion stratification for naphtha from CI combustion to PPC," *SAE Technical Paper*, 2017-01-0745, 2017.

- [38] S. Vedharaj, R. Vallinayagam, Y. An, A. Dawood, M. I. Najafabadi, B. Somers, J. Chang, and B. Johansson, "Fuel effect on combustion stratification in partially premixed combustion," *SAE Technical Paper*, 2017-24-0089, 2017.
- [39] Y. An, S. Vedharaj, R. Vallinayagam, A. Dawood, J.-B. Masurier, M. I. Najafabadi, B. Somers, J. Chang, and B. Johansson, "Effect of aromatics on combustion stratification and particulate emissions from low octane gasoline fuels in PPC and HCCI mode," *SAE Technical Paper*, 2017-24-0086, 2017.
- [40] R. Vallinayagam, S. Vedharaj, Y. An, A. Dawood, M. I. Najafabadi, B. Somers, J. Chang, M. Sarathy, and B. Johansson, "Compression ignition of light naphtha and its multicomponent surrogate under partially premixed conditions," *SAE Technical Paper*, 2017-24-0078, 2017.
- [41] T. Lucchini, A. D. Torre, G. D'Errico, and G. Montenegro, "Automatic mesh generation for CFD simulations of direct-injection engines automatic mesh generation for CFD simulations of direct-injection engines," *SAE Technical Paper*, 2015-01-0376, 2015.
- [42] H. Weller, G. Tabor, H. Jasak, and C. Fureby, "A tensorial approach to CFD using object orientated techniques," *Computers in Physics*, vol. 12, no. 6, pp. 620–631, 1998.
- [43] T. Lucchini, G. D'Errico, F. Brusiani, and G. B. ., "A finite-element based mesh motion technique for internal combustion engine simulations," *COMODIA 2008*, MS2-3, 2008.
- [44] Y.-D. Liu, M. Jia, M.-Z. Xie, and B. Pang, "Enhancement on a skeletal kinetic model for primary reference fuel oxidation by using a semidecoupling methodology," *Energy and Fuels*, vol. 26, no. 12, pp. 7069–7083, 2012.
- [45] Y. Pei, E. R. Hawkes, M. Bolla, S. Kook, G. M. Goldin, Y. Yang, S. B. Pope, and S. Som, "An analysis of the structure of an n-dodecane spray flame using tpdf modelling," *Combustion and Flame*, vol. 168, pp. 420–435, 2016.
- [46] M. Musculus, P. Miles, and L. Pickett, "Conceptual models for partially premixed low-temperature diesel combustion," *Progress in Energy and Combustion Science*, vol. 39, no. 2-3, pp. 246–283, 2013.
- [47] J. Dec, "Advanced compression-ignition engines - understanding the in-cylinder processes," *Proceedings of the Combustion Institute*, vol. 32, no. 2, pp. 2727–2742, 2009.
- [48] R. Reitz, "Directions in internal combustion engine research," *Combustion and Flame*, vol. 160, no. 1, pp. 1–8, 2013.
- [49] M. Jakob, T. Hülser, A. Janssen, P. Adomeit, S. Pischinger, and G. Grünefeld, "Simultaneous high-speed visualization of soot luminosity and OH* chemiluminescence of alternative-fuel combustion in a HSDI diesel engine under realistic operating conditions," *Combustion and Flame*, vol. 159, no. 7, pp. 2516–2529, 2012.
- [50] J. Dec and C. Espey, "Ignition and early soot formation in a DI diesel engine using multiple 2-D imaging diagnostics," *SAE Technical Paper*, 950456, 1995.

- [51] A. Hultqvist, M. Christensen, B. Johansson, A. Franke, M. Richter, and M. Aldén, "A study of the homogeneous charge compression ignition combustion process by chemiluminescence imaging," *SAE Technical Paper*, 1999-01-3680, 1999.
- [52] A. Gaydon, *The Spectroscopy of Flames*. London: Chapman and Hall, 1974.
- [53] J. Zhang, W. Jing, and T. Fang, "High speed imaging of OH* chemiluminescence and natural luminosity of low temperature diesel spray combustion," *Fuel*, vol. 99, pp. 226–234, 2012.
- [54] T. Kathrotia, U. Riedel, A. Seipel, K. Moshhammer, and A. Brockhinke, "Experimental and numerical study of chemiluminescent species in low-pressure flames," *Applied Physics B*, vol. 107, no. 3, pp. 571–584, 2012.
- [55] J. Dec and C. Espey, "Chemiluminescence imaging of autoignition in a di diesel engine," *SAE Technical Paper*, 982685, 1998.
- [56] B. Kim, M. Kaneko, Y. Ikeda, and T. Nakajima, "Detailed spectral analysis of the process of HCCI combustion," *Proceedings of the Combustion Institute*, vol. 29, no. 1, pp. 671–677, 2002.
- [57] R. Augusta, D. Foster, J. Ghandhi, J. Eng, and P. Najt, "Chemiluminescence measurements of homogeneous charge compression ignition (HCCI) combustion," *SAE Technical Paper*, 2006-01-1520, 2006.
- [58] M. I. Najafabadi, N. Dam, B. Somers, and B. Johansson, "Ignition sensitivity study of partially premixed combustion by using shadowgraphy and OH* chemiluminescence methods," *SAE Technical Paper*, 2016-01-0761, 2016.
- [59] J. Kojima and Y. I. abd Tsuyoshi Nakajima, "Spatially resolved measurement of OH*, CH*, and C₂* chemiluminescence in the reaction zone of laminar methane/air premixed flames," *Proceedings of the Combustion Institute*, vol. 28, no. 2, pp. 1757–1764, 2000.
- [60] Y. Hardalupas and M. Orain, "Local measurements of the time-dependent heat release rate and equivalence ratio using chemiluminescent emission from a flame," *Combustion and Flame*, vol. 139, no. 3, pp. 188–207, 2004.
- [61] M. Kopp, O. Mathieu, and E. Petersen, "Rate determination of the CO₂* chemiluminescence reaction $\text{CO} + \text{O} + \text{M} \rightleftharpoons \text{CO}_2^* + \text{M}$," *International Journal of Chemical Kinetics*, vol. 47, no. 1, pp. 50–72, 2014.
- [62] V. Nori and J. Seitzman, "CH* chemiluminescence modeling for combustion diagnostics," *Proceedings of the Combustion Institute*, vol. 32, no. 1, pp. 895–903, 2009.
- [63] A. Yoshida, M. Narisawa, and H. Tsuji, "Structure of highly turbulent premixed flames," *Symposium (International) on Combustion*, vol. 24, no. 1, pp. 519–525, 1992.
- [64] S. Merola, B. Vaglieco, F. Corcione, and E. Mancaruso, "In-cylinder combustion analysis by flame emission spectroscopy of transparent CR diesel engine," *SAE Technical Paper*, 2003-01-1112, 2003.

- [65] V. Nori and J. Seitzman, "Evaluation of chemiluminescence as a combustion diagnostic under varying operating conditions," *46th AIAA Aerospace Sciences Meeting and Exhibit*, no. AIAA 2008-953, 2008.
- [66] H. Solaka, U. Aronsson, M. Tuner, and B. Johansson, "Investigation of partially premixed combustion characteristics in low load range with regards to fuel octane number in a light-duty diesel engine," *SAE Technical Paper*, 2012-01-0684, 2012.
- [67] J. Krasselt, D. Foster, J. Ghandhi, R. Herold, D. Reuss, and P. Najt, "Investigations into the effects of thermal and compositional stratification on HCCI combustion - part I: Metal engine results," *SAE Technical Paper*, 2009-01-1105, 2009.
- [68] A. Berntsson and I. Denbratt, "HCCI combustion using charge stratification for combustion control," *SAE Technical Paper*, 2007-01-0210, 2007.
- [69] M. I. Najafabadi, L. Egelmeers, B. Somers, N. Deen, B. Johansson, and N. Dam, "The influence of charge stratification on the spectral signature of partially premixed combustion in a light-duty optical engine," *Applied Physics B*, vol. 123, no. 108, pp. 1–13, 2017.
- [70] M. Seul, L. O’Gorman, and M. Sammon, *Practical algorithms for image analysis*. New York: Cambridge University Press, 2000.
- [71] C. Schulz and V. Sick, "Tracer-LIF diagnostics: quantitative measurement of fuel concentration, temperature and fuel/air ratio in practical combustion systems," *Progress in Energy and Combustion Science*, vol. 31, no. 1, pp. 75–121, 2005.
- [72] M. P. Musculus, "Multiple simultaneous optical diagnostic imaging of early-injection low-temperature combustion in a heavy-duty diesel engine," *SAE Technical Paper*, 2006-01-0079, 2006.
- [73] D. Sahoo, B. Petersen, and P. Miles, "Measurement of equivalence ratio in a light-duty low temperature combustion diesel engine by planar laser induced fluorescence of a fuel tracer," *SAE International Journal of Engines*, vol. 4, no. 2, pp. 2312–2325, 2011.
- [74] B. Petersen, P. Miles, and D. Sahoo, "Equivalence ratio distributions in a light-duty diesel engine operating under partially premixed conditions," *SAE International Journal of Engines*, vol. 5, no. 2, pp. 526–537, 2012.
- [75] B. Petersen, I. Ekoto, and P. Miles, "Effect of fuel properties on UHC and CO emissions from partially premixed combustion," *Proceedings of the 10th International Congress of Engine Combustion Processes*, 2011.
- [76] W. Colban, I. Ekoto, D. Kim, and P. C. Miles, "In-cylinder PIV measurements in an optical light-duty diesel at LTC conditions," *THIESEL 2008 Conference on Thermo- and Fluid Dynamic Processes in Diesel Engines*, 2008.
- [77] S. Kokjohn, R. Reitz, D. Splitter, and M. Musculus, "Investigation of fuel reactivity stratification for controlling PCI heat-release rates using high-speed chemiluminescence imaging and fuel tracer fluorescence," *SAE International Journal of Engines*, vol. 5, no. 2, pp. 248–269, 2012.

- [78] Q. Tang, H. Liu, M. Li, and M. Yao, "Study on the double injection strategy of gasoline partially premixed combustion under a light-duty optical engine," *SAE International Journal of Engines*, vol. 9, no. 4, pp. 2185–2193, 2016.
- [79] M. P. Musculus, T. Lachaux, L. M. Pickett, and C. A. Idicheria, "End-of-injection over-mixing and unburned hydrocarbon emissions in low-temperature-combustion diesel engines," *SAE Technical Paper*, 2007-01-0907, 2007.
- [80] Z. Wang, S. Lonn, A. Matamis, O. Andersson, M. Tuner, M. Alden, and M. Richter, "Transition from HCCI to PPC: Investigation of fuel distribution by planar laser induced fluorescence (PLIF)," *SAE International Journal of Engines*, vol. 10, no. 4, 2017.
- [81] R. Zegers, M. Yu, C. Bekdemir, N. Dam, C. Luijten, and L. de Goey, "Temperature measurements of the gas-phase during surrogate diesel injection using two-color toluene LIF," *Applied Physics B*, vol. 112, no. 1, pp. 7–23, 2013.
- [82] M. I. Najafabadi, N. Dam, B. Somers, and B. Johansson, "Fuel and combustion stratification study of partially premixed combustion," *ECCO-MATE Conference I: Combustion Processes in Marine and Automotive Engines*, 2016.
- [83] R. Klein-Douwel, P. Frijters, X. Seykens, L. Somers, and R. Baert, "Gas density and rail pressure effects on diesel spray growth from a heavy-duty common rail injector," *Energy and Fuels*, vol. 23, no. 4, pp. 1832–1842, 2009.
- [84] M. I. Najafabadi, S. Tanov, H. Wang, B. Somers, B. Johansson, and N. Dam, "Effects of injection timing on fluid flow characteristics of partially premixed combustion based on high-speed particle image velocimetry," *SAE International Journal of Engines*, vol. 10, no. 4, 2017.
- [85] N. Ashgriz, *Handbook of Atomization and Sprays, Theory and Applications*. Springer, 2011.
- [86] V. Manente, B. Johansson, and W. Cannella, "Gasoline partially premixed combustion, the future of internal combustion engines?," *International Journal of Engine Research*, vol. 12, no. 3, 2011.
- [87] W. Hardy and R. Reitz, "An experimental investigation of partially premixed combustion strategies using multiple injections in a heavy-duty diesel engine," *SAE Technical Paper*, 2006-01-0917, 2006.
- [88] M. I. Najafabadi, B. Somers, and A. Nuraini, "Validation of a reduced chemical mechanism coupled to CFD model in a 2-stroke HCCI engine," *SAE Technical Paper*, 2015-01-0392, 2015.
- [89] G. Neely, S. Sasaki, and J. Leet, "Experimental investigation of PCCI-DI combustion on emissions in a light-duty diesel engine," *SAE Technical Paper*, 2004-01-0121, 2004.
- [90] G. Kalghatgi, P. Risberg, and H. Angstrom, "Advantages of fuels with high resistance to auto-ignition in late-injection, low-temperature, compression ignition combustion," *SAE Technical Paper*, 2006-01-3385, 2006.

- [91] R. Hanson, D. Splitter, and R. Reitz, "Operating a heavy-duty direct-injection compression-ignition engine with gasoline for low emissions," *SAE Technical Paper*, 2009-01-1442, 2009.
- [92] Z. Wang, S. Tanov, H. Wang, M. Richter, B. Johansson, and M. Alden, "High-speed particle image velocimetry measurement of partially premixed combustion (PPC) in a light duty engine for different injection strategies," *SAE Technical Paper*, 2015-24-2454, 2015.
- [93] B. Johansson, "Influence of the velocity near the spark plug on early flame development," *SAE Technical Paper*, 930481, 1993.
- [94] P. Miles, M. Megerle, V. Sick, K. Richards, Z. Nagel, and R. Reitz, "The evolution of flow structures and turbulence in a fired HSDI diesel engine," *SAE Technical Paper*, 2001-01-3501, 2001.
- [95] P. Miles, M. Megerle, J. Hammer, Z. Nagel, R. Reitz, and V. Sick, "Late-cycle turbulence generation in swirl-supported, direct-injection diesel engines," *SAE Technical Paper*, 2002-01-0891, 2002.
- [96] P. Miles, R. Collin, L. Hildingsson, A. Hultqvist, and O. Andersson, "Combined measurements of flow structure, partially oxidized fuel, and soot in a high-speed, direct-injection diesel engine," *Proceedings of the Combustion Institute*, vol. 31, no. 2, pp. 2963–2970, 2007.
- [97] P. Miles, L. Hildingsson, and A. Hultqvist, "The influence of fuel injection and heat release on bulk flow structures in a direct-injection, swirl-supported diesel engine," *Experiments in Fluids*, vol. 43, no. 2-3, pp. 273–283, 2007.
- [98] R. Zegers, C. Luijten, N. Dam, and L. de Goey, "Pre- and post-injection flow characterization in a heavy-duty diesel engine using high-speed PIV," *Experiments in Fluids*, vol. 53, no. 3, pp. 731–746, 2012.
- [99] "Particle image velocimetry (PIV), <http://www.dantecdynamics.com/particle-image-velocimetry>."
- [100] S. Tanov, Z. Wang, H. Wang, M. Richter, and B. Johansson, "Effects of injection strategies on fluid flow and turbulence in partially premixed combustion (PPC) in a light duty engine," *SAE Technical Paper*, 2015-24-2455, 2015.
- [101] H. Wang, S. Tanov, M. I. Najafabadi, Z. Wang, and B. Johansson, "Time-resolved in-cylinder PIV measurement in a light duty optical engine under PPC conditions," *Lisbon 2016 International Symposium on the Application of Laser and Imaging Techniques to Fluid Mechanics*, 2016.
- [102] S. Tanov, B. Johansson, M. I. Najafabadi, and H. Wang, "Analyzing of in-cylinder flow structures and cyclic variations of partially premix combustion in a light duty engine," *FISITA 2016 World Automotive Congress*, no. F2016-ESYF-005, 2016.

- [103] P. Miles, *Turbulent Flow Structure in Direct-Injection, Swirl-Supported Diesel Engines*. Heidelberg Germany: Springer Berlin, 2009.
- [104] R. J. Tabaczynski, "Turbulence and turbulent combustion in spark-ignition engines," *Progress in Energy and Combustion Science*, vol. 2, no. 3, pp. 143–165, 1976.
- [105] K. Liu and D. C. Haworth, "Development and assessment of pod for analysis of turbulent flow in piston engines," *SAE Technical Paper*, 2011-01-0830, 2011.

Acknowledgements

I would like to express my sincere gratitude to the people who contributed to this work.

Nico, only few people in my life have had a long-term effect on me and on the way I see people and the world. You are definitely one of them. I cannot forget the first day I came to your office, introduced myself and asked you a question about my experiments. You immediately walked with me to the lab and helped me for hours. I learned a lot from you and I do appreciate all the time you spent on details of my research, on reading and modifying every word of my manuscripts and hours of discussion on different aspects of my research. You are a real scientist and an amazing supervisor.

Bart, I met you first during a Skype interview when I was in Kuala Lumpur, and I was really amazed by your nice attitude. I highly acknowledge that you gave me this opportunity to work with you as one of your *guys* and I greatly appreciate your knowledge and understanding of combustion and IC engines. We also traveled lots together, from Greece to US, and that was always exciting for me to go through a conversation with you; it could be even at your “castle” in Chania after a long walk. Thank you so much for all your support.

Bengt, I have been always proud to have you as my first promoter. You are a genius who needs only a glance at a graph of any engine related experiments to fully understand it, and even find what has been done in a wrong way, and what should be done for the next step. We experienced a unique way of working together, usually thousands of kilometers away from each other. Our monthly Skype meetings were always fruitful for me. I visited you for a few months, when you were in Lund, and it was a nice experience to work with you in close distance as well.

I would also like to extend my gratitude to Philip and Niels. Philip, during the first two years of my PhD, our regular meetings were always motivating me; thank you so much for all your advises. Niels, your willingness to be a part of my committee is appreciated, thank you.

Visiting two other institutions, Lund University and ETH Zurich, and working with the nice people there was a priceless experience for me.

I would like to express my gratitude to the team at the division of combustion engines at Lund University, where I spent a nice summer in 2015. Slavey, you were a great host and friend. We spent most of the summer together in the lab; a cage in the basement where fingers could be easily burned by hot optical pistons!

Acknowledgements

My special thanks to the people at LAV laboratory at ETH Zurich, particularly Panos, Maria, Christophe, Yuri, Walter and Ruta. I experienced a nice working structure and a great summer in Zurich together with you. I learned a lot at your group, and I greatly appreciate all your supports.

A significant amount of results presented in this work is based on the efforts of students who worked with me during their graduation project. I would like to particularly thank Luc, Linda and John. It was nice to work with all of you.

I wish to thank my colleagues/friends who made my daily working hours full of joy and excitement: PC, Aromal, Robin, Denis, Jos, Shuli, Noud, Amin, Robbert, Bersan, Nard, Yigit, Marjan, Camila, Suleyman, Zhen, Theo, Hans, Bart, Martin, and others. I have enjoyed very much having coffee, lunch, BBQ, sport and trips with you. I wish you all the best. PC and Aromal, we were sitting one meter away from each other for 3 years. PC, we had many challenging conversations and made very nice and unforgettable memories. You are definitely a nice friend and were a super-helpful colleague. Not only did you spend a year on preparation of the experimental setup I used, but you were also continuously supporting me to plan my experiments. Aromal, I was always enjoying our long conversations about different aspects of life. You know a lot, even about me!

I would like to express my sincerely gratitude and special thanks to my father and mother. I cannot imagine having better parents than you. You have helped me to realize my own potential and have cared a lot about my education from the first days of primary school, and have encouraged and supported me up until now. Words cannot describe how thankful I am. My lovely sisters: Shirin, Leila and Maedeh, I learned a lot from you, from our childhood until now, specially from you, Maedeh. I highly appreciate all your love and supports.

Fahimeh, there is no doubt that I could not finish this work without your efforts, patience, encouragement and love. We have experienced different aspects of life together, happiness and sadness, hope and disappointment, clarity and confusion, and many more things to come. However, you have always been lightening up the life for me and helping me to find my own way. Thanks for every moment of your life being with me. Our beautiful daughter, Rosa, will be proud of having such an amazing mom. I love you both.

PhD Publications

Peer-reviewed Journal and Technical Papers

1. Izadi Najafabadi, M., Somers, B., Johansson, B., Dam, N., (2017) "Fuel Stratification Study of Partially Premixed Combustion Using Fuel-Tracer LIF," *Applied Physics B: Lasers & Optics*, under review.
2. Izadi Najafabadi, M., Somers, B., Johansson, B., Dam, N., (2017) "Combustion Stratification Study of Partially Premixed Combustion by Using Fourier Transform Analysis of OH* Chemiluminescence Images," *International Journal of Engine Research*, in Press, doi:10.1177/1468087417740270".
3. Izadi Najafabadi, M., Egelmeers, L., Somers, B., Deen, N., Johansson B., Dam, N., (2017) "The influence of charge stratification on the spectral signature of partially premixed combustion in a light-duty optical engine," *Applied Physics B: Lasers & Optics* 123:108, doi:10.1007/s00340-017-6688-9.
4. Izadi Najafabadi, M., Tanov, S., Wang, H., Somers, B., Johansson, B., Dam, N., (2017) "Effects of Injection Timing on Fluid Flow Characteristics of Partially Premixed Combustion Based on High-Speed Particle Image Velocimetry," *SAE International Journal of Engines* 10(4), doi:10.4271/2017-01-0744.
5. Vedharaj, S., Vallinayagam, R., An, Y., Izadi Najafabadi, M., Somers, B., Chang, J., Johansson, B., (2017) "Combustion Homogeneity and Emission Analysis during the Transition from CI to HCCI for FACE I Gasoline," *SAE Technical Paper* 2017-01-2263, doi:10.4271/2017-01-2263.
6. An, Y., Vallinayagam, R., Vedharaj, S., Masurier, J.B., Dawood, A., Izadi Najafabadi, M., Somers, B., Johansson, B., (2017) "Analysis of Transition from HCCI to CI via PPC with Low Octane Gasoline Fuels using Optical Diagnostics and Soot Particle Analysis," *SAE Technical Paper* 2017-01-2403, doi:10.4271/2017-01-2403.
7. An, Y., Vedharaj, S., Vallinayagam, R., Dawood, A., Masurier, J.B., Izadi Najafabadi, M., Somers, B., Chang, J., Johansson, B., (2017) "Effect of Aromatics on Combustion Stratification and Particulate Emissions from surrogate of Naphtha fuels in PPC and HCCI mode," *SAE Technical Paper* 2017-24-0086, doi:10.4271/2017-24-0086.

8. Vallinayagam, R., Vedharaj, S., An, Y., Dawood, A., Izadi Najafabadi, M., Somers, B., Chang, J., Sarathy, M., Johansson, B., (2017) "Compression Ignition of Light Naphtha and its Multi-component Surrogate under Various Mixing Conditions," *SAE Technical Paper 2017-24-0078*, doi:10.4271/2017-24-0078.
9. Vedharaj, S., Vallinayagam, R., An, Y., Dawood, A., Izadi Najafabadi, M., Somers, B., Chang, J., Johansson, B., (2017) "Fuel Effects on Combustion Stratification in Partially Premixed Combustion," *SAE Technical Paper 2017-24-0089*, doi:10.4271/2017-24-0089.
10. Vallinayagam, R., Vedharaj, S., An, Y., Dawood, A., Izadi Najafabadi, M., Somers, B., Johansson, B., (2017) "Combustion Stratification for Naphtha from CI Combustion to PPC," *SAE Technical Paper 2017-01-0745*, doi:10.4271/2017-01-0745.
11. Maghbouli, A., Lucchini, T., D'Errico, G., Izadi Najafabadi, M., Somers, B., (2017) "Numerical Investigation of PPCI Combustion at Low and High Charge Stratification Levels," *SAE Technical Paper 2017-01-0739*, doi:10.4271/2017-01-0739.
12. Izadi Najafabadi, M., Dam, N., Somers, B., Johansson, B., (2016) "Ignition Sensitivity Study of Partially Premixed Combustion by Using Shadowgraphy and OH* Chemiluminescence methods," *SAE Technical Paper 2016-01-0761*, doi:10.4271/2016-01-0761.
13. Izadi Najafabadi, M., Somers, B., and Nuraini, A., (2015) "Validation of a Reduced Chemical Mechanism Coupled to CFD Model in a 2-Stroke HCCI Engine," *SAE Technical Paper 2015-01-0392*, doi:10.4271/2015-01-0392.

Conference Papers

1. An, Y., Vallinayagam, R., Vedharaj, S., Masurier, J.B., Dawood, A., Izadi Najafabadi, M., Somers, B., Johansson, B., (2017) "Combustion stratification and emissions under PPC mode in an optical engine at various EGR ratios," *9th International Conference On Modeling And Diagnostics For Advanced Engine Systems (COMODIA 2017)*, Okayama, July 2017.
2. Tanov, S., Johansson, B., Izadi Najafabadi, M., Wang, H., (2016) "Analyzing of In-Cylinder Flow Structures and Cyclic Variations of Partially Premixed Combustion in a Light Duty Engine," *FISITA 2016 World Automotive Congress*, F2016-ESYF-005, Busan, September 2016.
3. Wang, H., Tanov, S., Izadi Najafabadi, M., Wang, Z., Johansson, B., (2016) "Time-resolved in-cylinder PIV measurement in a light duty optical engine under PPC conditions," *Lisbon 2016 International Symposium on the Application of Laser and Imaging Techniques to Fluid Mechanics*, Lisbon, July 2016.
4. Izadi Najafabadi, M., Dam, N., Somers, B., Johansson, B., (2016) "Fuel and combustion stratification study of partially premixed combustion," *ECCO-MATE Conference I: Combustion Processes in Marine and Automotive Engines*, Lund, June 2016.

Curriculum vitae

Mohammad Izadi Najafabadi was born on February 22nd, 1987 in Najafabad, Iran. He is a researcher with background and interest in Internal Combustion Engines, Optical/Laser Diagnostics, Fluid Mechanics, CFD and Thermal Engineering.

Work Experience

- **Eindhoven University of Technology** 05-2014 / Present
PhD Researcher (the work presented in this thesis)
- **ETH Zurich** 05-2017 / 08-2017
Visiting Researcher on optical data processing.
- **Lund University** 05-2015 / 07-2015
Visiting Researcher on high-speed PIV measurements
- **University Putra Malaysia** 09-2011 / 02-2014
Research & Teaching Assistant
- **Irankhodro Powertrain Company** 09-2009 / 09-2011
R&D Engineer on piston thermal management.

Education

- **MSc in Mechanical Engineering** 09-2011 / 02-2014
University Putra Malaysia, Kuala Lumpur, Malaysia
Thesis: Numerical and Experimental Studies of Homogeneous Charge Compression Ignition Engine Performance.
- **BSc in Mechanical Engineering** 09-2005 / 09-2010
Amirkabir University of Technology (Tehran Polytechnic), Tehran, Iran
Thesis: Computational and Experimental Analysis of Piston Cooling Jet.

